Biphotons for Nonlinear Imaging

Ivi Afxenti

Submitted in fulfilment of the requirements for the
Degree of Doctor of Philosophy

James Watt School of Engineering
College of Science and Engineering
University of Glasgow

Abstract

The harnessing of the nonclassical properties in photon pairs generated by the process of Spontaneous Parametric Down Conversion (SPDC) to enhance two-photon interactions has long intrigued researchers. Their use in light-matter interactions has been proven to improve efficiency either by increasing the rate of generation or by suppressing noise. Namely, the processes of Entangled Sum Frequency Generation (eSFG) and Entangled Two Photon Absorption (eTPA) have been shown to produce more photons when stimulated with entangled photons than the classical versions of the effects. This has only been effective so far at very low intensities, which, alongside the inability to reproduce previous experimental results, has caused debates about the usefulness of the effect. In the presented work, I aim to shed light on the topic by employing a carefully crafted source of entangled photon pairs to improve two-photon effects. I attempt to demonstrate, through a series of experiments, that the quantum enhancement can be observed at an order of magnitude higher than previously thought possible. To solidify the results, a direct comparison of the quantum effect was conducted by investigating the performance of the phenomenon when it is stimulated by classical radiation from a laser. Our results confirm a quantum improvement in a regime previously considered impossible, and they enabled us to examine the ramifications of the effect on imaging. By doing so, we consider real-life microscopy applications, and therefore, we can set limits to the effect.

Contents

List of Tables

List of Figures

List of Acronyms

Author Contributions

1. Thomas Dickinson, Ivi Afxenti, Giedre Astrauskaite, Lennart Hirsch, Samuel Nerenberg, Ottavia Jedrkiewicz, Daniele Faccio, Caroline Müllenbroich, Alessandra Gatti, Matteo Clerici, Lucia Caspani,"Quantum-enhanced second harmonic generation beyond the photon pairs regime", Science Advances, eadw4820 (2025)

2. Ivi Afxenti, Lijun Yu, Taylor Shields, Daniele Faccio, Thomas Bradley, Lucia Caspani, Matteo Clerici, and Adetunmise C. Dada, "Polarization purity and dispersion characteristics of nested antiresonant nodeless hollow-core optical fiber at near- and short-wave-IR wavelengths for quantum communications," Optics Express 32, 34471-34481 (2024)

3. Tie-Jun Wang, Mehdi H. Ebrahim, Ivi Afxenti, Dionysis Adamou, Adetunmise C. Dada, Ruxin Li, Yuxin Leng, Jean-Claude Diels, Daniele Faccio, Arnaud Couairon, Carles Milián, Matteo Clerici, "Cumulative Effects in 100 kHz Repetition-Rate Laser-Induced Plasma Filaments in Air", Advanced Photonics Research, 4: 2200338, (2023)

Acknowledgements

I would like to express my sincere gratitude to my supervisor, Matteo Clerici, from whom I learned so much. His infectious enthusiasm in the lab consistently motivated me to put forth my best effort. Special thanks to my first/second supervisor Daniele Faccio, for allowing me to join his group and for his invaluable support and constructive input on the project.

My sincere thanks also go to Lucia Caspani, the lead investigator of this study. Her input and guidance were instrumental in bringing this project to completion, providing thoughtful feedback throughout the process. Acknowledgements are due to Thomas Dickinson for his valuable contributions to this work, whose input played a role in the development of this project

Finally, I want to express my gratitude to my family and friends, who supported me by providing me with space to share both my excitement and frustration during this PhD.

Declaration

I declare that, unless otherwise stated, all the work presented in this thesis is mine.

CHAPTER 1

Introduction

The ability to control light has enabled us to visually represent a wide range of biological structures, from the microscopic, such as single cells, to the very large, such as entire living organisms. This hasn't only helped us gain insight into their mechanisms and aid in fighting diseases, but has also enabled control over their genetic engineering. Two-photon interactions underpin some of these imaging technologies, such as nonlinear imaging, spectroscopy and two-photon optogenetics [1–3]. Those techniques enable the imaging of in-vivo pathophysiology, but they come with limitations. More specifically, nonlinear microscopy requires high photon fluxes to achieve photon coincidence and hence simultaneous interaction at the sample, which can damage the sample. Moreover, compared to one-photon absorption, multiphoton cross-sections, which measure the sample's ability to absorb photons, are very small. This leads to weaker signals, requiring high-sensitivity detectors and long acquisition times.

To overcome these difficulties, a new approach of using two-beam optical microscopy with nonclassical light sources was proposed in 1990 [4]. Specifically, Javanainen and Gould suggested that using entangled photons, exhibiting high correlations, can alleviate the disadvantages mentioned above. Since then, numerous studies have been produced on the matter, with the earliest ones confirming the duo's theory [5]. Using photon pairs generated by spontaneous parametric down conversion (SPDC), the probability of absorption increases, thereby increasing the efficiency of two-photon processes, such as entangled two-photon absorption (eTPA) and entangled sum-frequency generation (eSFG). However, more recent work done in this field has been met with doubt [6–8]. In this thesis, we aim to tailor the spatiotemporal correlations in SPDC to shed new light on entangled two-photon interactions by focusing on eSFG.

1.1 Thesis Overview

My goal for this thesis is to state our contribution to the topic of entangled two-photon interactions. I begin by introducing the theoretical background and, after explaining the main concepts, provide a summary of the research conducted to date on the subject.

The third Chapter summarises the work done during the first two years of my PhD, with the main focus on investigating SPDC to enhance the nonlinear Sum-Frequency Generation (SFG) process. In this Chapter, the main findings on the process efficiency are summarised. Then, the results from comparing the effect with the generation of the sum-frequency signal from a lossy state are discussed. These results provide insight into how the careful exploitation of the energy-time and space-momentum entanglement in the biphoton state can enhance the efficiency of two-photon effects in a power regime previously considered impossible. The results are validated by performing a direct comparison of the quantum effect with its classical counterpart, in which the generated eSFG is measured against the SFG produced by a classical source.

These results allowed us to explore further applications for the quantum effect. We utilise the biphoton field to image the excitation signal produced by the entangled photons, aiming to establish this as a technique with potential for real imaging applications. The imaging scheme and the main results are provided in Chapter 4 of this thesis. More specifically, the implications of the nature of the entangled light on the resolution of the imaging system were investigated, and our main findings are discussed.

Apart from the work I've done on entangled two-photon processes, I also led a project with great potential for quantum communication schemes. More specifically, photon pairs were generated at 2 µm spectral range and propagated through a nested anti-resonant hollow-core fibre. By studying the polarisation extinction ratio and effects of dispersion, we investigated whether the hollow-core fiber is a potential platform for performing quantum communications. This work is presented in Chapter 5.

Finally, the last Chapter provides a summary of the main insights from this research and suggestions for future work.

CHAPTER 2

Theoretical background and literature review

2.1 Introduction

SPDC lies at the intersection of quantum mechanics and nonlinear optics, serving as a bridge between these two fields, and even giving birth to a new topic in photonics, namely quantum nonlinear optics. It has enabled the generation of individual photons, paving the way for an immeasurable number of quantum applications by making interactions possible at the level of individual quanta. After its initial observation in 1967 [9, 10] and the experimental verification of its quantum nature [11], SPDC is now one of the most widely used processes to generate entangled photon pairs. At its core, SPDC is a second-order nonlinear optical phenomenon in which a pump photon splits into two new photons with half the energy of the mother photon. The process doesn't require an input signal; the vacuum field serves as a seed. While this means the process can be quite inefficient, it corroborates the effect's inherent quantum nature. The new photon pair exhibits strong quantum correlations, making it impossible to describe both photon fields independently; therefore, the produced pair is an entangled state of light. Both features of correlations and entanglement are leveraged to enhance sensing, computing, and communications [12–14].

When pumped with a high-intensity beam, the SPDC process transitions from the spontaneous to the stimulated regime, thereby increasing its efficiency. The radiation is sometimes referred to as bright Squeezed Vacuum (SV), and at this regime, previously generated photons can stimulate the production of new ones. As a result, the process's efficiency scales exponentially, characterised by a high parametric gain, leading to the generation of more photon pairs. While photon correlations and entanglement remain, the state is now mixed because higher-order generated photon pairs can interact with one another. More specifically, for SV, the correlation widths between time and frequency and between space and momentum broaden [15, 16], and therefore the degree to which two

conjugate variables are linked decreases. Another essential feature of photons produced by SPDC is squeezing, typically described in terms of the electromagnetic field quadratures. For example, in a system where precise phase measurements are essential, the phase uncertainty can be reduced below the quantum limit, but at the cost of increasing the uncertainty in its conjugate observable, i.e., the amplitude [16]. The nature of squeezed states has enabled precise measurements even below the shot noise of photodetectors, overcoming the fundamental classical limit [17–19].

In this research, both the spontaneous and stimulated regimes of Parametric Down Conversion (PDC) were explored and their features exploited to enhance two-photon processes. In the remainder of this chapter, the theoretical framework of second-order nonlinear effects is presented, with a focus on PDC and its nonclassical features. I then give a theoretical description of the SFG process, which is the reverse of PDC. Lastly, a review of relevant prior work on two-photon processes is presented.

2.2 Theoretical framework

2.2.1 Parametric Down Conversion

Unlike linear optics, in nonlinear phenomena, the interaction between a laser and a medium is strong enough to displace electrons in the material. More specifically, each atom in the material will develop an oscillating dipole moment that radiates at a frequency different from that of the initial laser source. This is unlike linear interactions, where the dipole re-radiates at the same frequency as the excitation field. Here, instead, it will lead to a polarisation that depends nonlinearly on the electric field:

$$\boldsymbol{P} = \epsilon_o(\chi^{(1)}\boldsymbol{E} + \chi^{(2)}\boldsymbol{E}\boldsymbol{E} + ..) \tag{2.1}$$

with ϵ_o the permittivity of free space, and $\chi^{(1)}$ and $\chi^{(2)}$, the linear and nonlinear susceptibilities of the medium, respectively. We restrict our study to include only the effects produced by the second-order nonlinear susceptibility and examine the evolution of these effects in the time domain. For these nonlinear phenomena to occur, the medium must lack centrosymmetry, as centrosymmetric materials are characterised by inversion symmetry, which causes a vanishing second-order susceptibility coefficient [20]. In the presence of a strong oscillating electric field, materials that lack centrosymmetry will have their electrons' average position displaced, and the resulting dipole moments created will radiate, as explained above. By considering such a material, which is also isotropic and dispersionless, nonlinear differential equations that describe the propagation of light inside the

nonlinear medium can be derived by substituting Eq.1 into Maxwell's equations:

$$\nabla^2 \tilde{E} - \frac{1}{c^2}\frac{\partial^2 \tilde{E}}{\partial t^2} = -\mu_o \frac{\partial^2 \tilde{P}}{\partial t^2} \tag{2.2}$$

where $\tilde{E}$ represents the complex field amplitude, the term on the RHS is the source term and μ_o is the magnetic permeability. Two different approximations can be used to solve the above: the Born Approximation and the coupled-wave theory approximation [21]. The first one treats the problem as a scattering problem, while the latter considers the electric field as the sum of the present waves from the nonlinear interaction. This is the approximation considered here. In the case of three-wave mixing, two fields interact to generate a third field with frequency ω_3:

$$\omega_3 = \omega_1 + \omega_2 \tag{2.3}$$

and the non-linear source term and the applied fields are then written as:

$$\tilde{P} = P_3 e^{(-i\omega_3 t)} + c.c. \quad where \quad P_3 = 4\epsilon_0 d_{eff} E_1 E_2 \tag{2.4}$$

$$\tilde{E_i} = E_i e^{(-i\omega_i t)} + c.c \quad where \quad E_i = A_i e^{ik_i z} \quad and \quad i = 1, 2 \tag{2.5}$$

By substituting Eq.2.4 and Eq.2.5 into Maxwell's equation Eq.2.2, three coupled-wave equations can be derived:

$$\frac{dA_1}{dz} = \frac{2id_{eff}\omega_1^2}{k_1 c^2} A_3 A_2^* e^{-i\Delta k z} \tag{2.6}$$

$$\frac{dA_2}{dz} = \frac{2id_{eff}\omega_2^2}{k_2 c^2} A_3 A_1^* e^{-i\Delta k z} \tag{2.7}$$

$$\frac{dA_3}{dz} = \frac{2id_{eff}\omega_3^2}{k_3 c^2} A_2 A_1 e^{i\Delta k z} \tag{2.8}$$

where it is assumed that the three waves propagate in the z-direction and that the pump field amplitude is constant along the interaction length [22]. The parameter d_{eff} is called the effective nonlinear coefficient and is related to the material's nonlinear susceptibility by $d_{eff} = \chi^{(2)}/2$. The parameter Δk was also introduced, which is referred to as the momentum mismatch and in ideal scenarios Δk=0 and is generally defined as:

$$\Delta k = k_3 - k_2 - k_1 \tag{2.9}$$

The above expression, alongside Eq.2.3, are referred to as phase-matching equations and represent energy and momentum conservation laws. For the nonlinear process to be efficient, the mismatch in the interaction should be minimised by achieving the condition

known as "perfect phase-matching". This occurs when the radiation of each dipole in the material constructively interferes to form a well-defined beam of frequency ω_3, which propagates in the forward direction. The coupled differential equations for the generated frequency ω_3 can be solved by integrating over the crystal length, from 0 to l_c. Therefore, the intensity of the generated beam is equal to:

$$I_3 = \frac{8d_{eff}^2\omega_3^2 I_1 I_2}{n_1 n_2 n_3 \epsilon_0 c^3} l_c^2 \mathrm{sinc}^2\left(\frac{\Delta k l_c}{2}\right) \tag{2.10}$$

where $I_j = 2n_j\epsilon_0 c|A_j|^2$. When $\omega_1 \neq \omega_2$, the solution above describes the phenomenon of SFG and it is evident that when perfect phase-matching is achieved, for $\Delta k = 0$, the sinc function becomes equal to 1, and the intensity of the generated field will grow quadratically in terms of the length of the medium, under the undeleted pump approximation [23]. The above equation also shows how the intensity of the generated field depends on the second-order susceptibility of the material, with higher nonlinear susceptibilities resulting in a brighter generated field. However, the choice of a nonlinear material is far from trivial since different applications require tailoring different crystal parameters to achieve the desired application objective. For example, depending on the selected crystal, the produced fields can have orthogonal polarisation to the incident pump field, or they can be orthogonally polarised to each other, with the two interactions referred to as Type-I and Type-II, respectively [24]. To accommodate these different demands, many nonlinear materials are typically grown into crystals of varying sizes, with frequently used materials including Lithium Niobate (LN), Beta Barium Borate (BBO), and Lithium Triborate (LBO). The development of new nonlinear materials and their nonlinear susceptibilities is being rigorously studied to characterise their nonlinear response and to advance photoelectric technologies [25–27]. In general, the nonlinear susceptibility $\chi^{(n)}$ of the material is a tensor of rank $n+1$, but, as we will see in the following sections, only susceptibilities of specific materials can have their tensorial elements nonvanishing and can therefore induce a nonlinear response.

Now, let's consider the case of a perfectly phase-matched interaction between a pump field and a nonlinear medium, in which two new fields, the signal and idler, are created. The evolution of these two fields can be described by the Manley-Rowe solutions:

$$\mathrm{A_s(z)} = \mathrm{A_s(0)cosh(\gamma z)} \tag{2.11}$$

$$\mathrm{A_i(z)} = \mathrm{i\zeta}\frac{\mathrm{A_p}}{|\mathrm{A_p}|}\mathrm{A_s(0)sinh(\gamma z)} \tag{2.12}$$

where $\zeta = \sqrt{(\mathrm{n_s\omega_i/n_i\omega_s})}$ and $\gamma = \frac{\chi^{(2)}_{\mathrm{eff}}|\mathrm{A_p}|}{\mathrm{c}}\sqrt{\omega_\mathrm{i}\omega_\mathrm{p}/\mathrm{n_i n_p}}$. Interestingly, from the solutions above, it is evident that if $\mathrm{A_s(0)} = 0$, then the generation of signal and idler fields is

impossible; hence, no SPDC can be produced [28]. Hence, we conclude that this model is not suitable for describing the process and turn our attention to a quantum description of the interaction [24].

2.2.2 Quantum description

The SPDC process is typically considered to be the amplification of vacuum fluctuations, and, as we've seen so far, a classical formulation of the one provided above is not adequate to describe the parametric process. To fully explain the effect, a quantum model is formulated by first quantising the electromagnetic field, which results in it behaving like a harmonic oscillator with discrete modes. The quantisation of the electromagnetic field won't be included in this thesis, but a complete derivation can be found in [29, 30]. The obtained expression can be substituted back into the Hamiltonian describing the SPDC process:

$$\hat{\mathrm{H}}_{\mathrm{PDC}} = i\hbar\kappa\left(a_s^\dagger a_i^\dagger a_p + a_s a_i a_p^\dagger\right) \tag{2.13}$$

where κ is a coupling constant dependent on the crystal properties. The resulting equation also comprises the annihilation and creation operators, $\hat{a}_{i,s,p}$ and $\hat{a}^\dagger_{i,s,p}$, for the idler, signal and pump photons, respectively. These terms describe the pump photon annihilating into two new photons in optical modes, each with half the energy of the first. By considering the Schrödinger picture, the generated state can be described by using a time-ordered perturbation series:

$$\begin{aligned}|\Psi\rangle_{\mathrm{PDC}} = |0> &+ \frac{i}{\hbar}\int_{\mathrm{t_0}}^{\mathrm{t}} \mathrm{dt}'\hat{\mathrm{H}}_{\mathrm{PDC}}(\mathrm{t}')|0> \\ &+ \left(\frac{i}{\hbar}\right)^2 \int_{\mathrm{t_0}}^{\mathrm{t}} \mathrm{dt}'\hat{\mathrm{H}}_{\mathrm{PDC}}(\mathrm{t}') \int_{\mathrm{t_0}}^{\mathrm{t}'} \mathrm{dt}''\hat{\mathrm{H}}_{\mathrm{PDC}}|0> + ..\end{aligned} \tag{2.14}$$

In the above expression, we first have the vacuum emission term, and the first- and second-order terms that follow correspond to the creation of one-photon and two-photon pairs, respectively [31]. The vacuum emission term indicates that there is a nonzero probability that no photon pairs will be generated, demonstrating that SPDC is a weak nonlinear interaction, with typically only 10^{-5} to 10^{-12} pump photons being converted into signal and idler photons. When the second and higher-order terms are also present, the state is often called a SV [32], with multiple photon pairs occupying the optical modes. The process then becomes more efficient, characterised by a higher parametric gain, and the interaction strength grows exponentially with the pump amplitude. In contrast, when only the vacuum state and first-order terms are present, the growth of the generated fields to the pump is linear. The parametric gain of the process often distinguishes these

two regimes of PDC, which in this thesis and in some of the literature are referred to as high-gain and low-gain, respectively [33, 34]. More specifically, we will refer to operating in the low-gain regime of PDC when fewer than one photon per mode is present. Of course, this refers to the far field of the radiation, since in the PDC's birth zone, photons are generated in pairs. Once we increase the interaction gain, allowing more photons to occupy each mode, we refer to it as being in the high-gain regime. In this thesis, mode is defined as the coherence volume where photon pairs can be found, and pairs generated by PDC can exist in a large number of position and momentum modes. This means that high-dimensionality of information can be mapped to the state [35]. To determine the number of photons produced at the output of the crystal, one could resort to the Heisenberg picture, where the state is considered static, with the operators being evolved. The Bogoliubov–Valatin transformations are used, and the expression:

$$N_s = \langle 0 | \, V^2 a_i^\dagger a_i \, | 0 \rangle = \frac{P_p \kappa^2}{\Gamma^2} \sinh^2(\Gamma l_c) \tag{2.15}$$

is obtained, where $\mathrm{V} = \sinh(\Gamma \mathrm{l_c})$ and the plane-wave pump approximation was assumed to hold [36]. The parameter $\Gamma = \sqrt{2\pi P_p \kappa - (\Delta k(\omega)/2)^2}$ is the parametric gain of the process, and Λ is related to the crystal properties, as mentioned earlier. If we assume that the interaction is adequately phase-matched, then $2\pi \mathrm{P_p}\kappa >> (\Delta \mathrm{k}(\omega)/2)^2$ and therefore the parametric gain can be simplified to $\Gamma = \sqrt{2\pi \mathrm{P_p}\kappa}$. Following the theoretical work presented in [37–39], and redefining parameter κ the above Eq.2.15 can be rewritten as:

$$\mathrm{N_s} = \mathrm{K_m}\left(\Lambda\sqrt{\mathrm{N_p}}\right)\sinh^2\left(\Lambda\sqrt{\mathrm{N_p}}\right) \tag{2.16}$$

where it was assumed that the number of pump photons $\mathrm{N_p}$ is proportional to the pump power $\mathrm{P_p}$. In general, the parametric gain is proportional to the crystal length, its nonlinear characteristics, and the peak photon flux density of the pump. Therefore parametric gain was substituted by $\Lambda\sqrt{\mathrm{N_s}}$ where Λ is now related to the crystal parameters:

$$\Lambda = 2 l_c d_{eff} \sqrt{\frac{\hbar \omega_p \omega_{SV}^2}{2\epsilon_0 n_p n_{SV}^2 c^2 V_p}} \tag{2.17}$$

where l_c the crystal length, d_{eff} the effective nonlinear coefficient of the crystal and V_p the spatiotemporal volume of the pump with units $\mathrm{m^2 s}$. For Eq.2.16, a quasi-stationary approximation was made, where both the pump and SV have large cross-sections and temporal durations, much larger than the entanglement area and time of the generated SV, parameters which will be introduced in the next section.

As mentioned previously, for sufficiently high parametric gain, SPDC ceases to be a spontaneous process and enters the stimulated regime, where photons created at the start

of the nonlinear crystal seed the generation of new pairs. As we will see in the upcoming chapters of this thesis, apart from the change in the number of photons generated, other characteristics of the PDC transform as well for different interaction gains. Therefore, Eq. 2.16 was used at various points throughout this research to characterise the PDC source as a function of the process's gain.

Most quantum imaging applications [40–42] rely on the nonclassical features of PDC, such as squeezing or entanglement. At the very low gain of PDC, only one or fewer photons start to occupy each mode. PDC is usually utilised in this regime to avoid the arrival of "accidentals" in coincidence experiments [43] or to reduce the noise in sub-shot noise imaging experiments [44], even though the quantum correlations of different degrees of freedom survive in the high-gain regime. Since PDC is governed by the phase-matching conditions, as described by Eq.2.3 and 2.9, photon pairs generated by the process exhibit strong spatial (position-momentum) and temporal (time-frequency) correlations. These, alongside entanglement, are described in the next sections.

2.2.3 Quantum correlations and entanglement

States of light generated by SPDC are used to showcase the Einstein–Podolsky–Rosen (EPR) paradox, and therefore validate the quantum nature of the produced light [45]. Famously, a thought experiment designed to disprove quantum mechanics and its core tenets, the EPR paradox highlighted that superposition and entanglement entail violations of locality and the uncertainty principle. Today, resolving the EPR paradox through a Bell inequality test confirms the validity of quantum mechanics and the existence of high correlations between observables [46]. Biphotons generated by SPDC exhibit correlations in their position and momentum, and therefore, the state of the system cannot be expressed as the product of the separable states that encompass it:

$$|\Psi\rangle_{AB} \neq |\psi\rangle_A |\psi\rangle_B \tag{2.18}$$

Hence, it is impossible to define the state or its density operator for individual parts of it, i.e, A or B. If we now consider the phase matching Eq.2.9, when signal and idler photons are emitted around the pump beam, they shall do so by conserving the transverse momentum $\mathbf{q}$ of the system so that $\mathbf{q_p} = \mathbf{q_s} + \mathbf{q_i} = 0$. However, in reality, a pump with a finite size along the transverse direction has an uncertainty in its transverse momentum $\Delta\mathbf{q_p}$. Hence, the transverse momentum conservation stipulation becomes $|\mathbf{q_s} + \mathbf{q_i}| \leq \Delta\mathbf{q_p}$, which means that the pump restricts the sum of transverse momenta of the signal and idler. A similar condition holds if we consider the energy-conservation phase-matching

Eq.2.3. The biphoton energies won't sum up to a constant, but instead, there will be some uncertainty stemming from the pump's own uncertainty in energy, represented as $|\omega_i + \omega_s| \leq \Delta\omega_p$. This is shown graphically in Figure 2.1. In Figure 2.1 B, the range of all the possible frequencies that the signal and idler photon can sum up to is $\Delta\omega_p$, while the possible range of frequencies that the individual photons can have to satisfy energy conservation is given by $\Delta\omega_{s+i}$. The same restrictions apply for momentum as shown in Figure 2.1 A. A longer crystal restricts the angular spectrum of the photon pair, while a shorter crystal results in a broader one [47]. This is due to the restrictions a longer crystal imposes on the phase-matching bandwidth, as it becomes increasingly challenging to achieve perfect phase-matching due to the accumulated phase mismatch throughout its length [21].

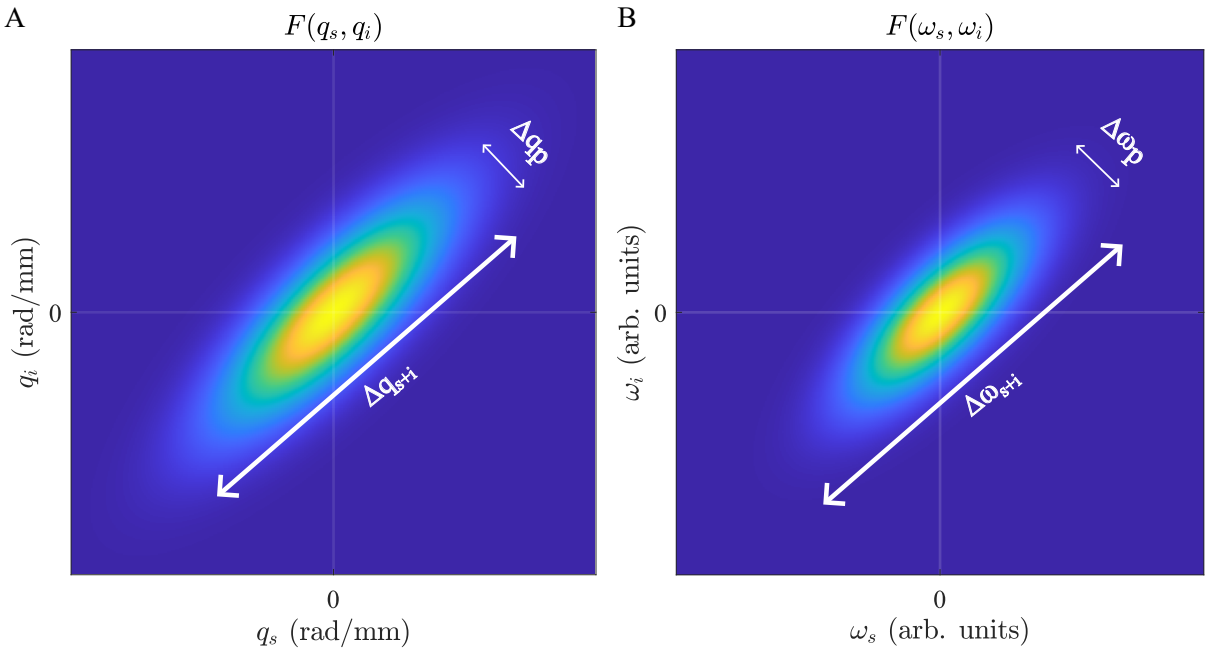

Figure 2.1: **Joint frequency and momentum distributions of the biphoton state.** Crystal phase-matching properties and pump bandwidth are the main factors for the frequency and momentum distributions, shown in **A** and **B**, respectively.

Of course, both frequency ω and momentum $\mathbf{q}$ have their conjugate variables, time t and position x, respectively. Both of these are the Fourier transform of the aforementioned frequency and momentum, and from these, the entanglement time T_e and area A_e can be found. These define the time and area in which the photon pairs are entangled. A broader spectrum of frequencies $\Delta\omega_{s+i}$ means a smaller time window in which the entangled photons can be found together, and similarly, the larger the spread in transverse momentum, the smaller the area where the pairs can be found. This can be visualised if we consider a similar representation as the ones provided for frequency and momentum in Figure 2.1, but this time, their conjugate variable will spread along the anti-diagonal with Δq_p being the Fourier transform of Δx and $\Delta\omega_p$ the Fourier transform of the Δt. Therefore, a small

uncertainty in Δq_p and $\Delta\omega_p$ will result in a large uncertainty of Δx and Δt, respectively. The width of the two anti-diagonals will be the entanglement area A_e and time T_e, and the fact that they are not the Fourier conjugates of Δq_p and $\Delta\omega_p$ offers the opportunity to circumvent limitations that are present in classical optics. For example, a simultaneous measurement can be made with high temporal resolution and short frequency uncertainty. This is how entangled photons can circumvent the limitations present in classical measurements. Entanglement time T_e and area A_e set the temporal and spatial resolution in two-photon processes, with the ability to shape temporal correlations so that short entanglement times in the scale of a few femtoseconds can be achieved [48]. This enables the possibility of exciting states with minimal energy-level differences [49].

As with any other nonlinear process, the phase-matching equations govern PDC, and the correlations discussed above directly stem from the nature of phase matching in PDC. Next, we consider phase-matching in a birefringent crystal to investigate how it affects the geometry of the generated field.

2.2.4 Phase-matching

Generally, phase-matching conditions are hard to meet in common media since they can't fulfil the condition $n_i(\omega_i) = n_s(\omega_s)$ ($< n_p(\omega_p)$ in typical cases). For this reason, birefringent materials are typically employed, in which the directionality and polarisation of light, relative to the crystal's axes, affect the index of refraction that the incoming ray will experience. This is evident in anisotropic materials, where the field oscillating along different directions within the crystal experiences different values of refractive index. Crystals like this are either uniaxial or biaxial, having two or three refractive indices, respectively [50]. Here, we consider the geometry of uniaxial crystals, e.g., BBO, with the electric field displacement $\mathbf{D}$ being a sum of the three components of the electric field E and the electric permittivity, ϵ_{ij}, where $i, j = 1, 2, 3$:

$$\mathbf{D_i} = \sum_{\mathrm{j}} \epsilon_{\mathrm{ij}} \mathrm{E_j} \tag{2.19}$$

due to the fact that $\mathbf{D}$ and E are no longer parallel. The electric permittivity is a second-rank tensor. A convenient choice of coordinate system can result in vanishing off-diagonal elements of the permittivity ϵ_{ij}. In the remaining directions, the electric field and the electric displacement are parallel, which defines the crystal's principal axis [51]. Hence, the principal refractive indices are related to the permittivity by:

$$n_i = \sqrt{\frac{\epsilon_i}{\epsilon_0}} \quad \text{with } i\text{=1,2,3} \tag{2.20}$$

and waves travelling along the principal axes with polarisation at some angle to the axes, will have polarisation components experiencing different phase velocities. Therefore, it is common to use an index ellipsoid to depict this, with the geometry of a negative uniaxial crystal is shown in Fig.2.2. The ellipsoid is described by:

$$\frac{x_1^2}{n_1^2} + \frac{x_2^2}{n_2^2} + \frac{x_3^2}{n_3^2} = 1 \tag{2.21}$$

with $x_{1,2,3}$ being the principal axes. In the case of uniaxial crystals, two of the refractive indices are the same $n_1 = n_2 = n_o$ and are called ordinary, while the third is called extraordinary $n_3 = n_e$. For the rest of the section, equations will be introduced using the n_o and n_e notation.

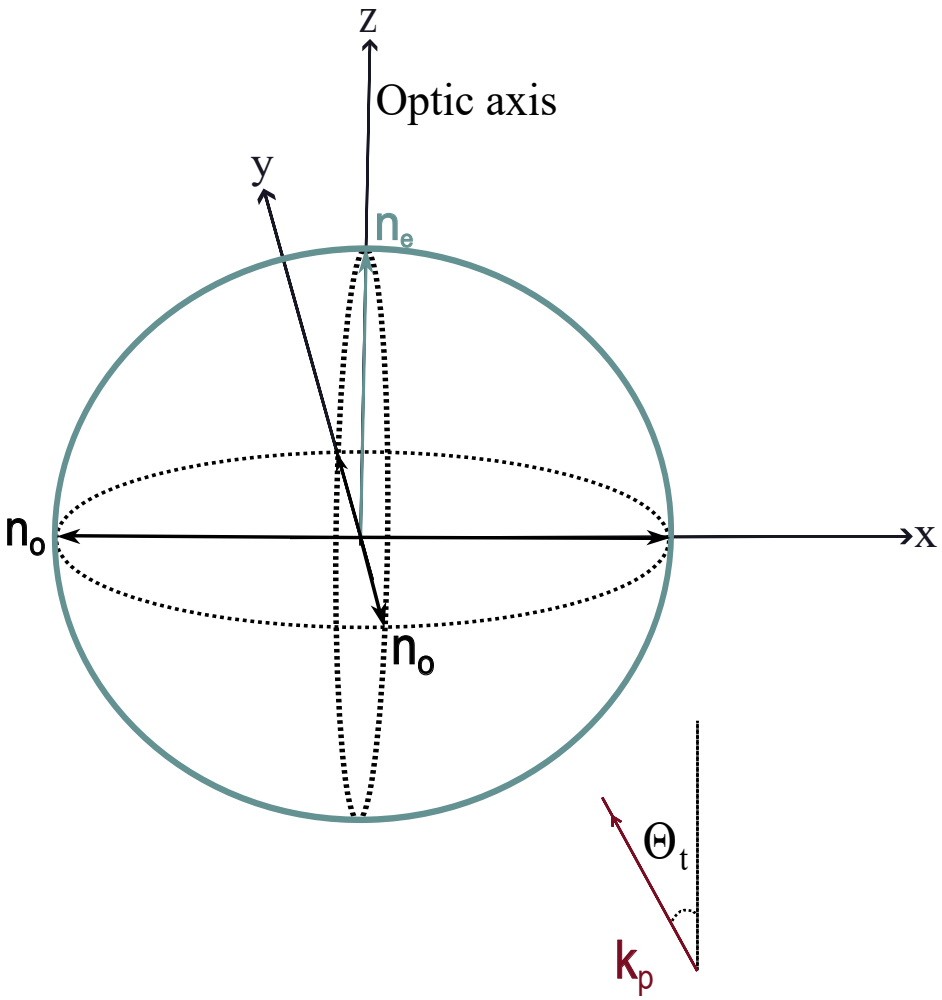

Figure 2.2: **Index ellipsoid of a uniaxial crystal.** The wavevector of the pump is represented by k_p, incident on the crystal at some tuning angle Θ_t.

In the case of SPDC, phase-matching can be achieved when either one or both of the generated fields have a polarisation different from that of the pump field. When one of the generated fields has polarisation different from that of the pump field, the photon pairs

are cross-polarised, and the interaction is denoted as o-eo and referred to as Type-II. In contrast, when both generated fields have the same polarisation, the interaction is called Type-I and is the one considered here. There are two possible configurations for Type-I: either the pump field experiences the extraordinary index, while the signal and idler fields are subject to the ordinary index, or vice versa. Those are denoted e-oo and o-ee, respectively, and we concern ourselves with the first. Light with a polarisation component along the optic axis will experience an extraordinary refractive index. In contrast, light with a perpendicular polarisation component relative to the optic axis will experience an ordinary refractive index. If the incoming light is going through the crystal at an angle with the optic axis, then:

$$\frac{1}{n^2(\theta)} = \frac{cos^2(\theta)}{n_o^2} + \frac{sin^2(\theta)}{n_e^2} \tag{2.22}$$

with $n^2(\theta)$ being the refractive index value that the light will experience. When signal and idler photons have the same frequency, the interaction is called degenerate, and when they also propagate in the same direction as the pump photon, the phase-matching is called collinear. For the generation of degenerate signal and idler photons, the relationship $n_e(\lambda_p) = n_o(2\lambda_p)$ needs to hold. The tuning angle θ_t between the crystal optic axis and the pump k_p can be adjusted to achieve collinear phase matching and can be calculated using:

$$\frac{n_o^2(\lambda_p)n_e^2(\lambda_p)}{n_e^2(\lambda_p)cos^2(\theta_t) + n_o^2(\lambda_p)sin^2(\theta_t)} = n_o(2\lambda) \tag{2.23}$$

and solving for θ_t. But firstly, the wavelength-dependent refractive indices $n_o^2(\lambda)$ and $n_e^2(\lambda)$ need to be calculated using the Sellmeier equations for a BBO crystal [52]:

$$n_o^2 = 2.7359 + \frac{0.01878}{\lambda^2 - 0.01822} - 0.01354\lambda^2 \tag{2.24}$$

$$n_e^2 = 2.3753 + \frac{0.01224}{\lambda^2 - 0.01667} - 0.01516\lambda^2 \tag{2.25}$$

for a pump wavelength at $\lambda_p = 515$ nm. By solving Eq.2.23 we find the tuning angle equal to $\theta_t = 23.32$. Utilising the birefringence of the nonlinear medium to achieve efficient upconversion is called critical phase-matching, but this technique is susceptible to walk-off. As a wave propagates through the crystal, its Poynting vector, which represents the direction of the wave's energy flux, can deviate from the wavevector of the wave [53]. This will result in an intensity distribution that deviates from the interaction direction and can, therefore, reduce the effective interaction length in the crystal. To reduce walk-off, another phase-matching technique can be employed, which involves temperature-tuning the crystal to alter its birefringent properties [54]. This is referred to as non-critical phase

matching.

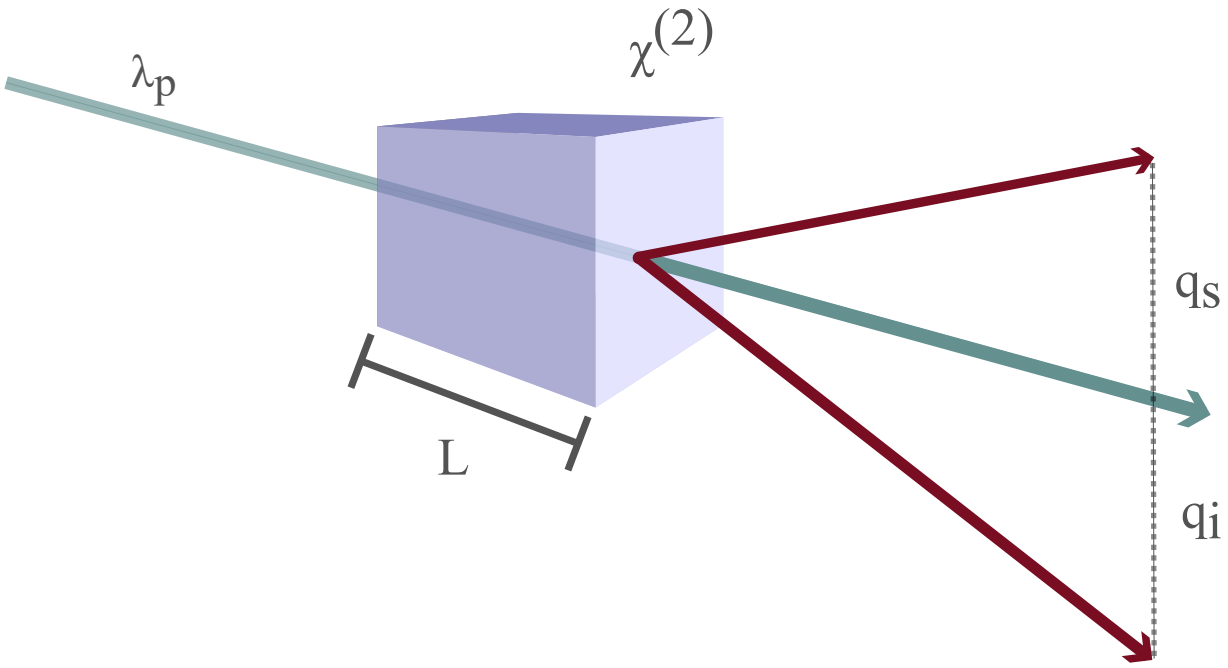

Figure 2.3: **Type-I Parametric Down Conversion.**Produced signal and idler field are represented by their momentum vectors q_s and q_i, respectively.

It is essential to state that the calculated tuning angle θ_t corresponds to the degenerate phase-matching condition, where the signal and idler photons have equal frequencies, each equal to half the pump frequency $\omega_p/2$. A collinear geometry was assumed between the pump and generated fields. While this angle optimises phase matching for degenerate down-conversion, the nonlinear process still supports phase matching for a range of non-degenerate frequency pairs, especially when the pump has a finite spectral width, which is the case experimentally.

A non-collinear geometry between the pump and the generated fields can be achieved by further tuning the angle. Because of a broad phase-matching bandwidth, down-converted photons with frequencies different from $\omega_p/2$ can also be generated efficiently. The phase-matched PDC will have a conical geometry, as depicted in Figure 2.3. Then, the momentum phase-matching condition as described by Eq.2.9 leads to an interesting consequence on the process, where signal and idler photons need to propagate on opposing sides of the pump beam. This brings us back to the concept of correlations introduced in the previous section. Signal and idler photons not only have a frequency spectrum, but that spectrum is also mapped spatially through phase-matching conditions. By spectrally measuring the idler photon, the signal pair's frequency state will collapse, and its position will also be known. This is what we refer to as spatiotemporal entanglement.

2.3 Sum-frequency generation

Second harmonic generation is sometimes considered the inverse process of PDC. It is a special case of Sum-Frequency Generation, in which pump photons with the same energy and momentum interact in the nonlinear medium to generate a third wave with twice the energy. Here, we consider SFG since the entangled photons from each pair used to stimulate SFG can be nondegenerate and/or have different transverse spatial frequencies. Developing a theoretical model for eSFG is beyond the scope of this thesis; however, during our experimental investigations, our collaborator Alessandra Gatti developed a model to describe the effect of SFG when entangled photons are used to pump the process. The model aligns with the experimental data; therefore, I attempt to explain it in this section [37].

The model I will describe is built upon a previous description of PDC, where a quasi-stationary model was used to derive expressions predicting changes in PDC characteristics at different gain levels [39, 55]. A complete derivation can be found in [37]. We start by using a Gaussian amplitude profile for the pump beam that produces SV:

$$A_p(\vec{\xi}) = e^{(-\frac{x^2+y^2}{D_p^2})} e^{-\frac{t^2}{\tau_p^2}} \tag{2.26}$$

where D_p and τ_p are the spatial and temporal widths of the pump field, respectively. Then the number of SV photons per pulse is defined as:

$$N_{SV} = \int d_3\vec{\xi} F_{coh}(\vec{\xi}) \cdot \int \frac{d_3\vec{w}}{(2\pi)^3} |V(\vec{w})|^2 \tag{2.27}$$

where:

$$\vec{\xi} := (x, y, t) = (\vec{r}, t) \tag{2.28}$$

$$\vec{w} := (q_x, q_y, \Omega) \tag{2.29}$$

$$\vec{w} \cdot \vec{\xi} := xq_x + yq_y - \Omega t \tag{2.30}$$

the space-time coordinates, with $\vec{w}$ the Fourier conjugate of $\vec{\xi}$. The above Eq.2.26 was obtained by integrating over the equation:

$$I_{PDC}(\vec{\xi}) = F_{coh}(\vec{\xi}) \int \frac{d^3w}{(2\pi)^2} |V(\vec{w})|^2 \tag{2.31}$$

which expresses the intensity distribution of the PDC pulse. Equation 2.27 has two terms, both with interesting properties. The photon flux density profile of the PDC field $F_{coh}(\vec{\xi})$

is described by:

$$F_{coh}(\vec{\xi}) = \frac{\sinh^2[2\mathrm{gA_p}(\tilde{\xi})]}{\sinh(2\mathrm{g})} \tag{2.32}$$

As seen from the above expression, the photon flux density profile depends on the gain of the process $\mathrm{g} = \chi l_c |a_p|$, where $|a_p|^2$ is the peak photon flux density of the pump. This was shown in [39], where at low gain($\mathrm{g} << 1$) the photon flux density profile will coincide with that of the pump $|A_P(\vec{\xi})|^2$. At high gain, though, $F_{coh}(\vec{\xi})$ will shrink at a rate equivalent to $\sqrt{\tanh(\mathrm{g})/\mathrm{g}}$. Another parameter of the SV that changes with changing gain is the PDC one-photon probability distribution in Fourier mode $|V(\vec{w})|^2$, which is defined as:

$$|V(\vec{w})|^2 = \left|\mathrm{g}\frac{\sinh(\Gamma(\tilde{\mathrm{w}}))}{\Gamma(\vec{w})}\right|^2 \tag{2.33}$$

where $\Gamma = \sqrt{\mathrm{g}^2 - \frac{[D(\vec{w},-\vec{w})l_c]^2}{4}}$. We can therefore see that the one-photon probability distribution will peak at regions where the phase-matching is realised since Γ depends on the phase-mismatch $D(\vec{w},-\vec{w}) = k_{SV,z}(\vec{w}) + k_{SV,z}(-\vec{w}) + k_{p,z}(0)$, with $k_{i,z}$ the longitudinal wave vector of the i-th field. Now we can define the quantum field operator for the input PDC field at the nonlinear crystal where SFG occurs:

$$\hat{B}_j(\vec{r},t,z) = \int \frac{d^2\vec{q}}{2\pi} \int \frac{d\Omega}{\sqrt{2\pi}} e^{i\vec{q}\cdot\vec{r}} e^{-\Omega t} \hat{B}_j(\vec{q},\Omega,z) \tag{2.34}$$

with $\vec{r} = x\vec{e_x} + y\vec{e_y}$ the position in the transverse plane. In principle, an evolution equation should be coupled with the equation of the pump PDC field, but since the PDC input is weak, its nonlinear depletion can be neglected. This allows us to solve the evolution equation perturbatively, where the SFG field $\hat{A}(\vec{w_0})$ is related to input PDC field such as $\hat{A}_2(\vec{w}) := \hat{B}_2(\vec{w}, z = l_c)$, and hence:

$$\hat{A}_2(\vec{w_0}) = e^{ik_2(\vec{w_0})l_c'}\left[\hat{B}_2(\vec{w_0}) + \int \frac{d^3w}{(2\pi)^{\frac{3}{2}}} \hat{B}_1(\vec{w})\hat{B}_1(\vec{w_0}-\vec{w})\Phi_{SFG}(\vec{w},\vec{w_0}-\vec{w})\right] \tag{2.35}$$

where

$$\Phi_{SFG}(\vec{w},\vec{w'}) = -\frac{\chi l_c}{2}\mathrm{sinc}\left[\frac{D(\vec{w},\vec{w'})l_c}{2} e^{iD(\vec{w},\vec{w'})\frac{l_c}{2}}\right] \tag{2.36}$$

the probability amplitude of the microscopic upconversion process $\vec{w},\vec{w'} \rightarrow \vec{w}+\vec{w'}$. Finally, we use the operator in Eq.2.35 to obtain the spatiotemporal distribution of the SFG photon flux:

$$I_{SH}(\vec{\xi}) = \left\langle \hat{A}_2^\dagger(\vec{\xi})\hat{A}_2(\vec{\xi})\right\rangle = I_{SFG}^{(E)}(\vec{\xi}) + I_{SFG}^{(inc)}(\vec{\xi}) \tag{2.37}$$

where it was assumed that both nonlinear crystals, one for the PDC generation and the other for the SFG, have the same phase-matching condition. The above equation has two components, with the first, $I_{SFG}^{(E)}(\vec{\xi})$, referred to as the coherent component, indicating the upconversion of entangled photons from the PDC. The second term is the incoherent component $I_{SFG}^{(inc)}(\vec{\xi})$, resulting from the recombination of non-entangled photon pairs. The coherent component is considered to be the reconstruction of the initial pump beam that generated the entangled photons, since it originates from entangled photons created from the same pump photon. The component will also contain the interaction of entangled photons described by the higher-order terms in Eq.2.14, which were generated in the stimulated regime of PDC. Of course, the interaction of non-entangled photons is still possible, and the recombination of those photons will give rise to the incoherent component, since they lack a fixed phase relation between them. These two components not only have different spatiotemporal characteristics but also scale differently with the PDC photon flux. In general:

$$N_{SFG} = \sigma_1^E N_{SV} + \sigma_2^E N_{SV}^2 + \sigma_2^{inc} N_{SV}^2 \tag{2.38}$$

where σ_1^E, σ_2^E and σ_2^{inc} the coefficients of the interaction. It is important to emphasise the two second-order terms of the above equation. The coherent contribution scales in the same manner as the incoherent one at higher gains, signifying its contribution to the effect in the high-gain regime, without it being overwhelmed by the incoherent signal. In [37], the above equation was compared with the classical rate equation for SFG $N_{SFG}^{(cl)} = \sigma_{cl} N_p^2$ where N_p was assumed to have the same amount of classical photons per pulse as the PDC source on the nonlinear crystal, so that $N_p = N_{SV}$. Interestingly, the results showed a more efficient quantum SFG for g >> 1, indicating that a quantum advantage can be observed at much higher gains than previously thought possible. Moreover, the incoherent contribution is expected to enhance the overall efficiency of the quantum effect when the experimental setup is appropriately designed. More specifically, the crystal where SFG takes place needs to be as short as possible to achieve a large phase-matching bandwidth. This would result in a large bandwidth of the PDC spectrum getting upconverted coherently. Secondly, dispersion can degrade the localisation of the entangled photons, thereby reducing the process efficiency. Such a drop in efficiency can also be observed if the spatial localisation of the photons is not optimal, due to discrepancies in the imaging system used to bring the entangled photons together for interaction in the nonlinear crystal. We take into account all those caveats during the design of the experimental setup to study the effect, and, given the theoretical model's prediction of a more efficient entangled SFG rate than the classical SFG rate, we wanted to study this experimentally, too. In the next section, I will provide a critical overview of the existing literature on the topic.

2.4 Overview of literature on entangled two-photon effects

During the second half of the 20th century, a significant portion of the scientific community in optics and photonics shifted its focus. Entangled photon sources could finally become available in every lab by pumping a nonlinear crystal with laser radiation, and theoretical work on how their implications could alter current technologies was booming [56, 57]. One phenomenon theorised to benefit from the entanglement in nonclassical radiation was multi-photon absorption. More specifically, the rate of excitation of multiphoton effects was described as proportional to the correlation function of the incident field [58]. Entangled photons are guaranteed to exist in pairs, with high absorption probability, and therefore, by 1990, the first theoretical works on entangled two-photon absorption were published [4, 56].

The first experimental observation of the effect was reported by Georgiades et al. in 1995, who investigated the rate of excitation in trapped atomic Cesium and observed a linear scaling of the excited fluorescence [5]. It was two years later that Teich, Saleh and Fei produced two subsequent works that would describe the effect in terms of the rate equation:

$$R = R_e + R_r = \sigma_e \phi + \delta_r \phi^2 \tag{2.39}$$

where ϕ is the entangled photon pair flux and σ_e and δ_r are the coefficients of absorption. They were hence the first to correlate the effect with the absorption coefficients [59, 60]. They expand on this by introducing the expression $\sigma_e = \delta_r / 2 A_e T_e$, with T_e and A_e the entanglement time and area, respectively, as mentioned earlier. These expressions are still used by researchers today to describe the effect.

More research on the effect came in the early 2000s. Barak Dayan, Avi Pe'er, Asher A. Friesem, and Yaron Silberberg published three pieces of work, in which, instead of examining the scaling of the process, they mostly studied the effects of temporal correlations. They used broadband entangled photon pairs to excite fluorescence in a Rb cell, while the signal and idler paths were spatially separated. A delay was introduced, and upon scanning, they observed a peak in the eTPA, indicating temporal correlations [61]. While this research didn't include fluorescence scaling, the pair of papers they published later did. This time, they utilised SFG to study both the temporal correlations and the process's rate. They showed that when the bandwidth of the SFG crystal used matches that of the PDC, then the SFG process could be considered a means of measuring photon-

coincidences [62]. The same setup was used to demonstrate the linear scaling of eSFG at low SPDC gain, with 0.18 photons per mode. To confirm the observed quantum effect, they introduced losses into their entangled state, which caused eSFG to scale quadratically. In the later chapters of this thesis, this measurement and its implications are discussed in more detail [63]. Dayan later published a theoretical work on entangled two-photon interactions. He discusses both coherent and incoherent contributions, as well as their spectral properties [64].

A large body of work on eTPA in molecular samples has been produced by the group of Goodson at the University of Michigan. In most of their work, they generate entangled photons via Type-II SPDC and first tested porphyrin dendrimers [65]. They observed both the linear and the quadratic scaling in their fluorescence rate. They do so for different entanglement times, with a decreasing fluorescence rate efficiency as T_e increases. Although this observation is as expected, there are inconsistencies with it. They claim to change the entanglement times by introducing quartz plates of varying thicknesses. While it is true that in Type-II SPDC the entanglement time of the photon pairs is affected by the fact that signal and idler have different polarisations, and hence exit the crystal at various speeds, introducing an additional delay does not alter the entanglement time. Therefore, what is being measured is the externally introduced delay itself, not a change in the entanglement time, which is a fundamental property of the PDC state. In essence, the entanglement time corresponds to the width of the second-order correlation function, which characterises the photon statistics and coherence of the light source. This parameter is intrinsic and unaffected by dispersion. Consequently, the observed reduction in the efficiency of the entangled two-photon absorption (eTPA) process arises from the photon pairs failing to arrive simultaneously at the sample, rather than any change in their entanglement properties. In their later work, they tested the effect of spatial separation between the rings produced by Type-II phase-matching. The results showed that when the rings intersected, the eTPA response was higher. This, of course, can be explained by the fact that when idler and signal photons are overlapping, they are characterised by a higher degree of entanglement [66].

Experiments showing the dependence of the eTPA rate on the concentration of the sample were done in Zinc Tetraphenylporphyrin and Rhodamine B by Juan P. Villabona-Monsalve et.al. [67]. Similar work was produced later by Tabakaev et. al. [68]. Although they observed the linear scaling, Villabona-Monsalve et al. paper lacked measurements to verify that the observed effect is indeed a result of the interaction of entangled photons, measurements absent from Goodson's experiments, too. This is one of the main arguments against these early publications of eTPA, as others have since stated. More specifically, researchers from NIST in Colorado tried to detect eTPA signals from zinc tetraphenylpor-

phyrin, following Goodson's protocol in [69]. They concluded that the eTPA signal could have been mistaken for linear effects since they did not observe any eTPA signal [70]. The same group later published the paper titled "Hot-Band Absorption Can Mimic Entangled Two-Photon Absorption" [7]. As suggested by the title of their paper, the one-photon effect can lead to an overestimation of the eTPA signal and occurs when the incident radiation spectrum on the sample is broad. This can stimulate transitions in the vibronic manifold of the ground state. This series of publications demonstrates that replicating the experiments in molecular samples can be challenging. In general, discrepancies arise when measuring absorption coefficients, as results from different groups do not match. In some cases, the molecules used are not common and therefore not easily reproducible.

Theoretical and experimental work has been published in the early 2020s by a group at the University of Colorado [71–75]. Their theoretical work primarily focuses on eTPA, and they explain that without proper spectral shaping of the photon pairs, the quantum enhancement will be less pronounced. They suggest using systems with narrow-band transitions so that the frequency anticorrelations present in the signal and idler would be most effective. In their experimental paper, they utilise SFG to optimise their setup before trying to measure eTPA from Rhodamine 6G. However, they reported no eTPA in the sample, concluding that any eTPA enhancement should be much lower than previously reported.

In summary, the inconsistencies in the measured quantum-enhanced absorption cross sections σ_e, alongside the absence of any signal as reported in [70] and [73], indicate that any claim of observing the effect should be done with careful crafting of the experimental setup to rule out any other effects that can occur and overshadow eTPA. So far, there has been too much attention paid to measuring absorption coefficients and not enough to carefully optimising the quantum experiment. From the work presented by Juan P. Villabona-Monsalve et.al. [67], it is clear that there is a strong dependence on the concentration of the sample. The response of fluorophores can also vary with temperature, contributing to discrepancies in the literature. We concern ourselves with eSFG to study two-photon interactions, and in doing so, we eliminate any dependencies and one-photon effects that would lead to overestimating the measured signal. Therefore, it is also essential to report research that examines the effect of eSFG, beyond the expected efficiency enhancement.

Multiphoton processes are sensitive to the statistics of the pump that is used to generate them. Such multiphoton processes can be studied in Second Harmonic Generation (SHG), Third Harmonic Generation (THG) and Fourth Harmonic Generation (FHG), as demonstrated by Spasibko et al. [76]. Multiphoton effects of the n_{th} order will scale as the n_{th} order correlation function. Due to the ultrafast number fluctuations of the SV

a "superbunched" behaviour can be observed, and thus harmonic generation is expected to produce more signal. In [76], they compared the harmonics generation from SV with a pseudo-coherent source, by reducing the photon-number fluctuations, with the latter showing less production of nonlinear signal. Since then, the group has produced additional work by studying the upconversion of PDC by eSFG [77]. By examining the spectrum of the upconversion signal, they found that a more efficient signal is obtained when PDC is focused at the surface of the crystal, rather than within its bulk. In the same paper, both contributions of eSFG were studied spectrally, with the incoherent contribution being broad around a narrow peak that corresponds to the coherent contribution. The total number of modes produced in the setup was determined by calculating the ratio of the incoherent to the coherent spectrum, demonstrating that the correlation characteristics of the PDC source can be inferred from its upconversion.

A similar investigation was performed by O. Jedrkiewicz et al. in [78]. In contrast to previous investigations, this study employs an achromatic imaging system to image the PDC to the surface of the nonlinear crystal where eSFG occurs. They showed that when the PDC is filtered by a pinhole in the far field, the temporal correlations broaden. This highlights the non-factorability of PDC, as filtering in the space alters temporal correlations—a concept introduced earlier in this chapter. Lastly, they demonstrated that errors in the imaging system can compromise the efficiency of eSFG production by displacing the PDC focus from its ideal position, broadening the eSFG spectrum. This is an important insight from this work, as most early research on two-photon effects appears to give little regard to the two-photon state, using controversial methods to measure fluorescence and focusing primarily on the absorption coefficients obtained. Following the work of O. Jedrkiewicz et al., A. Gatti et al. described the effect of PDC upconversion using a three-dimensional model that incorporates changes in spatiotemporal correlations across different PDC regimes. The model makes quantitative predictions that agree with our experimental results, and I use it in this thesis to both characterise the PDC source and analyse the enhancement seen in quantum SFG.

Here, I attempted to summarise the most important work on entangled two-photon processes by presenting the experimental challenges and the existing doubts that scientists face about the enhancement of the nonlinear effects. A fundamental question remains unanswered: is the correlations or the entanglement responsible for the observed enhancement? In general, entanglement and correlations are intertwined properties of a quantum system, and therefore, to answer this question, we need to take a more fundamental look at the processes involved.

In conventional classical optics, the process of SFG or TPA scales quadratically with light intensity, reflecting the fact that two independent photons must arrive at the

interaction region within a short temporal window. Such processes are sensitive to photon statistics, and their rate will always be proportional to:

$$g^{(2)} = \frac{\hat{a}^\dagger \hat{a}^\dagger \hat{a}\hat{a}}{< \hat{a}^\dagger \hat{a} >< \hat{a}^\dagger \hat{a} >} \tag{2.40}$$

where $\hat{a}^\dagger$ and $\hat{a}$ are the photon creation and annihilation operators. In general, $g^{(2)}$ is defined as the second-order correlation function and can indicate the degree of correlation between photons detected at time t and those detected at time $t + \delta t$. For a single-mode field, the two-photon rate then becomes:

$$R = \kappa n^2 g^{(2)} = \kappa \hat{a}^\dagger \hat{a}^\dagger \hat{a}\hat{a} \tag{2.41}$$

where $n =< \hat{a}^\dagger \hat{a} >$ is the mean photon number and κ a constant indicating the strength of the nonlinear interactions. Now, depending on the radiation used to pump the process, $g^{(2)}$ will differ. For example, coherent laser radiation has a $g^{(2)}$ value of $g^{(2)} = 1$, while thermal light has a value of $g^{(2)} = 2$ and as any radiation with $g^{(2)} > 1$ it can exhibit the peculiar effect of photon bunching. This effect was reported by Hanbury Brown and Twiss (HBT) in their notable paper [79], and has become one of the cornerstones of early quantum optics. With TPA and SFG scaling linearly on the second-order correlation function, it is expected that they will produce twice as many photons when stimulated with thermal light sources as with coherent light. This was experimentally confirmed by Jechow, A. et al. [80], while other effects expected to be observed or enhanced by quantum radiation have also been demonstrated with thermal radiation [81, 82].

The $g^{(2)}$ value of thermal light reveals an important consequence: that correlations are not uniquely quantum and classical light fields, such as thermal light, can exhibit photon number correlations. As a result, part of the enhancement observed in eTPA and eSFG can be attributed to the fact that entangled photons naturally exhibit strong time–energy correlations.

However, the energy entanglement between the signal and idler photon can be engineered to match the energy of a two-photon transition in fluorophores. More specifically, a unique signature of eTPA is the ability to access and study different excitation paths inside the molecule. By engineering the entanglement time of the entangled state, the transition from the ground state to the virtual state, and then to the final state can be controlled, and the frequencies of the molecule's intermediate states can be revealed. This technique, known as virtual state spectroscopy [83], can offer unique control over the molecule's different pathways and implies the existence of quantum coherence between different two-photon excitation pathways. Entangled two-photon events also rely on the indistinguishability of the photon pairs. Research performed at the University of Michi-

gan revealed that overlap between the two rings of Type-II SPDCN increases the eTPA cross-section, with the overlapping photons in a superposition of polarisations [66].

As mentioned previously in this section, the coefficient of absorption in eTPA is:

$$\sigma_{\mathrm{e}} = \frac{\delta_{\mathrm{r}}}{\mathrm{T_e A_e}} \tag{2.42}$$

with δ_r the classical absorption coefficient of the two-photon absorber and T_e and A_e the entanglement time and area, respectively. Small values of T_e and A_e are what ultimately cause the enhancement seen in eTPA, with T_e ensuring that the idler photon is present to be absorbed before the virtual state decays, after it has been excited by the signal photon. A rise in a linear scaling between the generated field and the photon-pair flux is expected at the low gain of the SPDC. This can offer a distinction between two-photon effects produced by carefully engineered classical beams (thermal radiation) and those produced by entangled photons, since the linear regime hasn't been observed for any other source of light. In the case of eSFG, in the low-gain regime of PDC, distinct photon pairs arrive at the crystal having a broad bandwidth. All up-converted correlated pairs will produce SFG photons back at the narrow wavelength of the pump, and their properties are determined by the joint spectral amplitude of the two-photon state rather than by the individual photon spectra. As described by Dayan, this shows the quantum coherence of the entangled state, with many frequency combinations contributing coherently to the upconversion amplitude [63].

In summary, the enhanced efficiency observed in two-photon effects arises from a combination of strong correlations and genuine quantum entanglement. Using light that exceeds the second-order correlation function of quantum radiation, such as a spectrally narrow supercontinuum, will enhance the signal of two-photon effects. This enhancement might even exceed that seen with photon pairs from SPDC, since the signal rate scales linearly with $g^{(2)}$, indicating that correlations are necessary, and they ensure that photon pairs arrive within the temporal and spectral windows required for the nonlinear interaction. However, linear scaling won't be present, as it is a unique feature of entanglement. It provides the distinctly nonclassical contribution by preserving coherent superpositions of two-photon excitation and enabling linear scaling and interference effects that cannot be replicated by any classical light field with the same intensity. Thus, while correlations constitute the immediate mechanism, entanglement is the fundamental reason why these quantum light sources can outperform classical ones under appropriate conditions.

2.5 Conclusion

In this chapter, a review of the theoretical background of second-order nonlinear processes has been provided. More specifically, the mathematical formulation of PDC was described and how phase-matching governs the process, and its nonclassical features were discussed. A similar overview was provided for eSFG. More specifically, the theoretical work of A. Gatti et al. was discussed, which is the theoretical model we use to quantify the results presented in this thesis. Finally, a summary of the existing literature on the subject was provided. In the following chapters, I will introduce the work on shaping the PDC state to optimise it for the SFG effect.

CHAPTER 3

Entangled Sum-Frequency Generation and comparison with classical SFG

3.1 Introduction

Entangled Sum Frequency Generation is the phenomenon where a pair of entangled photons is combined in a nonlinear medium to produce radiation at the sum of their frequencies. While the mechanism for this interaction is similar to that of the classical SFG, the spatiotemporal correlations present in the entangled photon pairs can enhance the process, as they behave as one photon when interacting with matter. This causes the produced radiation to scale linearly with the input rate of the entangled photon pair at low parametric down-conversion gain. Therefore, using entangled pairs to pump the process enables higher light generation rates at low input pump powers, with applications in metrology, as it allows measurements at low light levels. Previous research on the topic suggests that any improvement in the process stops after the low-gain region of PDC. Here, we extend our research on the high-gain of PDC to investigate what actually happens, as the quantum contribution from biphotons should still be present at higher intensities than those previously considered. The quantum light that produces SFG can impart a unique signature on the signal, providing insight into the nature of the pump-photon statistics. More specifically, at the higher gain PDC regime, the accidental recombination of photon pairs that are not entangled with each other will result in the production of incoherent radiation that is not present in the phase-matched classical interaction. We decided not to overlook the incoherent component, and its contribution will be discussed in the results section of this chapter.

Another objective of this work was to provide a comparison of the entangled process with its classical counterpart, thereby setting the limitations of the observed enhancement. Since we are targeting a potential improvement in applications that rely on two-photon

processes, i.e., imaging, we decided to compare the generation rate of SFG when classical fields (coherent laser pulses) are employed to pump the process. Such a comparison is not trivial, as radiation produced by SPDC has properties inherently different from those of a classical laser pulse, aside from the presence of correlations. Therefore, the comparison needed to be conducted in a way that avoided discrepancies that could lead to favouring either case. To this end, the SV generated was characterised, and the parameters of the classical pump used to create SFG were matched accordingly. More specifically, we decided to maintain the same intensities in our pump fields.

3.2 Aparatus and measurement

3.2.1 Aparatus

Similar to classical excitation, the pump beam interacts with the nonlinear medium and any produced signal is collected using refractive optics. Therefore, to produce eSFG, the first crystal, where the entangled pairs are generated, is imaged into the second nonlinear crystal where eSFG takes place. This ensures that the signal and idler photons produced by PDC converge into a volume where they can interact simultaneously to produce eSFG.

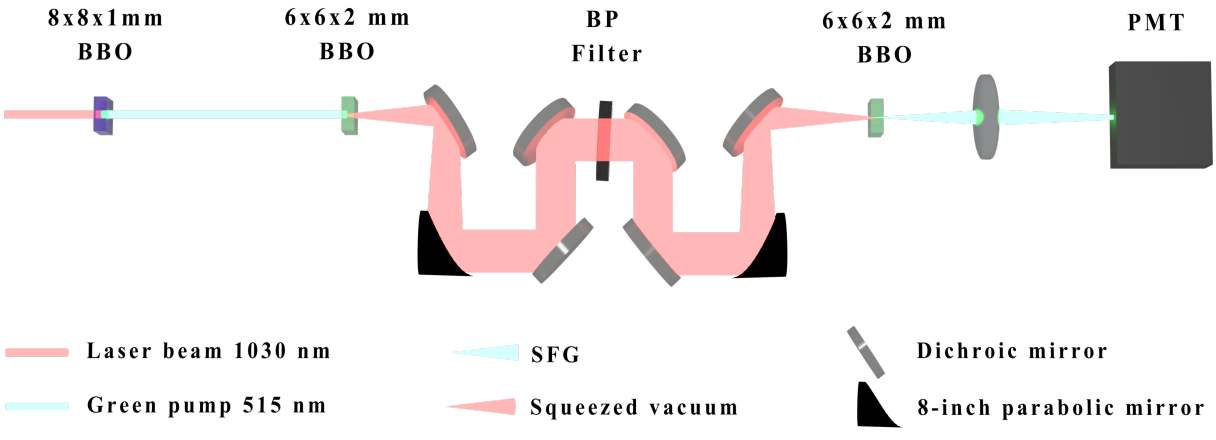

Figure 3.1: **Experimental Setup for eSFG.** An infrared laser beam is delivered in an 8x8x1 mm BBO crystal to generate a second harmonic at 515 nm. The remaining 1030 nm laser beam is filtered using dichroic mirrors. The green beam acts as a pump for the entangled photons in the 6x6x2 mm BBO crystal. The bandpass filter selects the frequency range that undergoes SFG in the second 6x6x2 mm BBO crystal, which is mounted on a translation stage. Far-field filtering separates the entangled SFG component (eSFG) from the incoherent, non-entangled component, and the remaining eSFG is detected using the Photomultiplier Tube (PMT). The SV is filtered using bandpass filters (Not shown).

The setup used to investigate eSFG is shown in Figure 3.1. The source used for this experiment is Light Conversion's Carbide CB3, a Yb:KGW amplified laser with a maximum output power of 40 W, delivering 250 fs pulses at an output wavelength of 1030 nm. The laser can be operated at different repetition rates; for this research, it was operated at 200 kHz and 500 kHz, resulting in maximum pulse energies of 0.2 mJ and 0.08 mJ, respectively. The laser output was used as a pump in an 8x8x1 mm BBO crystal to generate second harmonic at 515 nm. To ensure highly efficient second-harmonic generation, the beam size was reduced using a Galilean telescope with magnification M=0.67, resulting in a pump beam size of a ≈1.3 mm Full Width at Half Maximum (FWHM). This ensured a conversion efficiency of 60% and 40% at both working repetition rates. Dichroic mirrors are used to filter out the infrared laser light (not shown in the figure) and to guide the second-harmonic generation into a 6x6x2 mm BBO crystal, where it serves as the pump beam for the entangled photons generated by PDC.

Unlike previous research performed on the subject, we wanted to generate a multimode PDC source. Modes are the spatiotemporal volume in which the entangled photon pairs are produced, and a higher number of them would enable us to achieve a larger number of entangled photon pairs [84]. This was especially important for the low gain of PDC, when the linear scaling of eSFG was expected to be observed. A bright source of photon pairs at the low gain of PDC could help us achieve a highly efficient eSFG that is measurable with commercially available detectors. To this end, another telescope was placed in front of the BBO crystal to enlarge the pump beam, thereby increasing the number of spatial modes. The telescope placed had a magnification of M=0.8 and was found to be optimal in balancing the high number of spatial modes that we wanted to generate with the high output power of the generated PDC. However, there were additional reasons this magnification was chosen.

A key reason for choosing that specific magnification was to avoid thermal effects. While the femtosecond pump allowed us to ensure efficient conversion, it had the potential to introduce unwanted nonlinear effects, such as Kerr lensing or self-phase modulation [85]. This led to an iterative process in which the influence of the nonlinear effects on the setup was evaluated. Of special interest was Kerr lensing, which can occur when a short optical pulse propagates through a nonlinear medium. Part of the beam can experience a nonlinear refractive index, which can cause it to focus. To examine whether this effect was occurring, the green pump was imaged with and without the PDC crystal in place, at different distances from the crystal, and with varying pulse energies. To avoid Kerr lensing altogether, it was necessary to increase the beam size of the 515 nm pump before it was sent to the PDC crystal. In the end, the pump beam had a beam size ≈ 1.6 mm (FWHM), a spectral bandwidth of 3 nm (FWHM) and a pulse duration of ≈185 fs.

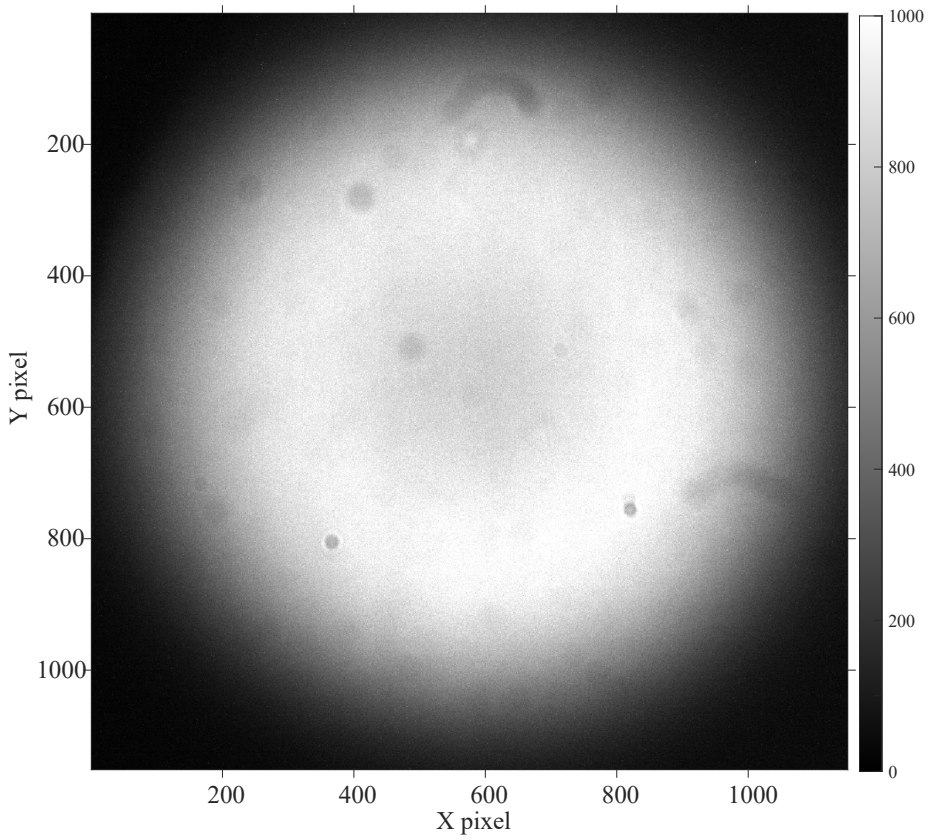

Figure 3.2: **PDC Far field** showing the non-collinear phase matching geometry of the PDC. Image taken with a 200 mm lens after the eSFG crystal at a distance of one focal length away.

To control the power of the PDC, an achromatic half-wave plate was placed in front of a thin-film polariser with an extinction ratio >1:200 on the pump beam path. The PDC radiation is then imaged into the second BBO crystal using two 8-inch equivalent focal lengths, 1-inch aperture, 90-degree off-axis parabolic silver mirrors with broadband ultrafast coating placed in a 4f configuration. The PDC beam path is guided using low-dispersion dichroic mirrors with high reflectivity (99.9% at an incidence angle of 45°) with a 300 nm bandwidth centred at 1030 nm and with high transmission (99%) at 515 nm. The seven dichroic mirrors filtered out the pump to a few pico Watts, but to ensure that no residual pump remains at the detection side, an 850 nm long pass optical filter (not shown in Figure 3.1) was placed at the far field of the PDC. Another bandpass filter was used at 23° with incidence to ensure that the PDC spectrum was cut symmetrically at 70 nm around 1030 nm. It is essential to state that our PDC source, with its far-field shown in Figure 3.2, was not bright enough to be visible by eye or a fluorescent alignment card. Hence, alignment was achieved using a camera placed after each mirror. The camera used was a Zyla 5.5 sCMOS, and it was mounted on a 1 m-long translation stage to ensure that the PDC radiation propagated in a straight line before the next mirror could be placed.

3.2.2 Imaging system

Choosing a suitable imaging system to image the generation plane of the parametric down-conversion field, i.e. the near field, at the second crystal where eSFG is produced was crucial. This would allow us to spatio-temporally reconstruct the entangled photons and bring them together in phase to interact coherently within the nonlinear crystal. However, it is challenging to pinpoint the exact location where the entangled photons are generated, as the interaction occurs within a thick crystal. It becomes even more difficult when we consider that throughout this research, we transition between the low-gain and high-gain regimes of the PDC, where the interaction within the crystal changes. At the low-gain regime, we generate photons throughout the entire length of the crystal. In contrast, in the high-gain regime, previously generated photons aid in the generation of new photons, resulting in most photon-pair production occurring at the end of the crystal. This changes the process's interaction length. Nevertheless, imaging of the near field was still essential to ensure the recombination of photon pairs and the preservation of their phases at the second crystal, where they would interact to produce eSFG.

The most suitable imaging system would be one that allows us to bring the signal and idler photons together without introducing any dispersion. For this reason, transmissive optics are avoided, and optical elements that can bend light while reflecting it, like spherical or parabolic mirrors, are favoured [78]. Parabolic mirrors in a 4f configuration are used for the results presented in this thesis, but other configurations were previously implemented before concluding that this was the best option. Initially, a 2-inch parabolic mirror with a hole in the centre was used. While this effectively filtered out the pump, it also meant the PDC's phase-matching conditions needed to be adjusted so that the photon pairs were emitted at a wider angle around the pump to avoid losing them as they propagated through the parabolic hole. This had a detrimental effect on the number of modes produced [84]. Concave mirrors were experimented with afterwards. Concave mirrors were placed in a 4f configuration. Still, the misalignment-induced aberrations resulted in the observation of two coherent eSFG peaks when the second BBO crystal was scanned across the PDC focus. These results, along with the reproduced Zemax schematic of the setup, are discussed in Appendix A.

Parabolic mirrors were used to image the near field of the PDC, requiring careful alignment. In addition to positioning the parabolic mirror one focal length away from the object to capture the reflected image correctly, the mirror must also be aligned so that it is the correct parent focal length away. Failing to match the parent focal length causes the object to be affected by coma aberrations and can also lead to unwanted changes in the spatial phase of the entangled radiation, which must be adequately mapped in the

up-conversion crystal for an unspoiled interaction of the correlated photons. To ensure the distances are correct, we have our first crystal on a translation stage to adjust the distance between it and the first parabolic mirror. The second parabolic mirror was also placed on a translation stage to optimise the distance between the two parabolic mirrors.

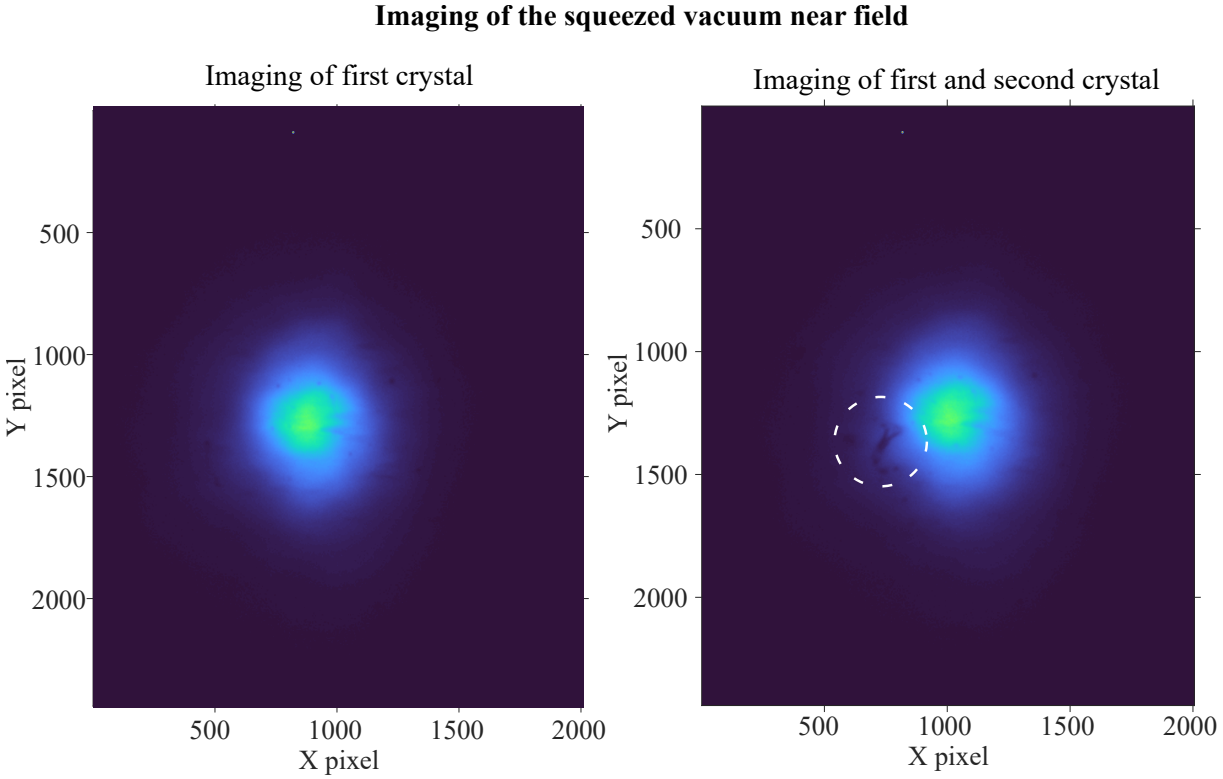

Figure 3.3: **Imaging the near-field of PDC**, with and without the second BBO crystal, where eSFG occurs, in place. When the generation plane of the entangled photons is properly imaged, dust particles on the crystal are reproduced in their true circular form, as observed in the image on the left. Dust particles and other details on the crystal that cannot be imaged properly appear as lines, and those are on the side of the first BBO crystal that is not imaged through the 4f system. This image was taken with a 100 mm lens placed two focal lengths from the imaging plane of the parabolic mirrors, where the second BBO crystal should be placed. To align the second crystal with the near-field imaging of the squeezed vacuum, we place it on a translation stage and move it along the imaging plane until its features come into sharp focus. This is shown in the image on the right, where such details on the second BBO are indicated using the dashed circle.

To minimise aberrations, the parabolic mirrors' orientations in the 4f configuration need to be "tip to tip" [86]. Therefore, the rest of the mirrors were set so that the reflection on the tip side of the first parabolic was reflected on the tip side of the second parabolic. Lastly, to ensure imaging of the near field of the PDC would be achieved without any aberrations, a laser pointer was aligned to follow the path of the PDC. The laser pointer emitted radiation at the same wavelength as the PDC; however, unlike the PDC, after passing through the second parabolic mirror, the laser pointer beam becomes collimated. When the beam is imaged at its collimation point, dust particles from the optics are also

imaged. If the alignment of the second parabolic mirror were incorrect, then those details would be affected by aberrations. Otherwise, they would appear as perfect circles. The resulting re-imaging of the PDC near-field after the 4f system is shown in Figure 3.3, showing how the squeezed vacuum generated by the first BBO crystal is imaged using the parabolic mirrors on the second BBO crystal, where SFG is generated.

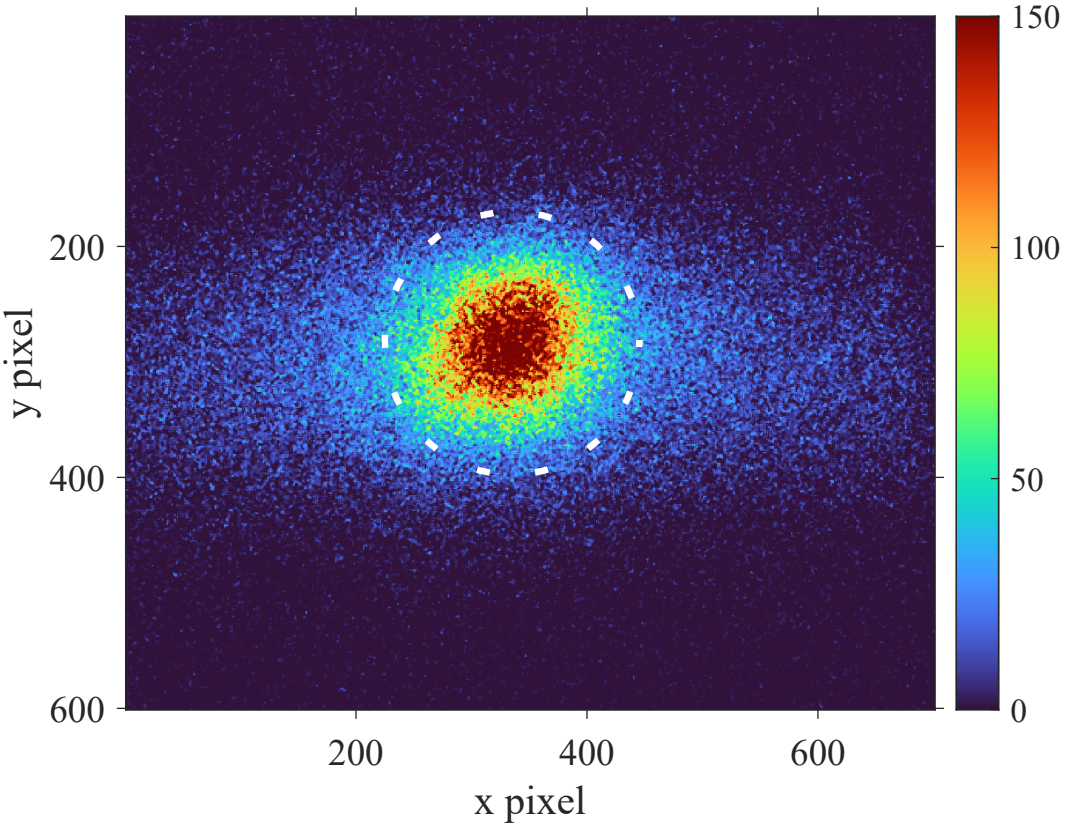

Figure 3.4: **Far field of eSFG** showing both the coherent beam formed by the correlated photons (indicated by the dashed circle) and the incoherent radiation surrounding it. The coherent eSFG beam shows some ellipticity. This ellipticity is also present in the PDC green pump beam. This is indicative of the fact that eSFG generated by entangled photons is the reconstruction of the pump beam used to generate them.

When signal and idler photons produced in the same mode combine in the BBO crystal, they interact as a single particle and give rise to a linear eSFG response. However, interactions between photons generated in different modes can still occur, resulting in an incoherent SFG signal. The incoherent signal lacks the correct momentum properties to form a beam and is therefore emitted in an expanding geometry alongside the primary coherent eSFG signal. The coherent response will emerge only when both the correct phase-matching condition is met on the up-conversion crystal (needs to match the phase-

matching of the first crystal) and the proper position of the crystal at the imaging plane of the parabolic mirrors are met simultaneously. Otherwise, only the incoherent SFG can be observed, as elements that produce it can still interact in the nonlinear crystal. To ensure that the crystal was placed at the correct distance, it was positioned on a motorised translation stage with a 25 mm range. To achieve phase matching, the crystal holder was mounted on a precision rotation stage with 5 arcmin resolution. To detect the signal, a 200 mm far-field lens was placed after the eSFG crystal, and the same Zyla 5.5 sCMOS camera, with an efficiency of 60% at 515 nm, was used to image the radiation. Phase matching and the crystal position were tuned simultaneously until a coherent spot appeared, as shown in Figure 3.4.

We wanted to isolate the coherent eSFG contribution. To this end, a telescope was built and an iris was inserted at the far field of the SFG (not shown in the setup Figure 3.1). With the iris closed, the incoherent signal that surrounds the eSFG was rejected. The remaining radiation is focused on the PMT (H16722P-40, Hamamatsu), which has a 40% quantum efficiency at 515 nm. Dichroic mirrors that filter out PDC radiation while reflecting SFG were used to deliver SFG to the PMT. Lastly, a short-pass 600 nm filter and a 10 nm bandpass filter centred at 515 nm were used to ensure that any down-converted radiation was removed before detection.

3.2.3 Crystal selection

Even if the beam was increased to avoid adverse nonlinear effects, the PDC crystal needed to have a high damage threshold, as the pump peak power density was calculated to be around 4.50×10^{10} W/cm^2. BBO was selected as it offers a significant nonlinear coefficient and a high damage threshold. However, a BBO crystal was not the first choice for this experiment. Initially, a 6x6x2 mm critically phase-matched LBO was used to generate the entangled photons. However, when imaging the near field of the entangled photons onto the second up-conversion crystal, a periodic structure was observed overlaying the Gaussian PDC beam. This structure originated from damage to the crystal's anti-reflective coating, as shown in Appendix A. This hindered our ability to properly reconstruct the generation plane of the PDC at the up-conversion crystal. Another challenge was posed by the heating oven in which the crystal had to be placed. To achieve the desired phase matching, the crystal's tuning temperature was set to 160 °C. While the crystal oven could reach those temperatures, it would overheat due to the metal shielding surrounding it, which was placed to block background radiation and scattering during SFG signal measurements. Therefore, it was decided to move from non-critically phase-matched crystals to avoid these thermal effects. In the remainder of this section, I will describe how the parameters

of the BBO crystal were selected.

It was essential to consider the crystal length. A longer crystal results in higher efficiency due to the increased interaction volume, but the pulse width of the pump beam may restrict the interaction throughout the entire length of the crystal. When ultrafast pulses propagate into nonlinear media, the nonlinear interaction under study can be influenced by effects such as pulse broadening and chirping. As a result, phenomena such as asymmetric spectrum generation can affect conversion efficiency. This can happen due to Group Velocity Mismatch (GVM) and Group Delay Dispersion (GDD), which short pulses are susceptible to. As noted in the introduction, both the phase-matching and group-velocity matching conditions are rarely satisfied simultaneously. To ensure that a mismatch between the pulses does not result in a decreased nonlinear coupling, the interaction length must be kept sufficiently short so that the pulses continue to coherently interact within the nonlinear medium, allowing them to interfere constructively [21]. The maximum crystal length can be calculated by accounting for the walk-off length. If a crystal with a length longer than that is used, the pulses will start separating, and it can be calculated by using the expression:

$$\mathrm{L_g} = \frac{\tau}{\mathrm{GVM}} \tag{3.1}$$

where τ is the pulse duration. An incorrect choice of crystal length can also cause the pulse to broaden, as different spectral components will propagate at different velocities. GDD causes this and can introduce a chirp to the pulse. To avoid these undesirable effects, the walk-off length for a BBO crystal was calculated, enabling an optimal length to be selected. The GVM was calculated using the equation:

$$\mathrm{GVM} = \left(\frac{1}{\upsilon_\mathrm{i}} - \frac{1}{\upsilon_\mathrm{p}} \right) \tag{3.2}$$

where $\upsilon_{p,i} = dk/d\omega|_{\omega_{p,i}}$, the corresponding group velocities of pump and signal/idler photons [87]. With the green pump having a pulse duration of 180 fs the GVD was calculated to be ≈ 90 fs/mm. Using those values, the interaction length equals ≈ 2 mm and therefore, a crystal with length ≤ 2 mm would be suitable to avoid the effects of GVD [87].

Choosing the crystal in which upconversion would occur was more straightforward. As suggested by [37], to maximise the eSFG response, the two crystals must be identically phase-matched, and the eSFG crystal must have a length equal to or shorter than the PDC crystal, with a shorter eSFG crystal being preferable. For our experiment, we chose to use identical crystals; therefore, another 2 mm BBO was selected instead of a shorter one. This ensured a more efficient eSFG signal.

3.2.4 Characterisation of the PDC source

After achieving perfect imaging of the down-converted state, it was essential to characterise the generated PDC power as a function of the pump beam. This would allow us to control the PDC parameters by adjusting the pump power, which is the most suitable variable for tracking the gain of the nonlinear interaction. Characterisation of the quantum radiation as a function of the pump beam power can be performed using Eq.1.16. The expression is suitable for characterising the PDC at both gain regimes, as it was derived from the quasi-stationary model described in [37, 39], which employs a fully three-dimensional description in space and time that accounts for the changes in the biphoton field in terms of the pump radiation. When the pump is at its maximum power, we produce high-gain PDC with a large number of photons in each produced mode. The number of photons per mode decreases as the pump power decreases, until we reach the low-gain regime, where one photon per mode is present. We wanted to quantify these two regimes, and therefore, the model was employed to predict the PDC response by using:

$$\mathrm{N_{SV}} = \mathrm{a}\sinh^2(\Lambda\sqrt{\mathrm{N_p}}) \tag{3.3}$$

where $a = K_m(\Lambda\sqrt{N_p})$ and K_m gives an estimation of the number of modes, and the angle inside the sinh is the parametric gain of the process as seen in the introductory chapter of this thesis. An estimate of the population of the modes is given by $\sinh^2(\Lambda\sqrt{\mathrm{N_p}})$, and hence indicates that the total number of modes that are produced changes with changing gain of the interaction. The experimental data are plotted in Fig.3.5. By matching the results of the model to the acquired experimental data, the total number of modes found in the squeezed vacuum equals $\sim 17,000$. It is important to note that the model described in [37, 39], doesn't account for GVM. Hence, a good fit of the theoretical curve to the experimental data was only achieved after adjusting the effective nonlinearity to $d_{eff} \simeq 1.65$ pm/V, only 10% different from the theoretical value found in [88]. The effective nonlinearity coefficient d_{eff} is included in the expression of Λ in Equation 2.2.2. With the rest of the coefficients in Equation 2.2.2 being either universal constants or experimentally determinable, d_{eff}, which depends on crystal structure and material properties, was the only other constant that could be adjusted to match the model to the experimental data, and hence it is the one we adjust.

The pump data in Figure 3.5 were measured using a thermal detector (Gentec UP19K-50L-H5-D0) while the PDC was measured using Ge photodiode (Thorlabs s132c). In the same Figure, the linear expansion of Eq. 3.3 is also plotted in dashed purple lines. As noted in the introductory chapter of the thesis, in the low-gain regime, PDC output scales linearly with the pump power. Therefore, a linear approximation is valid for cal-

culating the pump powers at which the spontaneous emission regime commences. From the linear approximation, the PDC crystal needs to be pumped with $\leq$ 6 W of pump power, which is equivalent to $\sim$ 2 nW of SPDC power. A similar characterisation to that mentioned in this section was also performed at 500 kHz.

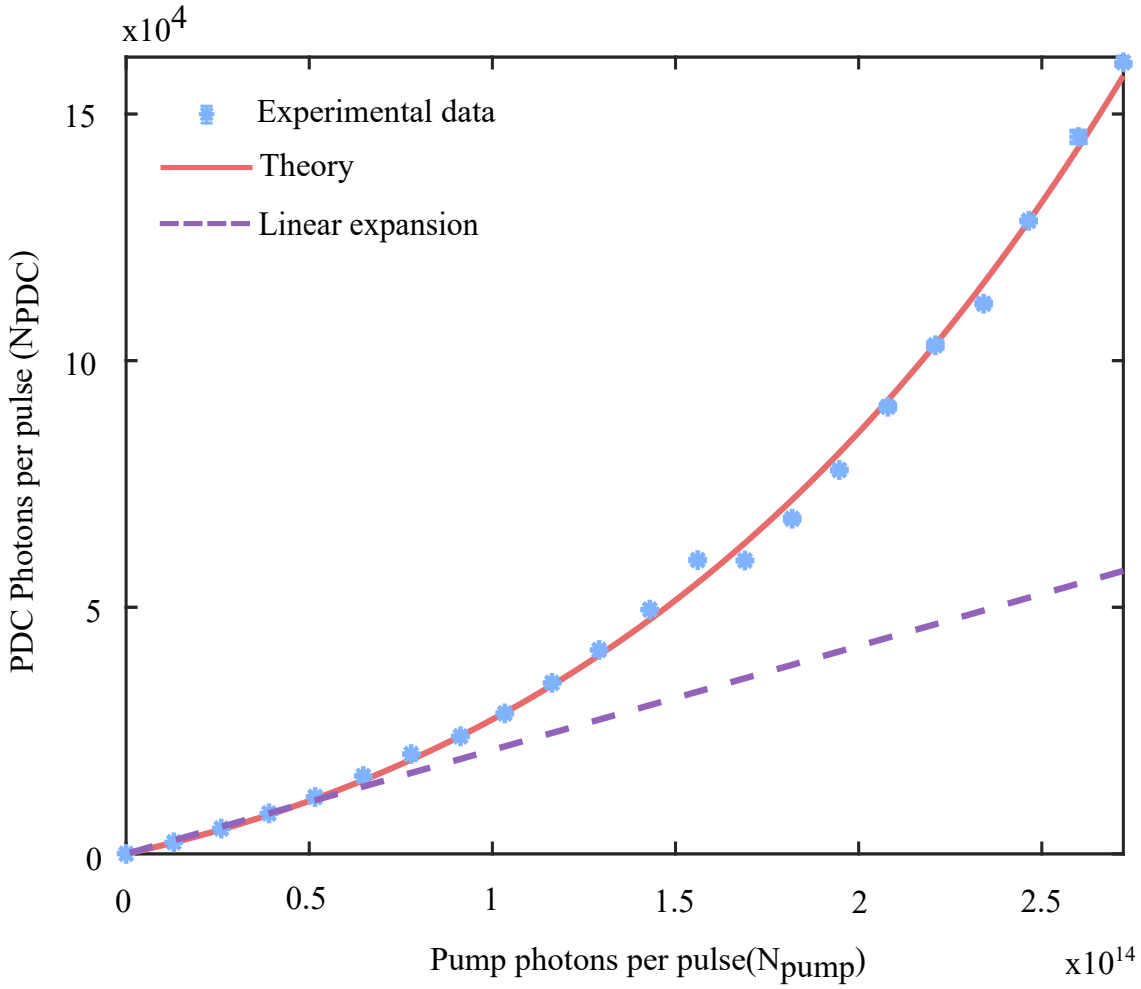

Figure 3.5: **PDC photons per pulse as a function of the pump.** The theoretical model predicts well the PDC response when we account for GVM by adjusting d_{eff}.

Throughout the experiments presented in this thesis, Eq. 3.3 was used to estimate the photon number in each mode. However, a second, more intuitive method can also be used to calculate the number of modes present in the PDC state. Because modes are the areas in space and time where entangled photons are confined, the number of modes can be directly associated with the entanglement area and time. More specifically, the number of spatial modes will be proportional to the pump beam's spatial profile over the entanglement area where the photon pairs can interact. A similar argument holds for the temporal modes. In the next section, after the entanglement volume is calculated, I will present the second method for calculating the number of modes in the PDC state.

3.2.5 Entanglement Area and Time

The area in space and time that the photons in the entangled pair can interact with each other determines the entanglement volume of the PDC. It is set by phase matching, pump, and crystal properties. In the case of entangled two-photon absorption, the first-order coefficient is equal to:

$$\sigma_{\mathrm{e}} = \frac{\delta_{\mathrm{r}}}{2\mathrm{A_e}\mathrm{T_e}} \tag{3.4}$$

where δ_r the classical absorption coefficient, A_e and T_e are the entanglement area and time, respectively. Tailoring these properties is essential to maximise the expected enhancement in entangled two-photon interactions, with smaller values of the netanglement area and time leading to a larger entangled two-photon absorption coefficient and, hence, an increased fluorescence rate in eTPA. Therefore, entanglement area and time are usually small, on the order of a few micrometres and femtoseconds, respectively. Here, we have analysed the angular and temporal bandwidths of the PDC state to calculate the entanglement volume.

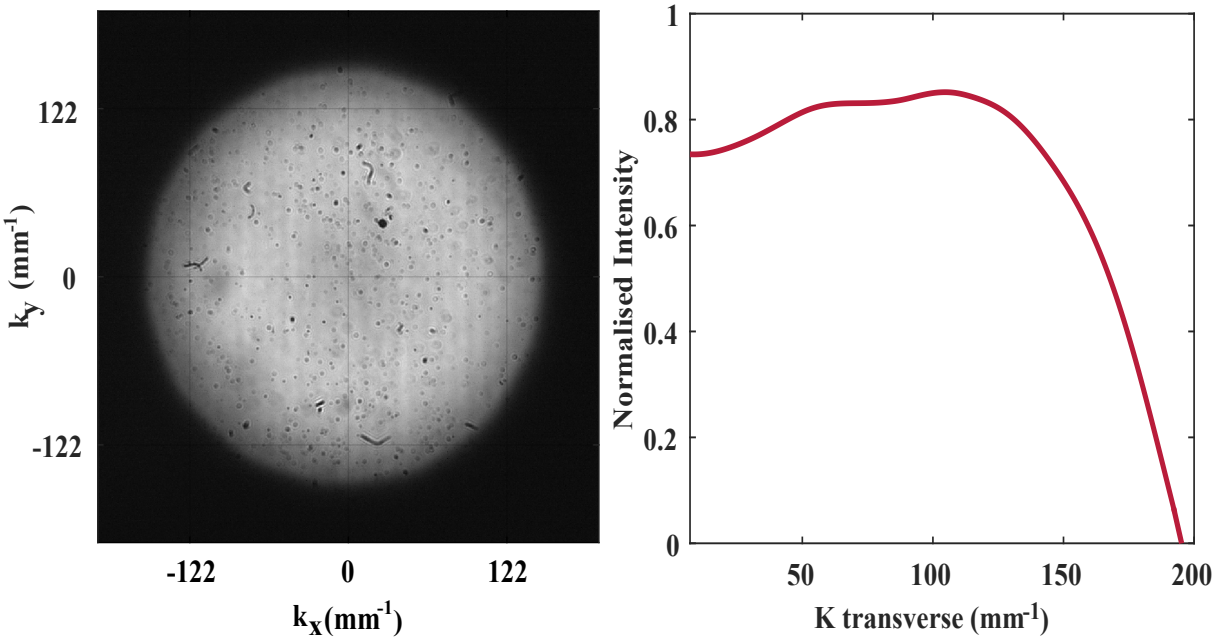

Figure 3.6: **K transverse of the PDC.** The picture on the left shows the angular spectrum of the SV, and the picture on the right shows the intensity across the profile of the PDC, indicating the phase matching condition for the eSFG experiment.

In the transverse plane, the idler photon is emitted within some polar and azimuthal angles about the pump propagation direction, with the entanglement area being related to the uncertainty of locating the idler photon when the location of the signal is known.

As explained in the introduction, the entanglement area A_e is affected by the pump beam waist. It is also set by the chosen phase-matching of the interaction, which is in turn affected by the different group velocities of the signal and idler, as well as the second-order dispersion they experience [89]. Therefore, determining the phase-matching of the SV is the first step in measuring the entanglement area. To this end, a far-field PDC size measurement can be performed to indicate the transverse-momentum wavevector. This correlates to a near-field measurement of the position, its conjugate variable. This measurement was performed by placing a narrowband filter at the PDC's far field to reduce uncertainties in $k_\perp$ across different frequencies. For the same reason, a camera with a more constant response around 1030nm than the Zyla was used. The camera was SWIR Atlas from Lucid Vision Labs with a Sony IMX990 InGaAs sensor with a sensor size of 1/2", and therefore, the PDC far field was re-imaged to fit the area of the sensor. An intensity profile analysis was performed along the diameter of the far field of the PDC, and to access the transverse wavevector space from the real-space intensity profile, a Fourier transform was performed using the equation:

$$\mathrm{k}_\perp = \frac{2\pi}{\lambda}\sin(\theta) \tag{3.5}$$

where angle θ can be mapped to real space using $\theta = \tan^{-1}(x/f)$, with x the far field diameter and f the focal length of the imaging system. The image taken was replotted in momentum space as shown in Figure 3.6. Hence, we can approximate the SV angular spectrum to be $\simeq$ 150 mm^{-1} (Half Width at Half Maximum (HWHM)), corresponding to $\simeq$ 25 mrad. Now, the length scale over which the photon pairs are entangled can be found from Heisenberg's uncertainty principle as $\Delta x \sim 1/\Delta k$, which will result in an entanglement length of $\sim$11 µm.

Similarly, the entanglement time defines a length scale over which the two-photon state must have been emitted and depends on the frequency uncertainty of the photon pairs. While our PDC photons span a broad frequency range, we use a band-pass filter to remove any spectrum that would be affected by GDD. Therefore, the entanglement time T_e will be inversely proportional to the filter's bandwidth. The filter used was a Semrock FF01-1055/70-25 with a 70 nm (FWHM) bandwidth centred around the wavelength of 1055 nm. As explained previously, by placing the filter at an angle of 23° the spectrum was cut symmetrically around 1030 nm. With the entanglement time being the inverse of the uncertainty in the angular frequency, $T_e = 1/\Delta\omega$ and the entanglement time was calculated equal to $\sim$ 45 fs (FWHM). With space and time being intrinsically linked, we can define a volume in which the photon pairs generated by PDC are confined. We have assumed that the volume is simply a cylinder with radius A_e and length T_e so that $V_{ent} = \pi A_e^2 T_e$.

As discussed earlier, the number of modes can be calculated from the values of entanglement area and time. In simple terms, the number of modes in the state is the ratio between the spatiotemporal volume of the downconverter state to that of the pump. The pump will generate photon pairs across its profile, each pair existing in those modes. The spatiotemporal volume we have calculated gives an estimation of the size of the mode. Therefore, the amount of spatiotemporal volumes we can fit into the pump spatiotemporal profile indicates the number of modes produced. Using this method we get $K_m = (185\text{fs}/45\text{fs}) \times (1.5\mu\text{m}/22\mu\text{m})^2 \simeq 19{,}100$ modes. This number is ∼12 % different from the previously calculated value, and if we take into consideration the different approaches of these two methods, the discrepancies between these two values are not a big concern. It is essential to note that, for the method presented in this section, the SV pulse profile was assumed to match that of the PDC pump. This assumption is strictly valid only at low parametric gain, when the near field profile of the SV reaches the same value as that of the pump, as explained in [37, 55]. For this reason, during our investigations, the first method was preferred as a way of determining the number of modes, which also allowed as to calculate the number of photons in each mode at varying gain of the PDC interaction.

3.2.6 PDC Spectrum

Although the entangled photons are filtered through a band-pass filter, the PDC spectrum was measured to confirm that the photon pairs generated are centred mostly around 1030 nm, with no significant asymmetries. To this end, the PDC near-field was reimaged into a Czerny-Turner spectrometer (Andor Shamrock 163) with interchangeable gratings. For our purposes, we used a reflective blazed grating, SR1-GRT-0600-1200, offering a 0.13 nm resolution. The ATLAS SWIR camera was attached to the spectrograph's output. Firstly, the zeroth order was aligned on the camera, and then the grating angle was adjusted until the first order was visible on the camera sensor. The spectrum was dispersed over a dimension much larger than the camera's sensor, meaning that the entire spectrum could not be imaged. To solve this, the camera was placed on a translation stage to capture images of the entire spectrum as it moved along the direction of dispersion. Given the 1/2" size of the camera sensor, five images were required to cover the full extent of the dispersed spectrum, which meant that it spanned approximately 6 cm. These images were processed and "stitched" together to form the entire spectrum. Since the camera can only measure intensity at each pixel, a calibration was performed to ensure that specific pixels correspond to specific wavelength values. This was done using spectral filters with examples shown in Fig.3.7. At the limit of each filter's bandwidth, a sharp edge appears in the spectral image, marking a specific wavelength associated with that pixel. In total,

seven infrared filters were used with bandwidths spanning from 950 nm to 1200 nm. The acquired spectrum is shown in Fig.3.7 C.

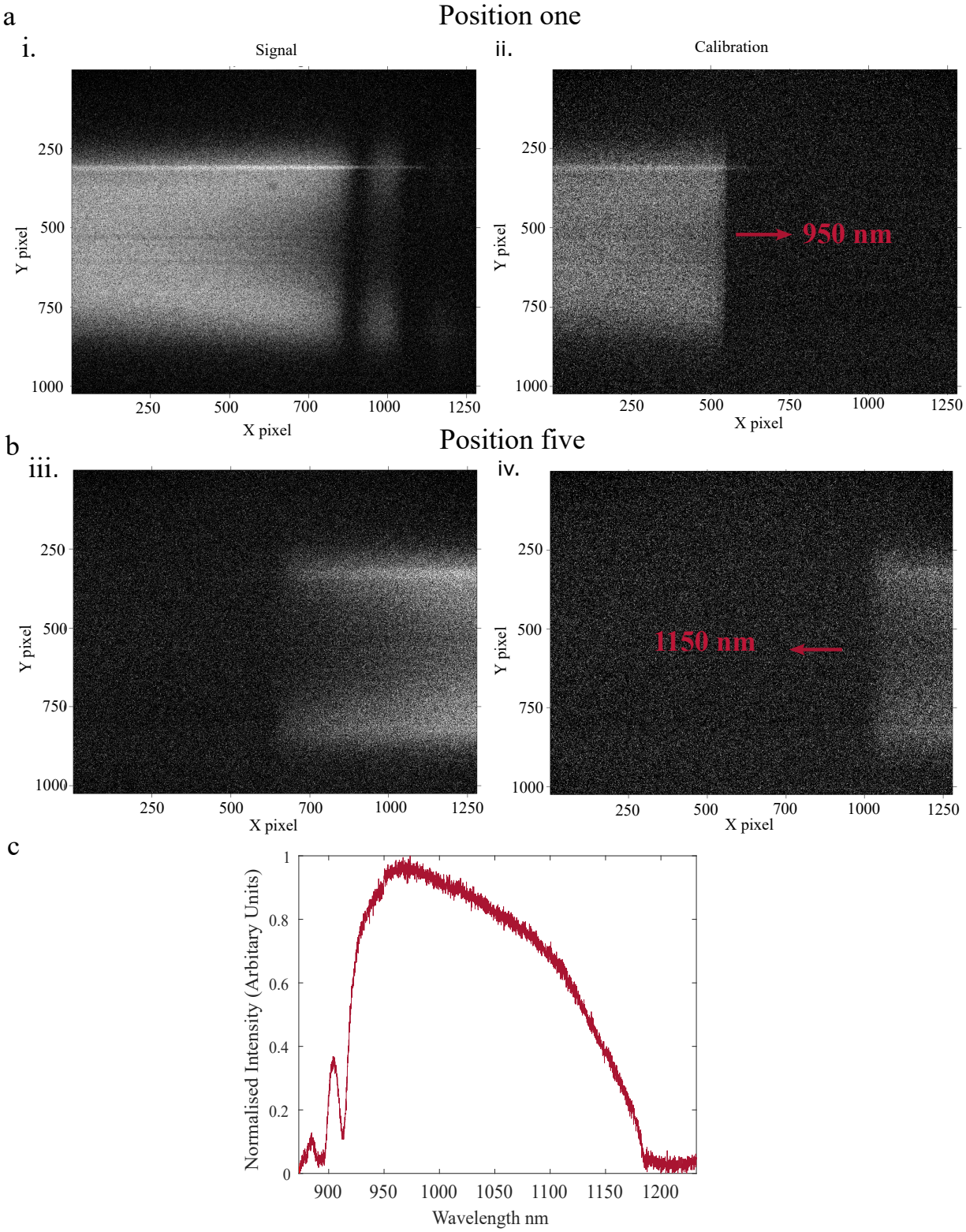

Figure 3.7: **Spectrum of PDC**. Panels **a** and **b** show examples of the pixel-wavelength calibration performed to acquire the spectrum of the PDC. The acquired wavelength spectrum of the PDC is shown in **c**.

As can be seen from Fig.3.7 C, on the left-hand side of the spectrum, for wavelengths closer to the pump's wavelength, an irregularity in intensity is observed. This can be attributed to the mirrors' coating response at lower wavelengths. But most importantly, we note an asymmetry in the spectrum about the degenerate wavelength of 1030 nm. This asymmetry, as well as the lower intensities at longer wavelengths, has been observed before by [90, 91], where they claim that this asymmetry should be present when the PDC spectrum is taken in terms of $S(\lambda, \theta)$, which is true for their experiments. They capture the spectrum by selecting portions of the PDC far field. Hence, their wavelength has a certain angular dependence. It is suggested in [90] that this asymmetry can be adjusted by multiplying the spectra by λ^4, a factor stemming from the fact that they select certain modes in the far-field. We have measured the spectrum in the near-field of the PDC, and we cannot perform such a correction as an angular aperture does not limit our measurement. This observed asymmetry is always present when the PDC's wavelength-angular spectrum is acquired. In contrast, when the wavevector-frequency spectrum is measured, such asymmetry will be absent. This can be explained by considering the phase-matching Eq.2.3, which suggests that the same number of photons will be generated at each side of the degeneracy. However, the energy conservation law doesn't imply that the same amount of photons will be generated at those wavelengths. Such asymmetry is expected to be absent when the spectrum is measured in frequency space. Therefore, to translate between the two spectra, an energy-conservation factor should be considered.

Consequently, to study the range of frequencies in which the PDC spectrum expands, a normalisation needs to be performed so that the power spectral density is plotted in its natural variables, where symmetry is expected. Hence, a normalisation needs to be performed so that the equality below holds:

$$\int \mathrm{S}(\lambda)\mathrm{d}\lambda = \int \mathrm{S}(\omega)\mathrm{d}(\omega) \tag{3.6}$$

We start solving the above by using the relationship $\omega = 2\pi c/\lambda$, and remembering to change the variables to $d\omega$ of the integral on the left-hand side of the above equation. we deduced that to obtain the frequency spectrum, we need to multiply the wavelength spectrum by a factor:

$$\mathrm{S}(\omega) = \frac{2\pi \mathrm{c}}{\omega^2}|\mathrm{S}(\lambda)| \tag{3.7}$$

ensuring that the change between wavelength and frequency will conserve energy.

The frequency-resolved power spectral density was plotted in Fig.3.8. The frequency data in the plot have been normalised around the central frequency of 1.8×10^{14} rad Hz, which equates to 1030 nm in wavelength space. From the figure, it can be seen that

the spectrum is asymmetric far from the degenerate wavelength of 1030 nm, indicating the need to filter the squeezed vacuum using bandpass filters. This was done to ensure that any interaction at the SFG crystal occurs between photons that can be temporally overlapped, minimising the generation of incoherent SFG. The filtered, squeezed vacuum spectrum is plotted in pink on the same graph. The spectrum was not measured with the filter in place; hence, the data shown here are extrapolated from the manufacturer's data on the filter's response.

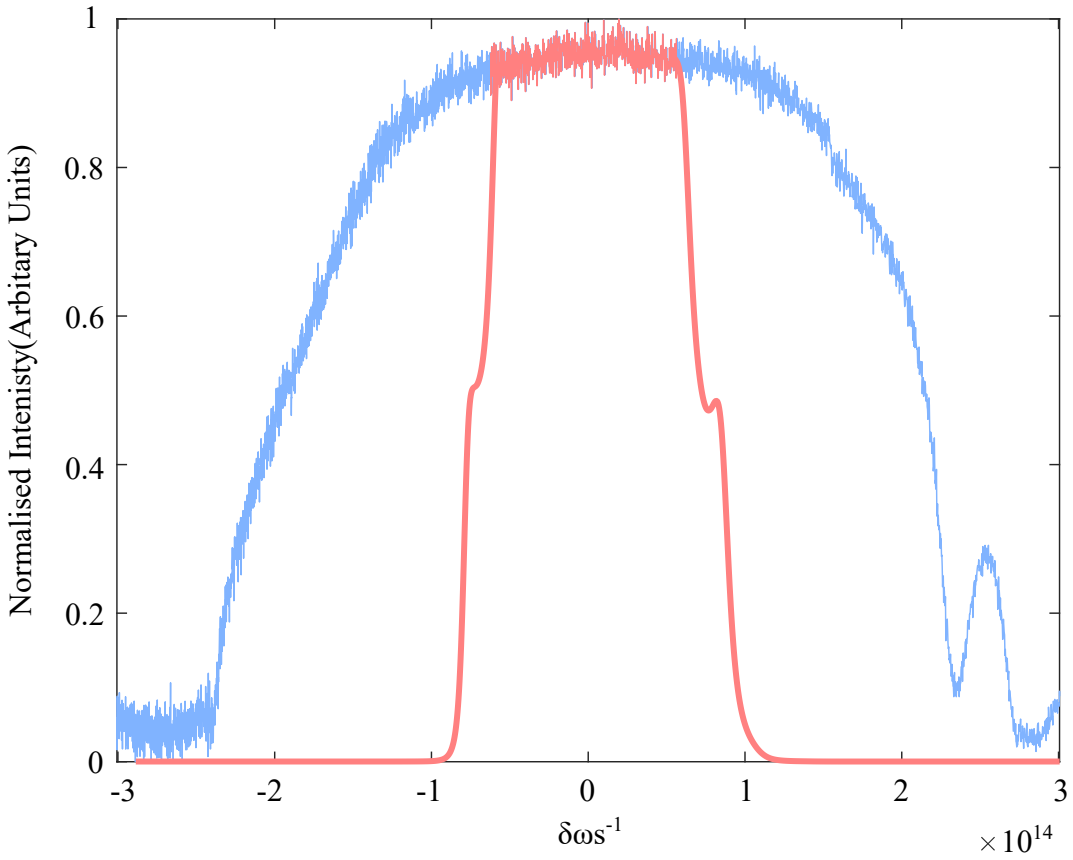

Figure 3.8: **Frequency spectra of PDC** centred around 1030 nm. The blue line represents the unfiltered frequency spectrum of the PDC, while the pink line corresponds to the extrapolated data from the 70 nm bandpass filter response. From the above, we note that the spectrum beyond the filter's bandwidth soon becomes asymmetric, with photons from that part of the spectrum being unable to undergo coherent interaction in the SFG crystal.

It is important to note that a shrinking of the spectrum's width has been reported in [90] as the gain of the nonlinear interaction is reduced. While we do not study here what happens at the spectrum at different gains, this result is not surprising. Similar effects were investigated in this thesis as well, and more details will be provided later in the Chapter.

3.2.7 Methods

A PMT was used to measure the eSFG signal, as it can be operated as a low-noise single-photon detector. A PMT consists of a light-sensitive photocathode that produces electrons when it interacts with light. The produced electrons are collected by a dynode, which will then generate secondary electrons, resulting in a multiplication effect. Finally, the electrons are collected by an anode, which generates an output current. The PMT used to measure the SFG signal was H7422-40, with a 40% efficiency around 515 nm and a dark count rate of 100 s^{-1}. The voltage driving the PMT was set at a maximum of ∼2 Volts to increase its sensitivity for all measurements. The PMT was connected to time-tagging electronics, specifically the HydraHarp 400, which can produce Time-tagged Time-resolved (TTTR) data. This enabled us to reject most of the background radiation and reduce the dark count rate, as a timing reference was used. This was achieved by sending an excitation pulse from the laser to the Hydraharp and synchronising the arrival of the SFG signal on the PMT with the laser pulse. The laser sync and the eSFG photons are converted into NIM-type electrical signals, and Hydraharp then registers photon-counting events and builds a histogram for each time bin. It was ensured that, for each time bin, the probability of a photon event occurring was less than 1, thereby avoiding the pile-up effect [92]. This meant that when operating at full power, the signal reaching the PMT should be less than 10,000, i.e., <5% of the laser's repetition rate.

All measurements were automated using a MATLAB script to further reduce background light. Matlab was used to acquire data from Hydraharp. Two rotational stages were also used, with their operation automated in MATLAB. One of the stages was used to rotate the half-wave plate in front of a thin film on the pump beam line to control the power of the PDC. The second one was used to rotate the eSFG crystal 90°, so that no phase-matching could occur, and any counts arriving at the detector were just background radiation. Before each measurement, a characterisation of the PDC power as a function of the half-wave plate was performed and the data were fitted using the equation:

$$\mathrm{P_{PDC}} = \mathrm{asinh}^2(\sqrt{\cos^2(2\theta)}) \tag{3.8}$$

as shown in Figure 3.9. The above is just a modified version of Eq.2.15 and suggests that the power of the PDC and, hence, the pump power, changes as a function of the half-wave plate, which has a $\cos^2(2\theta)$ response. The fit parameters were then inserted into the MATLAB script, and the angles for the half-wave plate to be rotated could be chosen, each corresponding to a PDC power value. For this, the PDC power was measured using a Thorlabs S132C Germanium photodiode at the surface of the second crystal. The optical power range of the photodiode is limited to ∼5 nW, so a different detector was required to

measure the power of the PDC at the low gain regime. For this purpose, a Femtoreceiver with an InGaAs PIN photodiode was used. The PDC was refocused to a size suitable for the Femtoreceiver's active area, and the signal output voltage was measured with an oscilloscope. The Femtoreceiver was characterised using a Ge photodiode to retrieve the PDC power.

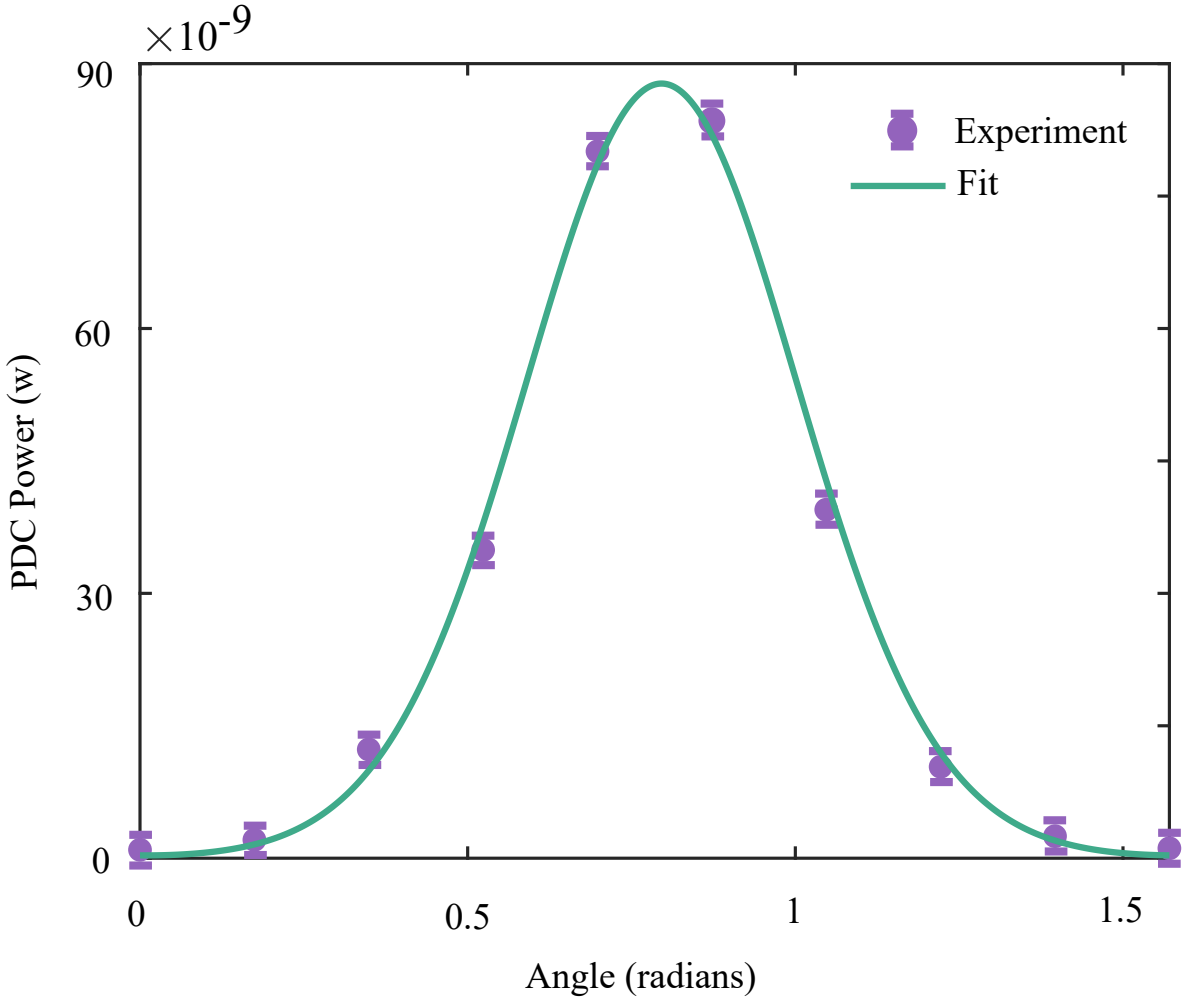

Figure 3.9: **Calibration between PDC power and half-wave plate angle controlling the pump power.** A calibration like the one shown here was performed before each measurement, and the fit parameters were fed to the MATLAB script controlling the optomechanics and the HydraHarp.

The data files from the scans were saved in .DAT format. From the data, the signal was extracted, and the background counts as well as the noise floor were subtracted from the signal. The signal was then normalised by the timing resolution of 1024 ps, the repetition rate and the exposure time. Lastly, the data were corrected for the detector's efficiency.

3.3 Results

To confirm the presence of a quantum advantage, the first measurement was performed at the low gain of the PDC, when one or fewer photons are present in each mode. Therefore, the only possible recombination that can occur at the second crystal during the upconversion process is from the entangled pair in each mode. A power scan was performed in which the PDC power was reduced, and the eSFG counts were recorded. This measurement was done at 500 kHz for several reasons. At the repetition rate of 500 kHz, the scaling of the PDC to the pump remains linear for most of the range of the pump power, making it easier to access the single photon per mode regime while making the scattering of the green pump less bright, since less SFG is produced from the reduced pulse energies. Secondly, at 500 kHz, each pulse arrives faster, allowing shorter measurements of the eSFG signal.

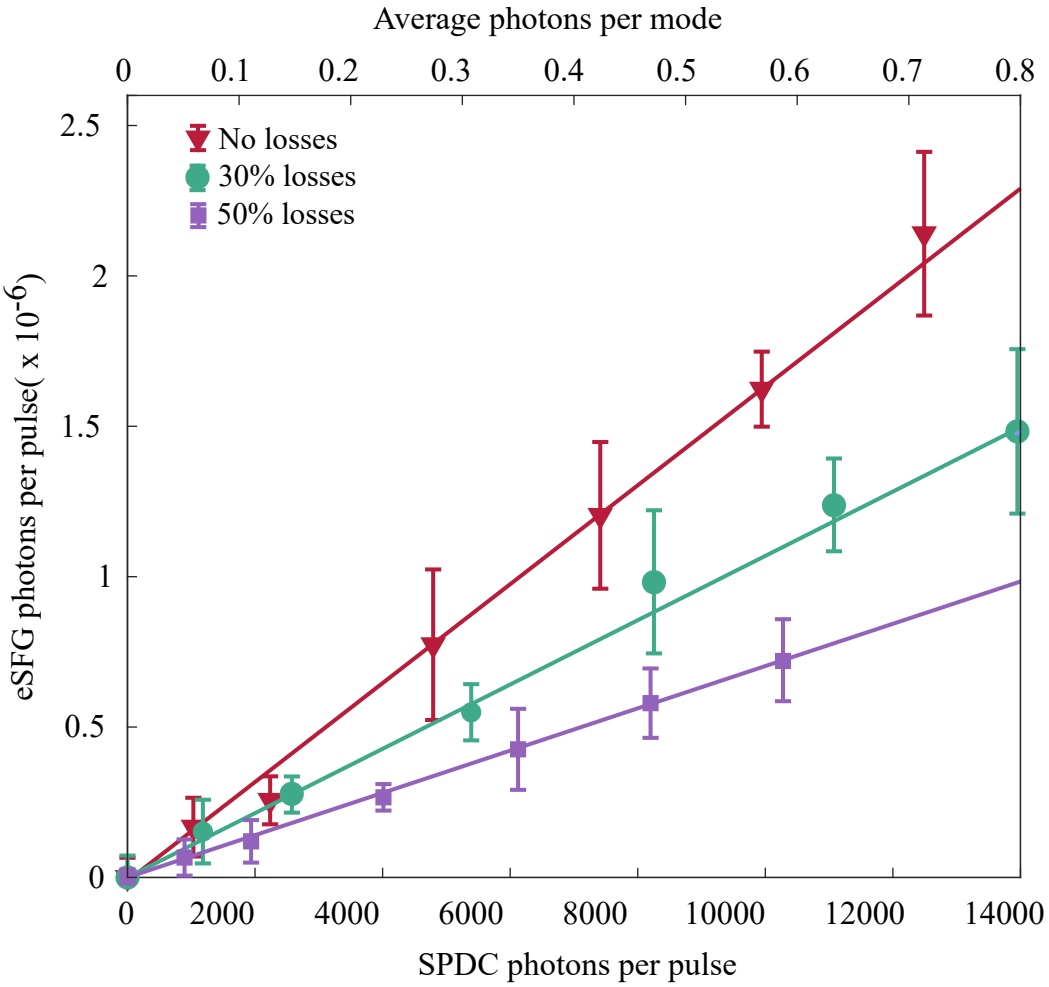

Figure 3.10: **Measurement of the SHG efficiency at the low gain regime.** Each data point is an average over a 5-minute acquisition at 500 kHz. The efficiency for the no losses cases (red line) is $\eta = (3.3 \pm 0.2)\text{x}10^{-10}$, $\eta_{30\%} = (2.2 \pm 0.1)\times10^{-7}$ for the 30% losses (green line) and $\eta_{50\%} = (1.3 \pm 0.1)\times10^{-7}$ for 50% losses (purple line).

The first results shown in Figure 3.10 confirm the expected linear scaling of the eSFG as a function of the incident PDC on the nonlinear crystal. The data were fitted using a first-degree polynomial (y = ax), plotted in red, with a coefficient equal to 7.755x10^{-7}. The efficiency of the process can be calculated using $\eta = 2N_{eSHG}/N_{PDC}$, where the factor 2 indicates the interaction of two PDC photons with half the energy of the generated photons. Therefore, the produced eSFG efficiency equals $\eta = (3.3 \pm 0.2)$x10^{-10}. We aimed to investigate the impact of losses on the SFG efficiency. Losses were added to the entangled state to ensure that the linear scaling is indeed a contribution of the correlations present in the photon pairs. The losses added were in the form of Neutral Density (ND) filters of different transmissions, resulting in the loss of PDC photons and, hence, a reduction in the amount of PDC photons that undergo eSFG. For example, for an ND filter with 50% transmission, half of the photons in the state remained, while the rest were lost randomly, meaning there was no control over which photons would not get transmitted. For a state with a 50% transmission, there is a chance that most of the lost photons are either all signal or all idler ones (although this example is nonphysical), or a stronger chance that half of the photons lost are idler with the rest being signal photons, and vice versa. We wanted to isolate the effects of these losses on the efficiency of eSFG. To this end, the power of the squeezed vacuum was increased to match the power of the squeezed vacuum that undergoes eSFG when no intentional losses are present, which at the low gain was ∼5 nW or ∼13000 photons per pulse, as shown in red on Figure 3.10. Two loss measurements were performed using ND 0.1 and ND 0.2, respectively. For both measurements, the PDC power was increased to match the available PDC power without losses by adjusting the green pump power. The filters' transmissions were characterised, and for ND 0.1 and ND 0.2, they were 30% and 50%, respectively. Then, a similar measurement to the lossless case was performed, in which the eSFG counts were recorded as the PDC power was reduced. We observed another linear scaling for both ND filters, with the corresponding first-order polynomial fits presented in Figure 3.10 in green and purple, respectively. The first-order coefficients obtained from fitting the data for transmission 30% and 50% are 5.612x10^{-7} and 2.818x10^{-7}, respectively. It is observed that the ratios between the two coefficients obtained from the loss cases and the coefficient from the no-loss case are 0.70 and 0.40, respectively, and each value agrees with the corresponding ND filter's transmission.

When losses are present, the PDC radiation exhibits characteristics similar to those of a thermal light source; it is a mixed state with low coherence. This is true for all loss cases, although the squeezed vacuum state has the same amount of photons present as in the case where no intentional losses are present. Any eSFG production is only possible by photon pairs that haven't been affected by losses. In other words, there is a negligible probability for any single photon to be able to upconvert with any photon apart from its entangled partner, since at this regime we are still photon-starved. Therefore, we observe

only a reduction in eSFG production efficiency, with linear scaling maintained. However, this wouldn't be the case if the losses were exceptionally high. Our loss measurement differs from those performed in the literature thus far, as previous research didn't account for the PDC photons lost when ND filters were introduced to the state. In previous studies, the power of the PDC was attenuated using the ND filters [63, 93]. In those cases, when a signal or idler photon is lost, it is equivalent to the loss of the entire pair, and therefore, a quadratic scaling was observed. To compare the results with the current available literature, we plotted in Figure 3.11 the eSFG response if losses were added for a fixed PDC gain. This was done by extracting the expected eSFG response from the measured transmission of the ND filters introduced at the far field of the PDC. Although this indicates that the two loss measurements are related, our proposed method is more effective at determining whether a quantum advantage is indeed present, since both loss and loss-free states contain the same number of photons. We only assumed that when losses are present, we have a mixed state with both entangled and non-entangled components. We wanted to see what happens at higher gain, so we studied this next.

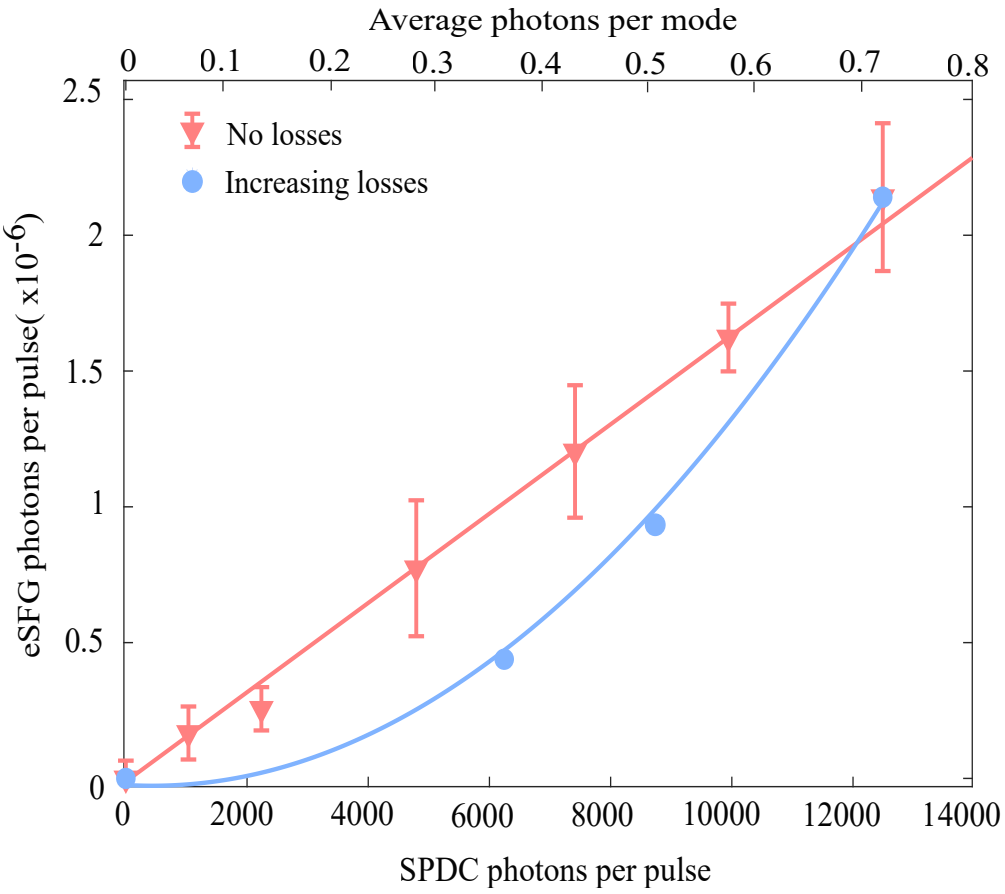

Figure 3.11: **Expected eSFG response for increasing losses.** The blue line is the expected response that the ND filters would have caused to the effect if the number of photons per pulse reaching the SFG crystal were not corrected for each ND filter introduced.

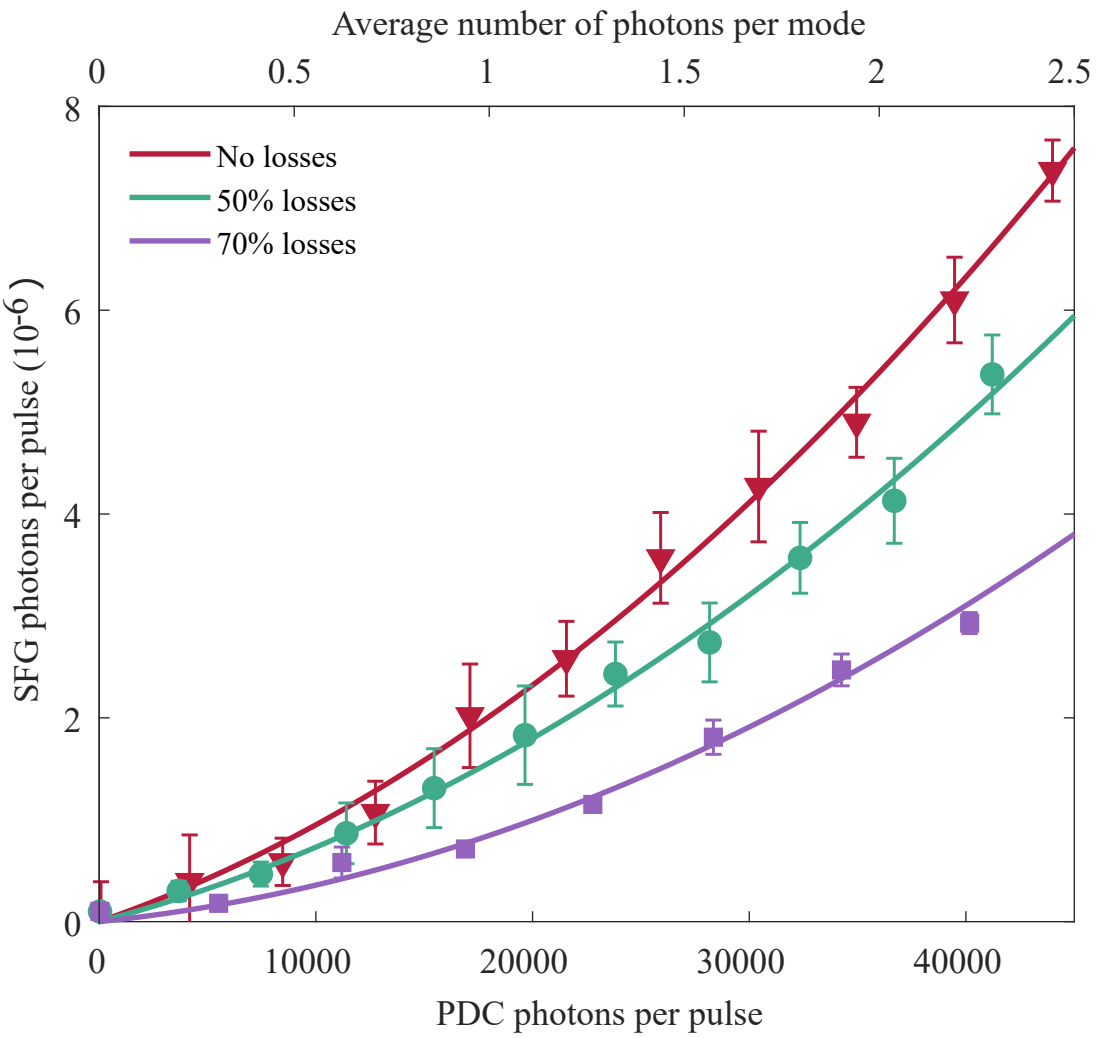

Figure 3.12: **Efficiency of SFG with losses at a higher gain of PDC.** In this regime, the interaction between high-order photon pairs becomes relevant. Therefore, the data were fitted with second-order polynomial equations.

For the stimulated regime of PDC, ND filters with lower transmission were selected to make the effect of the losses more evident. Now, due to the large number of photons present in the state, photons that are not entangled with each other may interact. The arrival of these photons introduces a second-order term in the SFG scaling. As mentioned earlier, this incoherent component was blocked at the SFG's far field, and we do not expect to measure it in the results presented here. Instead, at this "mid-gain" of the PDC, the generation of higher-order photon pairs occurs, and their interaction in the SFG crystal will lead to a second-order term, different from the one mentioned for the incoherent SFG. Therefore, the data presented in Figure 3.12 are fitted with a polynomial with both a linear and a quadratic term ($y = ax + bx^2$). As in the low-gain regime, we observe a reduction in the eSFG efficiency. From the fits, we observed that the linear term decreases as the quadratic term increases, leading to greater losses. This suggests that as losses increase, the entanglement component of the state decreases, as more uncorrelated photon pairs

interact to produce SFG. From this, it is evident that a more lossy state will eventually cross over into a purely quantum state.

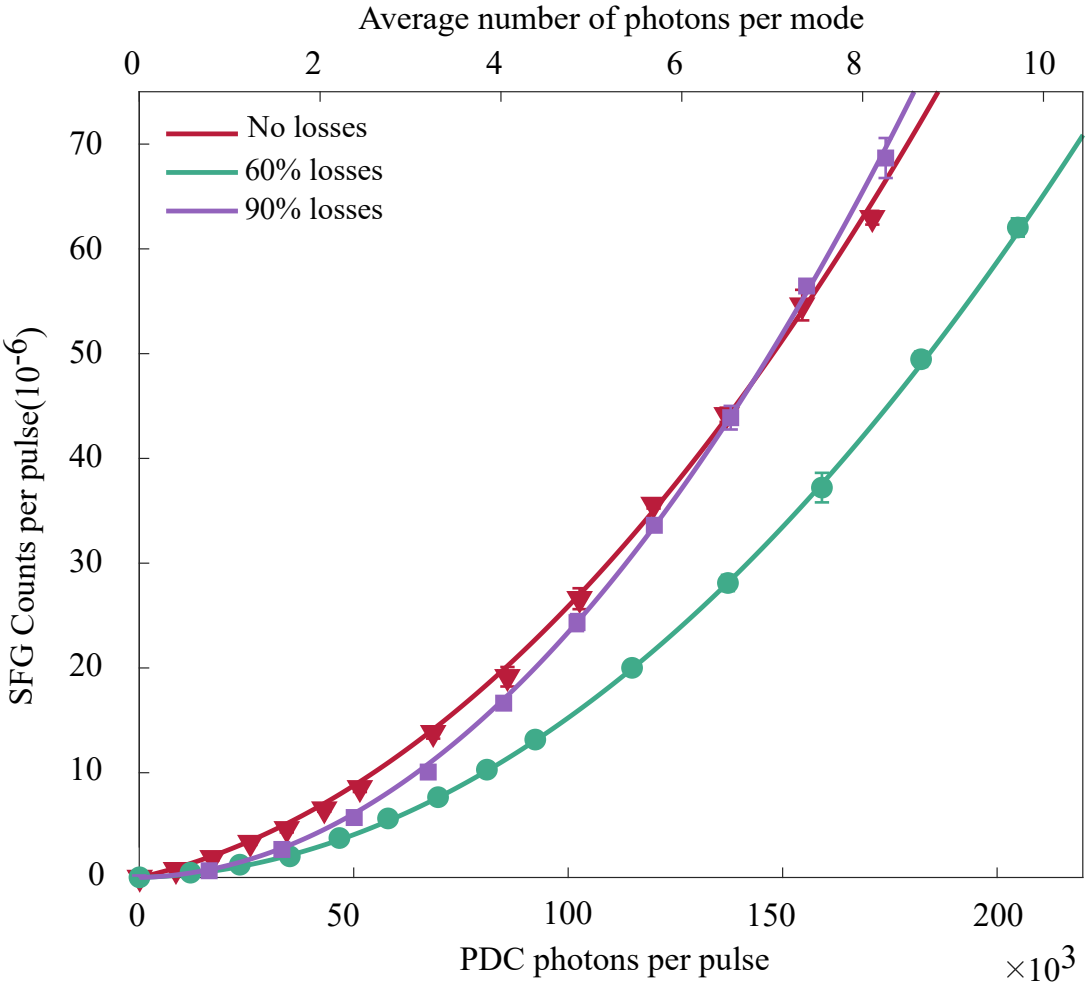

Figure 3.13: **A more lossy state produced more photons than a pure quantum state.** When the state is composed of photons which can't interact with their entangled pair, the SFG produced will have a classical component contributing to its efficiency scaling.

To examine this, measurements were performed at 200 kHz, as the pump pulse energy was sufficient to probe the SFG effect with the PDC at the high gain. However, the measurement needed to be performed in a regime where we would still have sufficient pump power to match the powers of the lossy state to those of the lossless one. The regime in which this was possible was when the state had ∼10 photons per mode. In the case where 90% losses are present, we indeed observe more stimulation of eSFG for the same flux of photons at the eSFG crystal as the zero losses case. A macroscopic model was formulated to describe this phenomenon, using equations for eTPA. We start by considering the equations describing the enhanced rate of eTPA:

$$R_{eSFG} = \delta R_e + \sigma R_e^2 \tag{3.9}$$

With δ and σ the coefficients of first and second order absorption, and as explained previously, the first order term is the contribution of the entangled photons interacting together in the second crystal, while the second order term appears due to the entanglement conservation at the high-gain of the PDC. Both those components contribute to the reconstruction of the pump. When losses are added, and the photon fluxes are matched, we have introduced photons to the state that have entirely lost their entangled partner. Now, there are only three possible interactions these photons can have: they don't interact with any photon, they interact with a photon that has also lost its entangled partner, or with one of the photons that still has its entangled pairs present. In all these cases, the photon gives the state characteristics similar to a thermal source, and hence any contribution from them will be classical. Therefore, a third term arises, and the equation becomes:

$$\mathrm{R_{losses}} = \delta \mathrm{R_e} + \sigma \mathrm{R_e^2} + \sigma \mathrm{R_c^2} \tag{3.10}$$

to describe a mixed state with entangled and non-entangled parts. In expressing the above equation, we have assumed that the classical SFG and SFG generated by the photons produced at the high gain of the PDC have the same absorption coefficient σ. When no losses are present, we assume maximum photon transmission, T, and attribute it to the entangled SFG. The rest of the photons that are present contribute to a reduced transmission, 1-T, and therefore the entangled photon rate and the non-entangled photon rate can be expressed as:

$$\mathrm{R_e} = \mathrm{T} \times \mathrm{R} \tag{3.11}$$

$$\mathrm{R_c} = (1 - \mathrm{T}) \times \mathrm{R} \tag{3.12}$$

correspondingly. The eSFG rate equation can then be written as:

$$\mathrm{R_{losses}} = \delta \mathrm{TR} + \sigma \mathrm{R}^2 (2\mathrm{T}^2 - 2\mathrm{T} + 1) \tag{3.13}$$

If transmission T is maximum (T=1), we revert to Eq.3.9. At the other end, as T approaches zero, we observe eSFG scaling as it would classically; however, in our case, zero transmission has no physical meaning due to how we account for losses. The above equation was plotted for T = 1, T = 0.5, and T = 0, where T = 0 corresponds to completely uncorrelated photons; hence, we expect a completely classical scaling from it.

From Figure 3.14, it is evident that classical radiation (purple line) will eventually generate at a higher rate than the SFG produced by a lossy PDC state, but will converge at infinity to the case where we have T = 1, concluding that there is a real advantage when pumping the system with an entangled beam of light. We observe that the classical SFG will cross the eSFG generated from a PDC state with losses present (orange and

green lines), indicating that the real challenge lies in generating entangled photons and transmitting them without losses to achieve the maximum efficiency of the effect. Although we assumed T=1 for data without intentional losses, in reality, our experiment still incurred unavoidable losses beyond our control. Lastly, we observe that lossy states (orange and green lines) will eventually cross, with the more lossy one (green) generating at a higher rate. This was observed experimentally, with the results shown in Figure 3.13. This result was initially surprising, but further investigation, as discussed in the next section, can explain the effect. Briefly, we observed a change in the PDC peak intensity at different parametric gains, with higher parametric gain increasing the eSHG efficiency. It is essential to note that the crossing points can be predicted using the theoretical model formulated in [37].

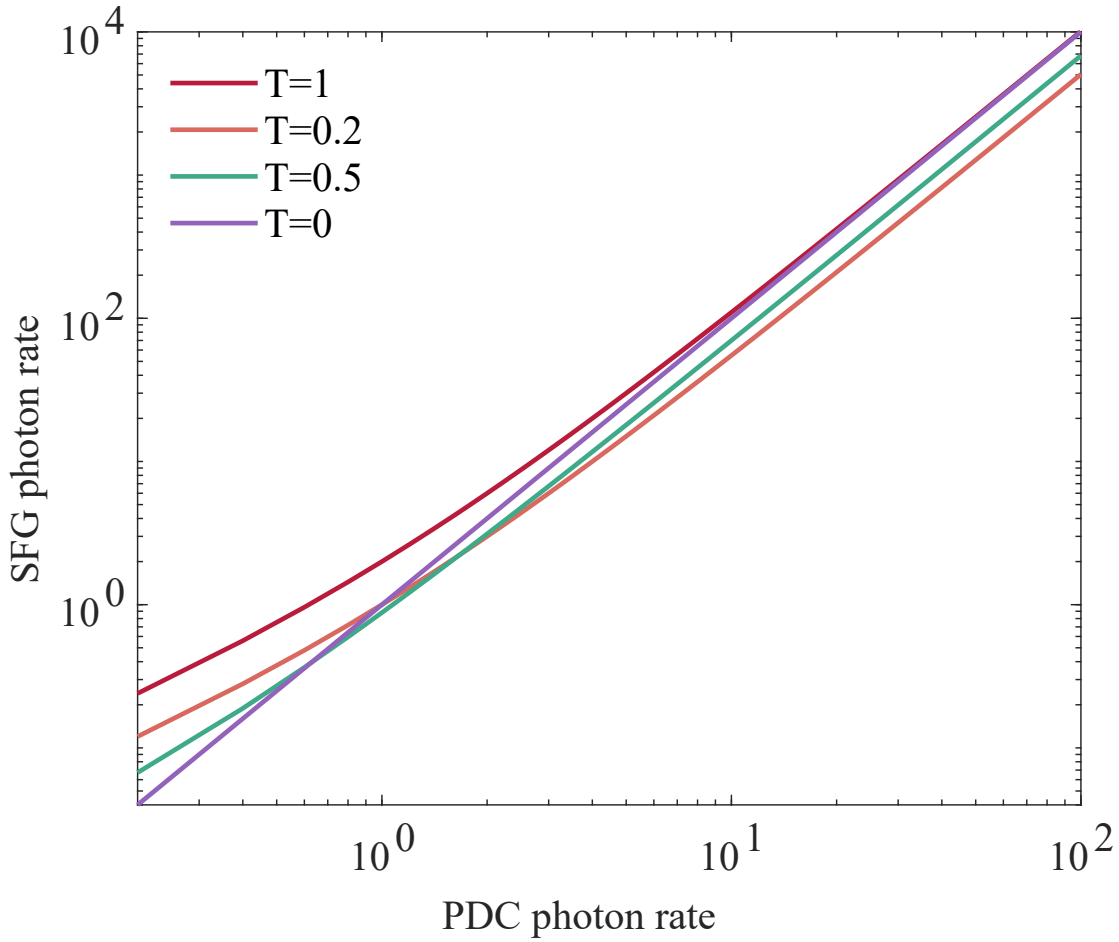

Figure 3.14: **Theoretical curves of transmission equation.** In red line, the transmission of eSFG produced by a state of entangled photons without any losses. SFG produced by classical laser radiation (in purple) will only asymptotically reach the red line. However, if any losses are present in the PDC state (green and orange lines), the classical produced SFG will produce more photons.

Another interesting observation arises from the data fitting. The data in Figure 3.13

were fitted using a second-order polynomial. However, the model described by Eq.3.13 was able to predict the existence of crossing points; therefore, the data were also fitted using Eq.3.13. We note that the transmission coefficient T was set equal to the measured transmission of the ND filters. Hence, the values of the coefficients δ and σ differ across loss cases, as we observed previously when fitting the data with the second-order equation. The change in the coefficients seen is easily explainable if we consider Eq.3.4 and remember that the TPA coefficient σ depends on the entanglement area A_e and time T_e. These properties of the entangled field will also be dependent on the parametric gain and will cause the eSFG interaction coefficients to change.

While we were able to isolate the effect of the losses by compensating for the reduction in PDC power through increased PDC gain, controlling other changes in the PDC state introduced by the different gains was beyond our control. This solidifies the idea that adding losses to the PDC far field is not the appropriate approach for demonstrating a quantum enhancement from the use of entangled photons to generate multiphoton interactions. Therefore, a comparison with a classical beam is necessary. But first, we will discuss the change in the PDC state at different interaction gains.

3.3.1 Characteristics of squeezed vacuum at different gain levels

During our investigation, it became evident that the produced squeezed vacuum would change its properties when a different gain regime was accessed. This change was first observed when looking at the PDC near field, with the beam profile at low and high gain shown in Fig.3.15. A similar change was then expected to be observed at the temporal profile of the PDC state. In this subsection, these changes will be presented, and their consequences will be discussed.

We start by formulating equations that describe the observed effect. Firstly, we take a look at the gain equation 2.15, introduced earlier. We consider the spatial distribution of the pump power P_p. We start from the intensity profile of the beam propagating along the z direction:

$$\mathrm{I(r,z)} = \frac{\mathrm{2P_0}}{\mathrm{2\pi w_0^2}} \left(\frac{\mathrm{w_0}}{\mathrm{w(z)}} \right)^2 \exp\left(- \frac{\mathrm{2r^2}}{\mathrm{w(z)^2}} \right) \tag{3.14}$$

where w_0 is the beam radius and r is the radial distance from the centre axis of the beam. In general, power at an incident plane S is $P(z) = \int_S I(r,z)dS$, and an integration of the intensity profile over the polar coordinates can be performed. In our case, the pump power is $P(z) = \int_r I(r,z)dr$. The result can be substituted back into the parametric gain

parameter in Eq.2.15:

$$N_{PDC} = \text{asinh}^2\left(\Lambda\sqrt{P_0}\exp\left(-\frac{S^2}{2w(R)^2}\right)\right) \tag{3.15}$$

Now, we have an expression for the number of PDC photons produced as a function of the pump power's spatial distribution. Of course, the hyperbolic sine $\sinh^2$ can be then rewritten as $\sinh^2(\theta) = ((e^{\theta} - e^{-\theta})/2)^2$ and Eq.3.15 can be expressed as:

$$N_{PDC} = \text{aexp}\left(2\Lambda\sqrt{P_0}\exp\left(-\frac{x^2}{2w(R)^2}\right)\right) \tag{3.16}$$

From the above expression, it can be seen that as the pump's peak intensity increases, more PDC photons are produced, but the spatial distribution of the PDC state also changes. As earlier-generated photons begin to seed the production of new photons, the width of the PDC birth-zone will shrink.

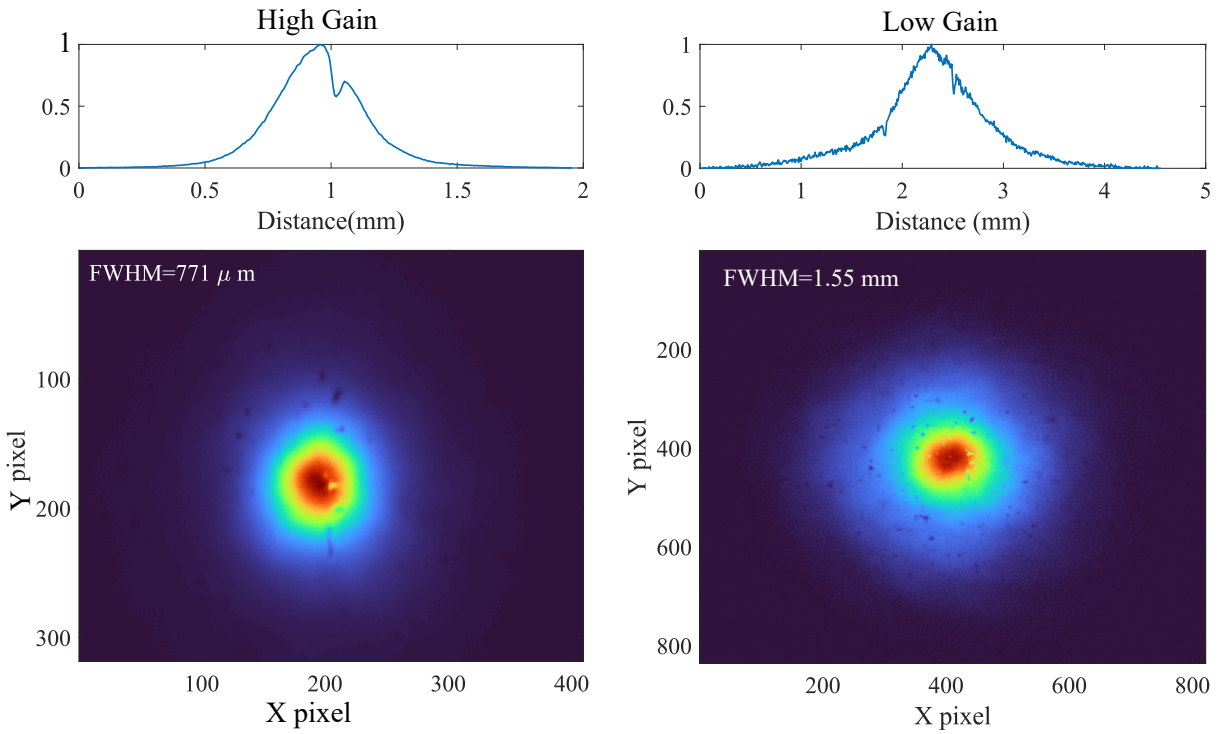

Figure 3.15: **High gain and low gain near field beam profiles of PDC**. The image on the left was taken at the SV's high gain, while the image on the right corresponds to the SV's near-field beam profile at low pump power.

As the pump's Gaussian profile increases in the middle for higher pump energies, there will be a higher conversion of pump photons residing in its centre into PDC photons, in contrast to those located around it. Changes in the PDC field across different gains will, in turn, affect the correlation and coherence volumes. At low gain, these changes are

not expected to affect the two-photon interactions, as the correlation and entanglement volume will still depend on the pump beam. As the gain increases, a narrowing of the PDC spatial and temporal characteristics will occur, as the pump's intensity distribution will increase in the middle of the Gaussian, causing those components to produce more than others [39].

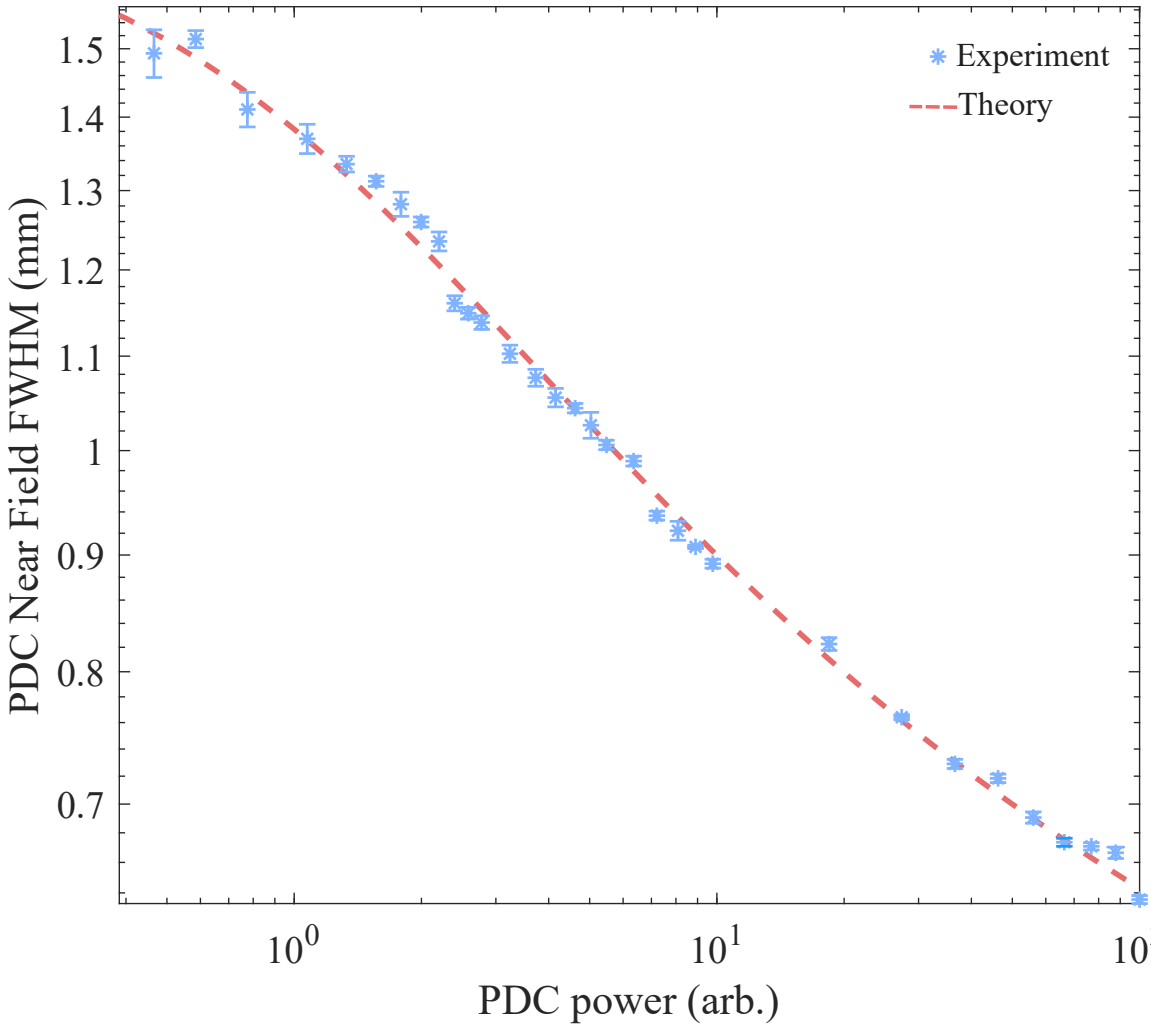

Figure 3.16: **PDC near field size fitted with the quasi-stationary model.**

We continue by expanding the exponential term of the Gaussian in Eq.3.16 so that:

$$\exp\left(-\frac{x^2}{2w(R)^2}\right) \simeq 1 - \frac{x^2}{2w(R)^2} \tag{3.17}$$

and then the above can be substituted back into Eq.3.16. From that, we can derive an expression for the near-field of the PDC as a function of the pump power, which reads as:

$$\mathrm{w_{PDC}} = \frac{\mathrm{w(R)}}{\sqrt{\Lambda\sqrt{\mathrm{P_0}}}} \tag{3.18}$$

Now, we can conclude that, for the results shown in the previous section, each time we increased the pump energy to match the PDC photon number in the absence of losses, we inadvertently changed the PDC spatial properties. For the data shown in Figure 3.13, when 90% losses were added in the far-field of the PDC, it produced more SFG photons per pulse than the case when no losses are present in the PDC because the peak intensity of the PDC field was higher. This unintentional change in the PDC beam profile reinforces the argument that, to claim any quantum advantage, a comparison of the quantum process with its classical counterpart is essential. Although the effect of losses was isolated, this approach yielded state characteristics that varied across cases.

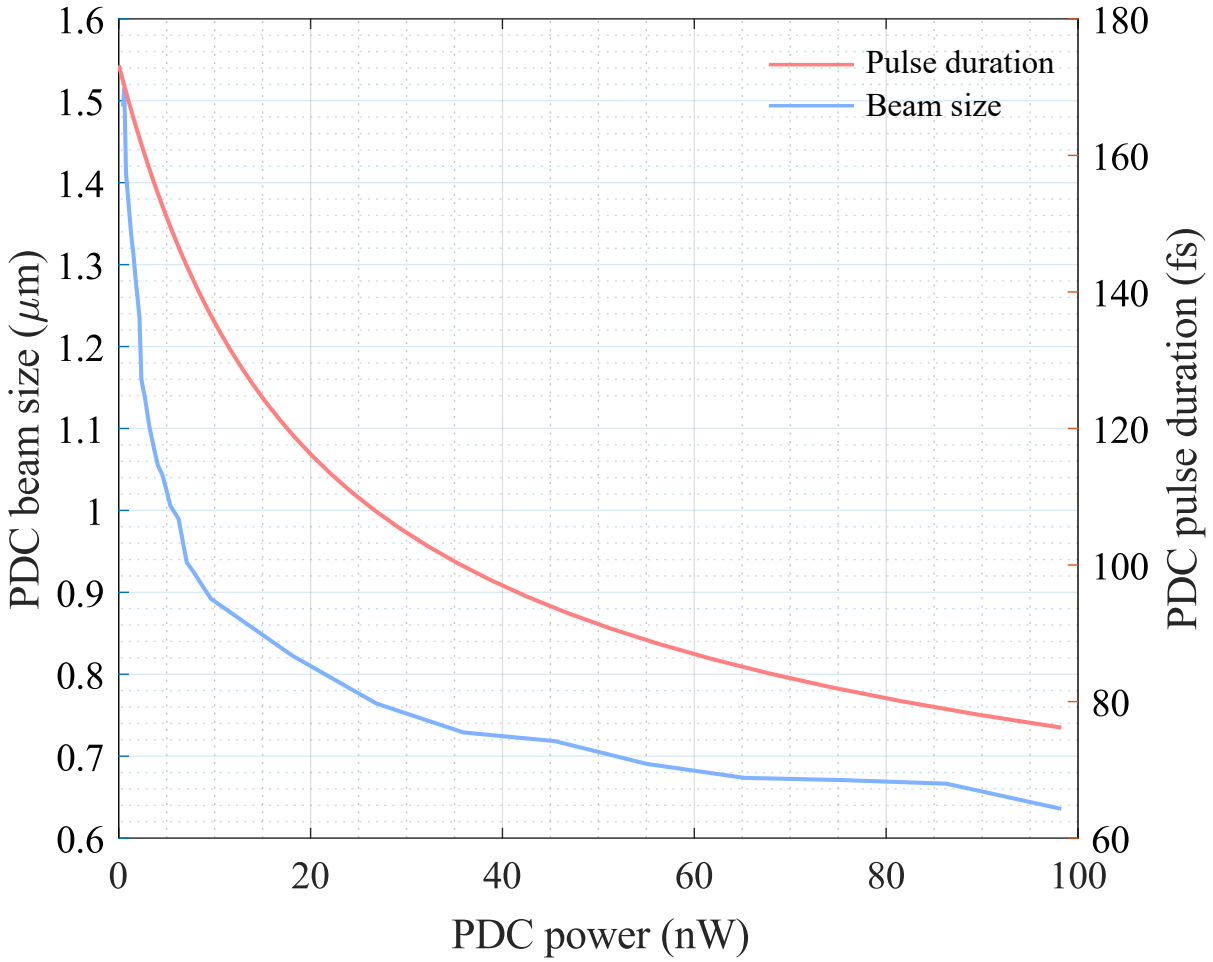

Figure 3.17: **PDC near-field size and pulse duration**. The beam size was measured using a CMOS camera, and the pulse duration values were obtained via MATLAB simulations.

We measured the PDC size at the surface of the SFG crystal, and now the data can be fitted using Eq. 3.18. The fit agrees with the data, but a slight deviation from the low-gain data points is noticeable. This was expected, since Eq. 3.18 is valid only in the high-gain regime. Instead, equations from the quasi-stationary model developed in [37, 55] can be used to fit the data. More specifically, the model describes the change of the

transverse spatial profile of the PDC at different parametric gains, and an equation can be derived to describe the near-field of the PDC:

$$w_{PDC} = \sqrt{\frac{\tanh(g)}{4g}}\Delta x \tag{3.19}$$

The data with the corresponding fit is shown in Figure 3.17. The equation shows good agreement with the experimental data, from which it is observed that at low PDC gain, its near-field size (FWHM) matches that of the pump beam. Taking this into consideration, we proceed to make a meaningful comparison between classical and quantum SFG.

3.4 Comparison with a coherent source

From the previous section, two main conclusions can be drawn. Firstly, a quantum advantage above the one-photon-per-mode regime should still be present in quantum two-photon interactions, as seen from our measurements of spoiling the entangled correlations by adding losses to the state. Secondly, a comparison of the quantum process with its classical counterpart is essential to claim a quantum advantage, since, although the effect of losses was isolated, this approach yielded state characteristics that varied from case to case. Our next goal was to compare classically generated SFG and entangled SFG. This would allow us to accurately investigate at which point the efficiency of SFG with a coherent field becomes comparable to that of an entangled field. To perform this measurement, it was essential to make a fair comparison in which both cases involved radiation incident on the SFG crystal with matching properties. Since SFG scales with pump intensity, we aimed to match the average intensity of the light arriving at our SFG crystal. Because the entangled-state characteristics change with different gains, this was not straightforward. For each data point, not only did the power need to be adjusted, but also the beam size and pulse duration. For this reason, the setup shown in Figure 3.18 was built to allow us to adjust these and Figure 3.17 was used to adjust the classical field accordingly.

The setup is shown in Fig.3.18. A beam from Orpheus-F OPA by Light Conversion was incident on a 0.5 mm-long BBO crystal to upconvert from 2060 nm to 1030 nm. The resulting SHG had a spectral bandwidth of ∼30 nm and a pulse duration of ∼100 fs, preferred over the laser output, which has a much longer pulse width than the SV at high gain. This was then sent to a makeshift pulse compressor with two UVSF prisms (Eksma 320-1218) in a double-pass geometry. Translation stages were used to vary the path length through the prisms and their separation, thereby controlling the dispersion added. More specifically, positive dispersion could be added with the first stage and

negative dispersion with the second stage. After the pulse compressor, spatial filtering was implemented to reject any unwanted radiation. This was achieved using two lenses to collimate the beam and a 100 mm pinhole at the telescope's focal point, ensuring the beam exited the telescope with a Gaussian profile. After spatial filtering, the spectrum was checked to ensure it remained unchanged by the pulse compressor and pinhole. A zoom beam expander (Thorlabs ZEB11) was then used to adjust the beam size, and finally, a variable-energy controller was employed to set the power to the desired value. The table below displays the near-field beam size for the chosen PDC photon per pulse arriving at the second crystal, along with the parameters of the classical field. After those were set, the radiation energy was adjusted to achieve the desired number of photons per pulse incident on the SFG crystal.

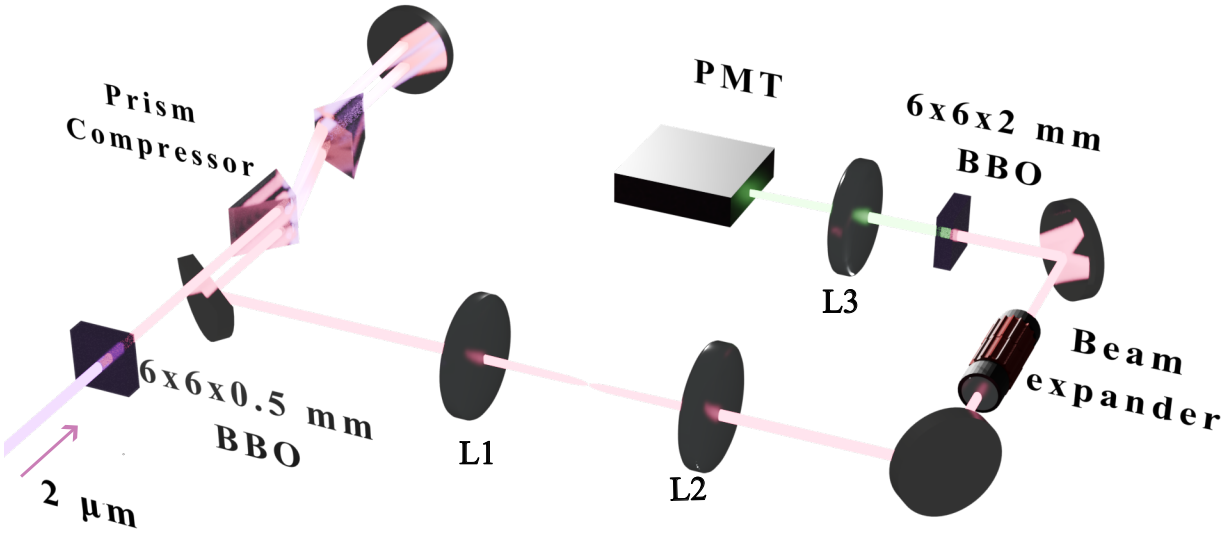

Figure 3.18: **Apparatus for classical SFG** The 2 µm beam from the OPA is sent to a BBO crystal to produce SHG, which acts as the classical pump for the SHG process. Pulse duration and beam size are controlled by a prism compressor and a beam expander, respectively. Lenses L1 and L2 had a pinhole placed between them, to ensure a Gaussian beam profile.SFG is produced at 515 nm and measured using the same PMT used for the quantum experiments.

It is worth noting that, although this was our best attempt to replicate some of the PDC's properties in the classical field, we were unable to match others. Firstly, the PDC is broadband, with a 70 nm bandwidth, whereas our coherent source had a 30 nm bandwidth. This made the comparison between the fields more biased in favour of the classical case, since a smaller bandwidth pulse is much easier to convert efficiently and cleanly. Another critical difference is the modes that are present in the PDC radiation. The squeezed vacuum is a multimode source, in which photons occupy each mode and therefore exhibit intensity fluctuations, whereas the classical field has only one spatial mode.

Table 3.1: **Classical and quantum field properties.**

Photons per pulse at SFG crystal (10^3)	PDC FWHM beam size (mm)	Classical field FWHM beam size (mm)	Classical field pulse duration (fs)
1.0	1.49±0.05	1.48±0.05	173±5
12.3	1.40±0.05	1.33±0.05	170±5
39.5	1.36±0.05	1.16±0.05	165±5
81.1	1.10±0.05	1.07±0.05	158±5
248.8	0.92±0.05	0.90±0.05	137±5

The main results are shown in Fig.3.19. Even though experimentally the classical field was given an advantage, for the reasons mentioned above, we see a quantum advantage up to ∼9.3 photons per mode, ten times higher than the regime where it was thought the process becomes more efficient for a classical field. The orange line in Fig.3.19 A represents the theoretical curve from the model provided in [37]. Similar to the entangled case, the theoretical curve was obtained by multiplying the theoretical results by a 0.76 factor, which accounts for the correction for the d_{eff} and losses introduced by the experimental setup. There are five data points, each representing the SFG response at five different settings. The input pump power, beam size and pulse duration were adjusted according to Table 3.1, each one matching the squeeze vacuum properties at different gains. For all five cases, a complete power scan was performed, recording the SFG response from the PMT as a function of the input classical field power. Each data point on the orange line was selected from the complete power scan performed between the classical field and the produced SFG response in post-processing, ensuring that the effect would scale as expected. The coefficient obtained from the theoretical curves is proportional to the effective coefficient d_{eff} and equals 1.65 pm/V. Then, the desired data point (that matches the input photons per pulse of the entangled light) at each setting was extracted and added to the plot, with all data points forming a second-order scaling of SFG.

The ratio between the classical and quantum SFGs was calculated to assess the efficiency of the quantum enhancement. From Figure 3.19 B, it can be seen that there is a ∼35 fold enhancement for quantum SFG, for identical input photons per pulse at the SFG crystal, confirming the advantage of using entangled photons for two-photon interactions. This enhancement drops as we enter the stimulated regime of PDC, but it persists until ∼10 photons occupy each mode. More specifically, the two fits for the quantum and classical SFG efficiency scaling in Figure 3.19 A, plotted in blue and orange lines, respectively, meet at 9.3 photons per mode. The eSFG measurements presented here were done by filtering out the incoherent part of the produced eSFG to exclude the interaction

of uncorrelated photon pairs. However, this incoherent light is a unique signature of the eSFG process and therefore contributes to the overall efficiency. If included, it should introduce a term to the second-order term of the quantum process. We wanted to confirm this experimentally, so a full eSFG scan was performed next.

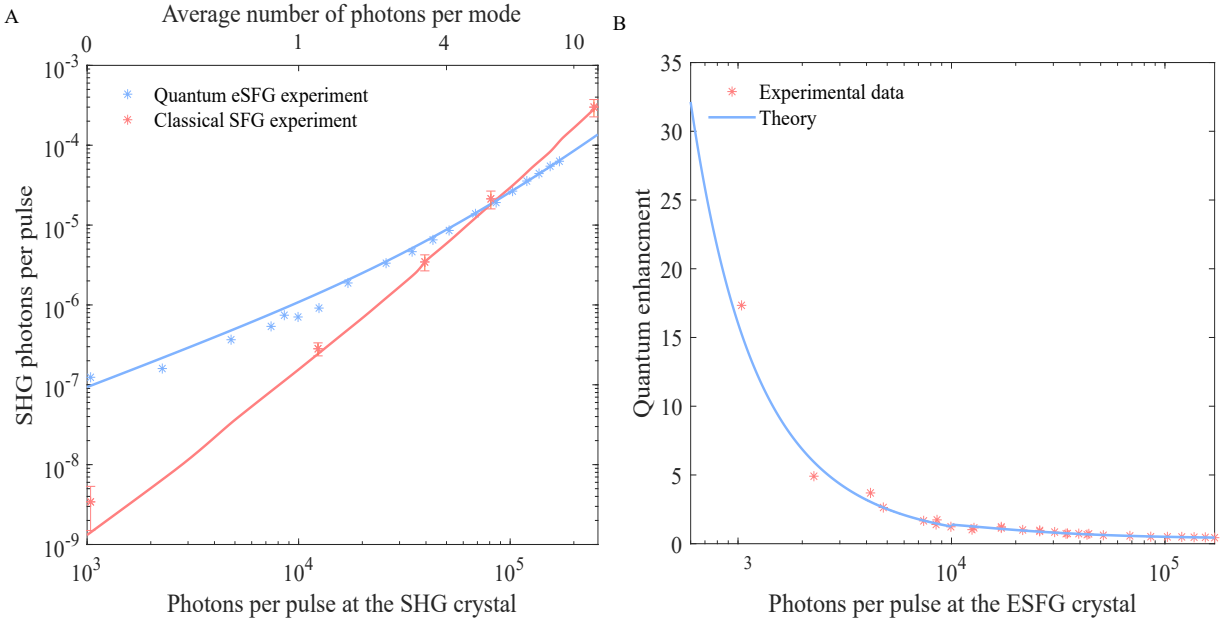

Figure 3.19: **Comparison of eSFG's efficiency with SFG from a classical laser pulse. A** Shows both the eSFG response (blue points) and SFG response produced from a classical laser pulse (orange points). The blue and orange lines are the curves obtained from the theoretical model for the quantum and classical SFG, respectively. We observed a quantum advantage of up to 9.3 photons per mode, a regime ∼10 times brighter than previously thought possible. In **B**, the ratio between the quantum eSFG and the classical SFG is plotted. In orange points are the experimental values, while the blue line represents the ratio between the curves obtained from the theoretical model.

Figure 3.20 shows the results from comparing classical SFG with all components of eSFG, including both coherent and incoherent contributions. Unfortunately, we returned to the quantum experiment after completing the classically produced SFG comparison, and changes in the quantum setup's gain were observed, attributed to misalignment-induced losses. Therefore, the results shown in blue on Figure 3.20 are not comparable with the results on Figure 3.19 A. Nevertheless, a quantum advantage was still observed for each case. For the length of the SFG crystal we used, the classical SFG will eventually produce more counts per pulse than the quantum SFG, but eSFG will remain more efficient for longer when the incoherent component is present. This confirms that, beyond the one-photon-per-mode regime, coherent and incoherent contributions are amplified in a similar manner, with the spatiotemporal correlations being preserved through the different gains of the SPDC. The uncorrelated portion of the PDC doesn't overwhelm the correlated one, and hence it contributes meaningfully to the overall efficiency of eSFG.

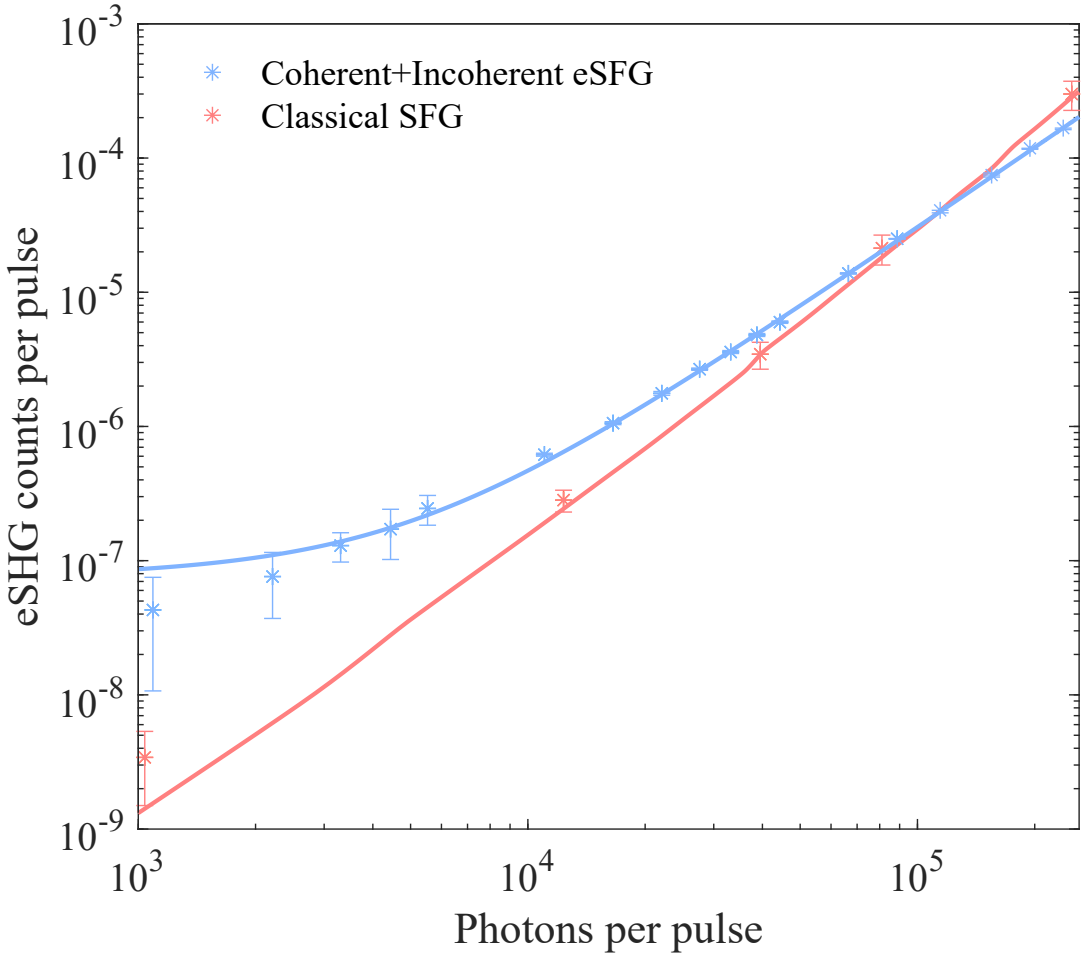

Figure 3.20: **Comparison with incoherent component.** The iris at the far-field of the PDC was open to allow for the incoherent radiation to reach the PMT. We observe that the SFG remains more efficient for longer than when only the coherent contribution is measured. Unfortunately, these results are not comparable to the ones shown in Figure 3.19 due to discrepancies in the experimental setup.

As suggested by the theoretical work in [37], the optimal setup for eSFG implements a shorter crystal for upconversion than the one used to produce the photon pairs. To confirm this, the upconversion crystal was replaced with a 1.5 mm-long BBO crystal, and the measurement described in the previous sections was repeated to record the eSFG efficiency. This time, instead of performing a comparison with the classical produced SFG, the results obtained previously, shown in Figure 3.19 A (in orange), were used to acquire a theoretical projection of the classical SFG response for the shorter crystal. Given that the SFG rate should increase with the square of the crystal length, the data were scaled accordingly. The scaling of SFG produced by classical and quantum light is shown in Figure 3.21, with quantum SFG being more efficient. This time, both the coherent and incoherent components were measured.

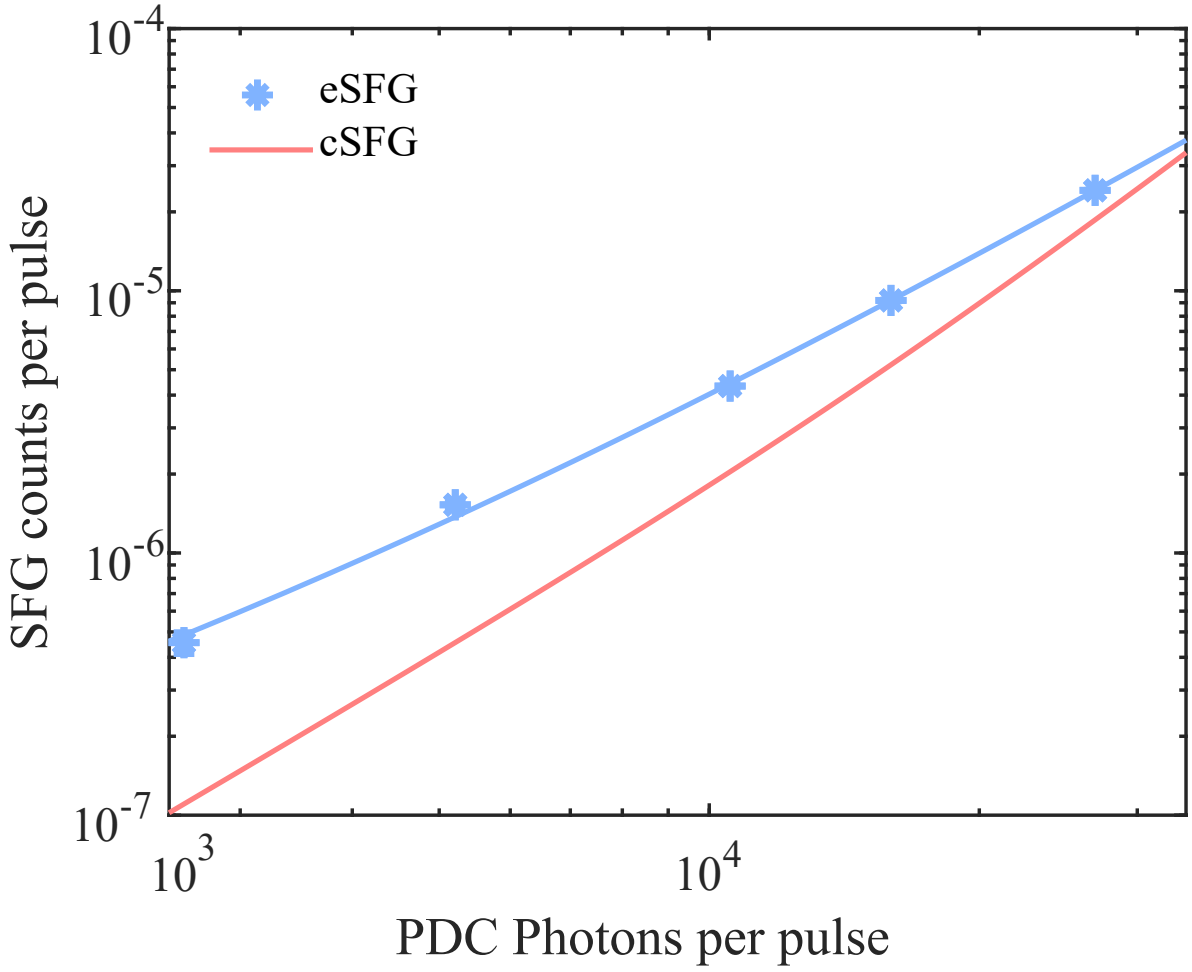

Figure 3.21: **Comparison between classical and quantum SFG from shorter crystal.** The above blue data points display the measured scaling of eSFG from a 1.5 mm BBO crystal, while the orange line represents the expected SFG response from a classical beam that has the same parameters as the SV. For the measured input SV energies the quantum SFG remains more efficient than the classical.

In general, a shorter crystal produces fewer photons than a longer one, since the efficiency of nonlinear frequency conversion scales with crystal length. But if we isolate each event and only compare the classical to the quantum interaction, we observe that when the conversion happens in a shorter crystal, not only will non-classical photons produce more SFG photons than a classical beam, but the classical SFG won't surpass the quantum SFG for the range of powers we had. This happens because of the larger bandwidth of the shorter crystal, allowing a much higher number of PDC modes to be phase-matched in the SFG crystal.

3.5 Conclusion

This work involved the optimisation of multimode parametric down-conversion to produce eSFG that scales linearly while still yielding a signal considered bright enough for imaging and metrology applications. The setup used to accomplish this is explained in this chapter, alongside the most significant results. By implementing a multimode, multiphoton PDC source, we were able to produce eSFG signals at low SPDC gain that were bright enough to study the process even when losses are present in the SPDC source. In contrast to previous research, we were able to isolate the effects of the losses by maintaining the same number of PDC photons undergoing upconversion across all loss cases. At low SPDC gain, losses reduced the efficiency of the eSFG process. A first-order polynomial was used to model the eSFG response, which matched the experimental data. The first-order coefficient from the theoretical model was found to be proportional to the transmission of ND filters used to introduce losses in the entangled field.

In this chapter, we also examine eSFG when higher powers of PDC are used to excite the process, thereby inducing the effect in a regime where previous research had thought it impossible to observe any quantum advantage. Similar to the low-gain regime, the SFG efficiency remained higher when no losses were present in the state. This stopped at the SV's high-gain regime, with the more lossy state eventually producing more SFG. This effect was attributed to the fact that, as we tried to maintain the same number of PDC photons reaching the nonlinear crystal, a higher PDC gain was required. This resulted in a state with higher peak intensities when more losses were present. The effect of losses in the state was described using the rate equation for eSFG, which predicted a higher SFG efficiency produced from a lossy PDC state. The model and the changing peak intensities of PDC at different gains demonstrate that adding losses to the state is insufficient to claim a quantum advantage; therefore, we proceeded to a direct comparison with its classical counterpart.

The properties of the SV were measured as the process gain varied, with the goal of matching them to a classical radiation that would act as a pump for the classical version of the process. Our results showed that the eSFG produced more photons in the regime where $\sim$10 photons per mode were produced in the PDC. After that, the SFG from a classical pulse begins to generate more photons. The results from the comparison and the effect of losses in the PDC state agree with the theoretical work of Gatti et al., and therefore they were published in [94]. While this is not the first work to compare the scaling between entangled and classical SFG, the comparison presented here is the most straightforward. For example, the work of Spasibko et al. provides a comparison between a bright SV state and a SV state with fewer quantum fluctuations, where the bright SV

state produces more photons for the multiphoton processes under study [76]. Another comparison was made by Landes et al., who compared the TPA response from an SV and a classical beam. To account for spatial differences, they decided to couple both the SV and the classical light into a single-mode fiber, with the output being focused into the R6G sample. While they measured an entangled TPA that was 1.8 times more efficient, their experimental method likely introduced losses in the state and could only be used to examine the two-photon process at the SV's high gain. While the authors appear to be aware that the SV pulse duration changes with gain, they assumed it remains almost constant, an assumption valid only when proper state characterisation is performed, a measurement missing from their publication.

It was of special interest to further investigate the effect by exploring real-life applications. Therefore, I decided to focus on imaging the signal from the nonlinear quantum-enhanced interaction and to study the impact of light generated by quantum SFG on imaging applications. The results of this study are discussed in the next section.

CHAPTER 4

Nonlinear imaging with entangled photons

4.1 Introduction

With the findings described in the previous Chapter, the next direction for this research was to image the nonlinear signal produced by entangled photons. Such a realisation would allow us to examine whether the process is helpful for real-life applications. We've seen so far that entangled photons can enhance the efficiency of the eSFG process at the low gain of PDC, as well as at a regime above what was previously thought possible. This implies that the second harmonic or two-photon excited fluorescence from a biological sample could be imaged using an entangled beam acting as a pump, at lower powers than conventional lasers. This implies that photobleaching damage could be avoided, with samples lasting longer, and the possibility of capturing images at a regime where the low Signal to Noise Ratio (SNR) would have rendered it impossible before.

Researchers have already capitalised on this, with attempts to image biological tissue and fluorescence dyes using the process of two-photon absorption, with Goodson et al. being the first to image fluorescence from a drop-cast film from a bis(styryl)benzene derivative using quantum light [95]. They claimed to have witnessed an enhancement when six orders of magnitude less excitation power was used to excite the fluorophore. They later use Hoechst 34580 dye to image breast cancer cells [96], this time using a CW source to generate their entangled photons. Both papers lack characterisation of the entangled state used, as well as controls to distinguish between quantum and classical effects. Additionally, no losses were added in the entangled state to show a quadratic scaling, or a reduction in their efficiency, as done in this thesis, to confirm that the light measured was a result of two correlated photons interacting together. This could have led to misinterpretations or overestimation of the results. Nevertheless, the results obtained from Goodson's group and previous investigations, presented in the literature review in the introduction, suggest that much lower powers can excite biological samples when an

entangled light source is used. However, technical difficulties can have an adverse effect on observing the effect, as long acquisition times are still required if a sCMOS sensor is used, ~ 2 hours as reported in [96].

Apart from these papers, no other research has been conducted to date to explore nonlinear imaging from entangled sources acting as a pump. Of course, this is true only for Two Photon Absorption (TPA) and SFG as other nonclassical techniques have been introduced to microscopy [97–99], since quantum light sources show nonclassical features that, when utilised for imaging and microscopy applications, can help overcome limitations imposed by classical optics. By leveraging SV, Casacio et al. managed to increase the SNR in a Raman microscope [97]. Quantum Optical Coherence Tomography (QOCT) has also been demonstrated, and an enhancement in axial resolution was achieved [100]. In a paper by Kazuki Hashimoto et al., it was shown that QOCT can be achieved without the need for a beam splitter by implementing SU(1,1) interferometry techniques. They also performed QOCT at the high gain of PDC [101], showing that detectors with medium sensitivity can be used to measure the light incident on the sample, while still preserving non-classical effects. Furthermore, quantum states of light can be utilised to enhance the resolution of imaging systems. In general, resolution is limited by diffraction as stated by Abbe and Rayleigh [102, 103]. But when quantum light is used, the resolution can be improved by a factor $1/\sqrt{N}$, known as the standard quantum limit [104, 105].

These imaging improvements were observed across both PDC regimes, demonstrating that although the correlations change, they remain present. Due to this, it was of interest to investigate what happens not only in the low-gain regime, with the characteristic linear scaling in efficiency, but also in the bright regime of our PDC, where higher-order photons are generated beyond single-photon pairs. When our state undergoes up-conversion to reproduce the pump, characteristics of the entangled state are encoded in the interaction. This can be observed in the production of the incoherent signal, which arises from the interactions between non-entangled photons and therefore follows the underlying field statistics, which are thermal, as PDC is seeded from the thermal vacuum. In contrast, the correlated photons that interact coherently in the nonlinear crystal contain information about the pump photon that created them and will therefore give rise to the coherent contribution. At different gains of the PDC process, the incoherent SFG contribution is not always present, with only the correlated eSFG peak observed at low PDC gain. Given previous evidence that the statistics of light can alter the imaging resolution of a system, the objective of this investigation was to observe how imaging changes across different regimes of PDC. A theoretical investigation of the effects of the incoherent and/or coherent components of SFG on imaging is given later in this Chapter. First, an overview of second-harmonic imaging techniques is provided.

4.2 Second harmonic imaging

Second-harmonic imaging is widely used to map the biological structure of samples that exhibit χ^2 nonlinearities. As soon as the first laser was built, Franken et al. demonstrated second harmonic by shining a red ruby laser beam through a quartz crystal [106]. A decade later, Fine and Hansen reported the first observation of SHG produced by biological tissue, and since then, techniques to improve the low SNR and weak penetration have been introduced [107]. For example, to increase the penetration depth, NIR-2 laser sources (1000-1300 nm) can be used, in contrast to the most commonly used NIR-1 (700-1000 nm) sources, as longer excitation wavelengths result in reduced scattering. However, depending on the sample under study, SHG production can be reduced when working with longer wavelengths; therefore, a careful parameter selection is necessary [108].

In biological samples, a molecule's ability to produce SHG stems from its hyperpolarizability, a measure of its second-order electric susceptibility per unit volume [109]. Similar to a nonlinear crystal fabricated in the lab, a molecule's hyperpolarisability, β, depends on its structural symmetry. As we've seen in the introduction to this thesis, only non-centrosymmetric materials can produce SHG because they lack a centre of symmetry. Macroscopically, the hyperpolarisability of the sample can be given by the individual hyperpolarisabilities in the harmonophores by:

$$\chi^{(2)} = N_e < \beta > \tag{4.1}$$

where N_s is the density of the molecule. The most common is the imaging of collagen, the most important structural protein of the animal body, found in connective tissues. Collagen Types I and II are found in skin and elastic cartilage, respectively, and form triple helices that are organised together in fibrils. Unlike fabricated nonlinear crystals, collagen is a nematic liquid crystal with inherent structural randomness and dispersion. That's why SFG produced from tissue can have a nonzero mismatch Δk. Therefore, it can sometimes back-propagate; SFG imaging microscopes now take this into account by having two collection points: one for forward-propagating SFG and one for back-propagating SFG.

To study the structure of a biological sample using eSFG, two main practical requirements must be met. A mode-locked femtosecond laser, along with a laser-scanning microscope, is required. Most commonly used are Titanium sapphire lasers, with excitation wavelengths ranging from 700 to 1000 nm. For a laser with an 80 MHz repetition rate and 100 fs pulse duration, 10 mW is enough to excite SHG in collagen when the beam is focused at the sample using a microscope objective [110–112].

4.2.1 Imaging of biological tissue

Taking the above into consideration, I attempted to excite SHG from a biological sample using PDC. To this end, horse liver samples, mounted on a 1 mm microscope slide, were acquired by the Beatson Cancer charity. Liver is rich in Type I collagen, and I tried to image regions of our sample that had visible damage, since tissue damage can cause collagen deposition [113, 114]. The sample and the area where we attempted to generate the second harmonic are shown in Figure 4.1.

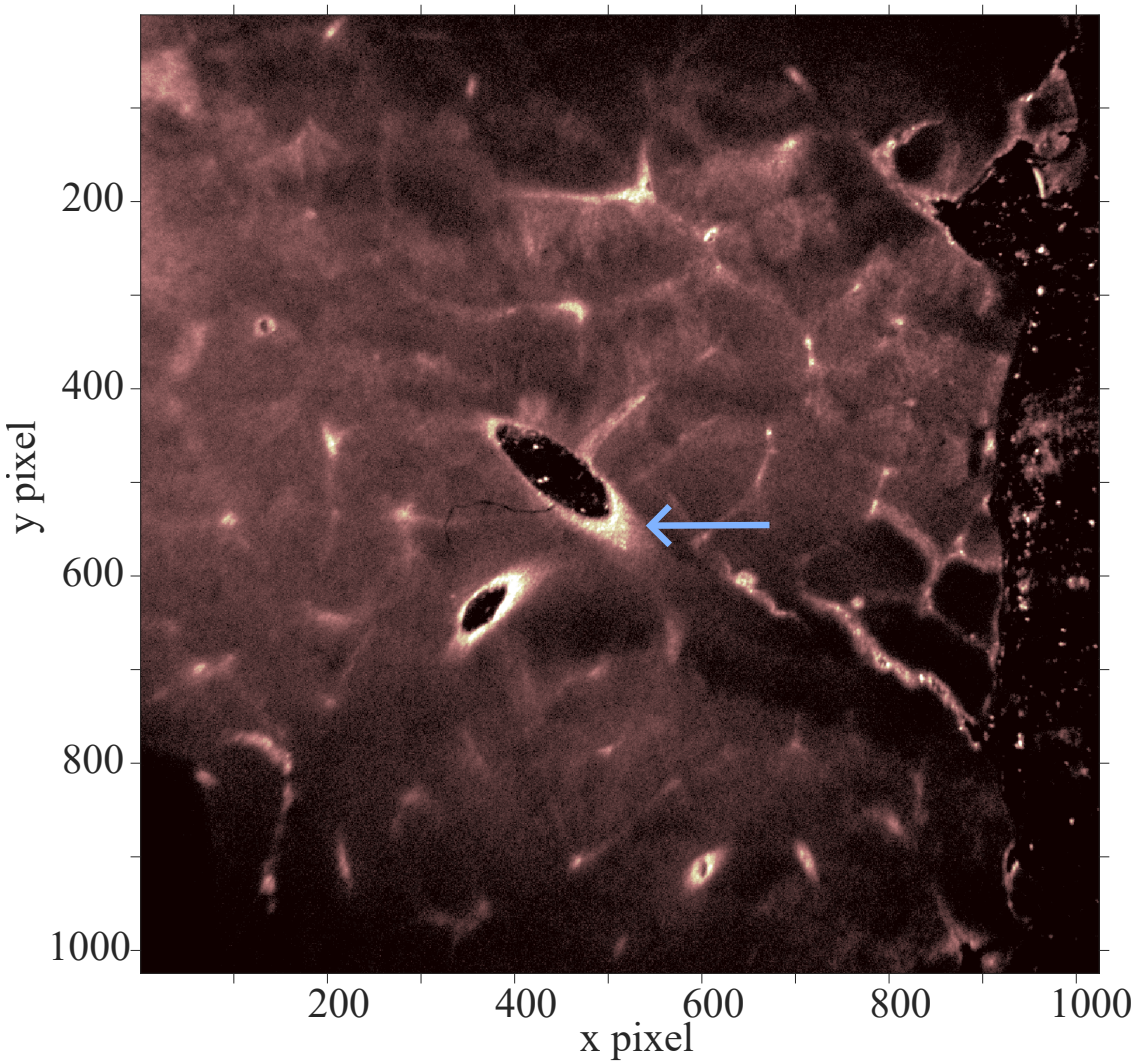

Figure 4.1: **Liver sample is imaged using scattered light** to the EMCCD. The blue arrow indicates the point where the excitation pump was incident.

For imaging, we switched from using the PMT to an Electron-multiplying CCD (EMCCD) image sensor. Unlike regular Charge-Coupled Device (CCD), EMCCDs consist of a multiplication register that amplifies the signal before passing it to the charge amplifier. Therefore, readout noise is effectively bypassed, enabling high-sensitivity image

acquisition. Additionally, the multiplication register enabled us to exploit the Clock-Induced Charge, an inherent effect in CCDs. It occurs during charge registration, which can sometimes result in the creation of additional charges. Therefore, signal amplification can occur, and its magnitude can be adjusted by selecting the gain in the EMCCD's multiplication register.

Before attempting to excite eSFG from the sample, a classical beam was used to measure its SFG response. This was done to help calculate the necessary exposure times to image eSFG on the EMCCD by comparing the peak intensities of the classical beam to the maximum available from the SV. To make the comparison as accurate as possible, the infrared output beam from the laser used in the quantum experiment was set to be incident on the sample. A telescope was built to match the PDC near field size when the PDC is at its maximum, with the only difference being the pulse duration. As described previously, the SFG signal is maximised when the incident light's polarisation matches the orientation of the fibrils in the collagen. Therefore, the polarisation was optimised in our experiment too, resulting in almost a twofold enhancement in counts on the EMCCD when the polarisation of the incident light was set to vertical, with the results shown in Figure 4.2.

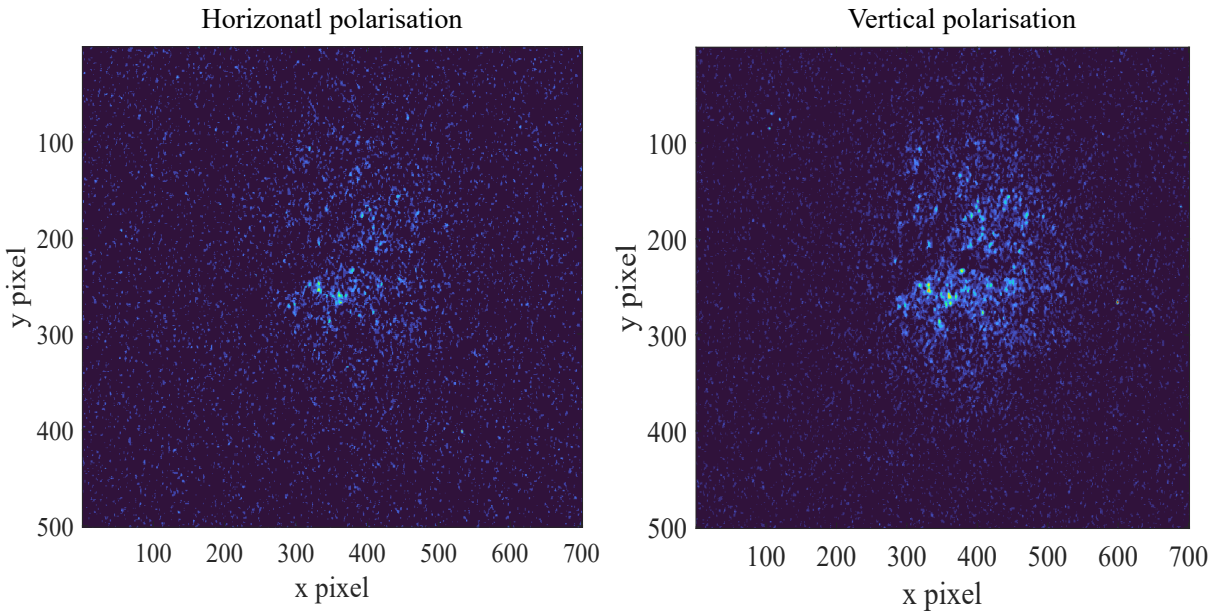

Figure 4.2: **Polarisation optimisation for higher SFG response.** This was done to ensure that the polarisation of the excitation light aligns with the fibrils in the collagen of the sample.

With the polarisation optimised, the power of the pump laser was set to 30 mW, and a five-minute acquisition on the EMCCD was sufficient to capture the signal produced at 515 nm. The image of the produce signal is shown in Figure 4.3. In five minutes of acquisition time, the counts recorded on the camera were around 100, which meant that,

after correcting for the camera's efficiency, the produced signal was $\sim 2\times10^{-6}$ photons per pulse. This was achieved with a pump peak intensity ∼6 orders of magnitude higher than that produced by the PDC. Unfortunately, to match the peak intensity of the classical field, the near field of the PDC needs to be resized to ∼10 µm, a value that is not practical for our case due to our entanglement area, which is ∼23 µm as reported in the previous Chapter. While others have managed to use objectives to shrink the PDC state to a few µm, they've done so because they had only one spatial mode available [65, 66]. In our case, we are spatially multimode and resizing the near field to a size smaller than our entanglement area would have possibly caused the spatial modes to overlap. It is essential to note that resizing the near field to produce eSFG would only enhance the overall eSFG, rather than improving the quantum effect of the linear scaling observed previously, as described in Chapter 3. This is because linear enhancement is observed when the photon pair is brought together to interact. Thus, the efficiency of the linear term should depend on the number of modes, with more modes indicating a higher number of photo pairs.

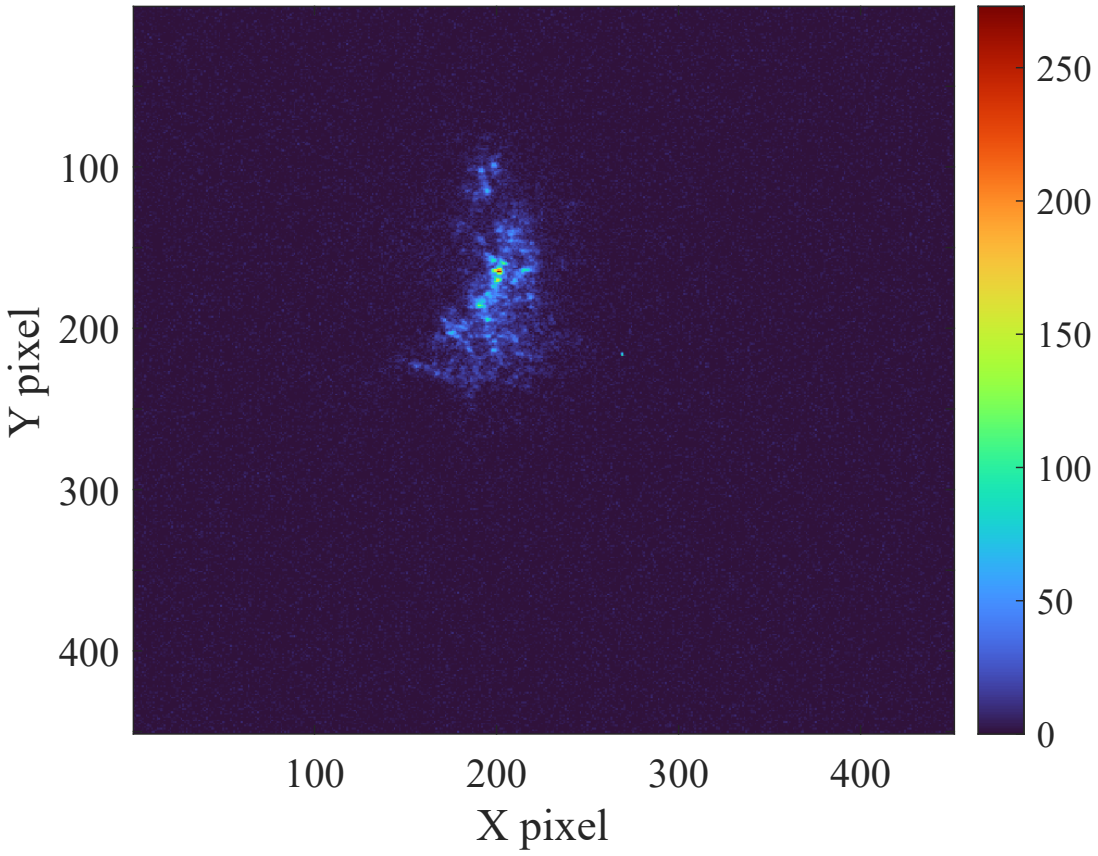

Figure 4.3: **SFG from biological tissue stimulated by classical radiation.** The above was taken with an exposure time of 300 seconds after optimising the polarisation.

Without the option to resize the near field, the only remaining option was to calculate

the exposure time the EMCCD camera should acquire to obtain the same SFG response from the quantum source. Unfortunately, the estimated exposure time was impractical, and therefore, it was concluded that eSFG imaging of the liver sample was not possible with the current source. Limitations such as the peak intensity achievable from the entangled photon source and the low response of the biological sample were the main challenges to imaging the entangled generation of second-harmonic light produced by collagen. We decided to adopt a new technique to enable us to conduct our investigations.

4.3 Parametric Upconversion Imaging

We then transitioned to a simplified eSFG imaging scheme inspired by Parametric Upconversion Imaging (PUI). Using this technique, an Infrared (IR) image undergoes image upconversion to capture images of objects with sensors that respond to visible wavelengths and have better bandwidth and efficiency, and remain unaffected by background thermal radiation. In simple terms, upconversion imaging is a technique in which an object is placed in the path of a beam, which is then imaged onto a nonlinear crystal to produce its second harmonic. This effect is described using classical electromagnetic theory, where the object is characterised by a spatially complex electromagnetic field distribution. A similar equation to Eq.2.10 is obtained for the up-converted field intensity. Unlike the mathematical derivation of the expression introduced in the Introduction, where differential coupled equations are used, in PUI, a mathematical expression for the upconverted electric field is obtained instead, which is a mathematical expression of the Huygens-Fresnel principle in a $\chi^{(2)}$ medium. A detailed derivation can be found in [115, 116]; however, a brief overview of the equations most relevant to this research is provided here.

Let's consider the following setup of an object imaged on a crystal with length l_c. Infrared radiation with beam waist w_0 is incident on the crystal, and upconversion of the radiation at the visible band occurs. The visible radiation can be used to image the object. By focusing on a wave-vector space analysis of the interacting fields, an expression for the FWHM of the upconverted intensity in k-space can be obtained. The upconverted field amplitude $\tilde{A}(\Delta k_\perp, \Delta k_z)$ is defined as:

$$\tilde{A}(\Delta k_\perp, \Delta k_z) = \frac{2\pi w_0^2 d_{eff} \omega_{up}^2 l_c A_{IR,2} A_{IR,1}}{c^2} e^{\frac{-\Delta k_\perp^2 w_0^2}{4}} sinc(\frac{\Delta k_z l_c}{2}) \tag{4.2}$$

where $A_{IR,1}$ and $A_{IR,2}$ the incident infrared pump photons' field amplitudes and the rest of the parameters have been introduced in the introductory Chapter 1. The angular spread

of the upconverted field $\Delta k_{\perp,FWHM}$ can be derived for the above expression. This is done by assuming that $\Delta k_z l_c << \Delta k_\perp w_0$, which is equivalent to a thin filter approximation, and the obtained expression is:

$$|\Delta k_{\perp,FWHM}| = \frac{2\sqrt{2ln(2)}}{w_0} \tag{4.3}$$

From the above, we conclude that by minimising phase mismatch, higher resolution can be achieved, as shown in the equation above. This can be attained by increasing the pump beam waist w_0, which will result in an upconverted field with $k_\perp$ vectors parallel to each other. This could have an interesting consequence in entangled upconversion imaging, since uncorrelated photons will produce incoherent radiation with a wide angular spectrum, which should degrade resolution. Nevertheless, imaging with an incoherent or thermal source has proven to improve resolution [117, 118]. Understanding how both characteristics of the incoherent eSFG can affect imaging is not straightforward, and the scope of this investigation was to examine this experimentally.

Generally, PUI is performed using two experimental configurations. In one of the experimental geometries, the object's Fourier plane is imaged on the crystal, with each object detail having its own Point-Spread Function (PSF). With a second lens after the nonlinear crystal, of focal length f_2, the upconverted field is brought back into the spatial domain and imaging is performed. In the second system, an intermediate imaging plane is used, and the object is imaged into the crystal using a separate imaging system. After the crystal, a lens is placed at a distance z_3, and the image of the object will be formed at a distance z_4. The size of the resolvable image for each imaging system is given by:

$$d_{res,1} = \frac{\sqrt{2ln2}\lambda_{up} f_2}{\pi w_0} \quad \text{and} \quad d_{res,2} = \frac{2ln(2)\lambda_{up} z_4}{\pi|\theta_{FWHM}|z_3} \tag{4.4}$$

respectively. As shown in the two equations above, the two systems will produce images with different resolutions. The first system's obtainable resolution is affected by the pump beam waist size, whereas in the second system, resolution is limited by the acceptance angle of the crystal θ_{FWHM}. The system without an intermediate imaging system is more commonly used because it is less sensitive to alignment, while the second system produces higher-resolution images [119].

A theoretical analysis of the upconversion of incoherent radiation has been published by the group of Tidemand-Lichtenberg in Denmark, predicting a $\sqrt{2}$ increase in resolution when an incoherent light is upconverted compared to a coherent laser beam [120]. Here, we wanted to investigate if such an enhancement could be obtained when PDC is upconverted to the visible range, with part of the upconverted field being incoherent. Thus far, the

interaction of the non-entangled photons has been considered an unfavourable contribution to the effect, as it introduces a second-order coefficient and therefore reduces the impact of the observed quantum effect. However, here we investigate the possible benefits of the incoherent component for imaging resolution. But first, the concept of imaging with incoherent radiation is explored, along with the advantages it offers over coherent light imaging.

4.3.1 Imaging with incoherent light sources

Before exploring the benefits of incoherent light imaging, we first need to establish the fundamental tenets of image quality. Image quality is a field of study that has blossomed initially as a means of advancing the film industry by improving lenses and photographic film [121, 122]. Today, with the rise of medical imaging, quantifying image quality is crucial for accurate disease diagnosis [123]. An important parameter of an imaging system is its spatial resolution, which refers to the ability to resolve details of an object. More specifically, resolution is a measure of the minimum spatial separation between two distinct objects before they can be represented as separate details in an image. If we consider the case where imaging of an object with alternating dark and bright lines is performed, then resolution is the ability to distinguish each line apart [124]. Hence, it can be measured as line pairs per mm, and imaging systems that can resolve more pairs in a shorter distance range have a higher resolving power and/or can image at a higher spatial frequency.

A technique for evaluating an imaging system's ability is to measure the Modulation Transfer Function (MTF), which describes how well contrast is transferred at different spatial frequencies. In general, lenses can be thought of as low-pass frequency filters and therefore, a Fourier optics analysis can be performed to describe some of the optical effects in an imaging system. MTF can also be derived from Fourier optics [125, 126]. The derivation begins with the PSF, also known as the impulse response of the imaging system, which represents the minimal size at which an object is blurred due to diffraction [127]. Taking the Fourier transform of the PSF yields the Optical Transfer Function (OTF), which indicates the imaging contrast in the frequency domain. Finally, taking the modulus of that can give the MTF. An imaging system with high resolving power will have an MTF that slowly drops towards zero at a point defined by the imaging system's optics. This point is usually referred to as the cut-off frequency [128]. An example of an MTF for an aberration-free imaging system is shown in Figure 4.4.

While the PSF is a three-dimensional representation of the light source's intensity distribution, the OTF can be represented as a one-dimensional spatial distribution. This is usually derived from the Line-Spread Function (LSF), and experimentally, the mea-

surement of the LSF includes a narrow slit, which should be precisely fabricated and allow enough light to pass through it [129, 130]. A modified measurement that can be performed instead uses a knife-edge, and the resulting distribution is called Edge-Spread Function (ESF) and is the derivative of LSF. Usually, the knife-edge is set in the direction of the beam, either in the vertical or horizontal direction, depending on the desired direction in which the MTF is to be measured. The imaging detector acquires images of the knife edge, which cover half of the beam. It is common to set either the knife edge or the imaging detector at a slight angle to enable sub-pixel resolution measurements. Characterising the resolution of a system using the MTF is a technique adopted in quantum imaging technologies [99, 105, 131] too. Thus, we use it in our experiment as well and follow the technique as described in [129, 132, 133]. Before delving into the experimental endeavours and the results obtained, an investigation of how incoherent radiation alters imaging is provided.

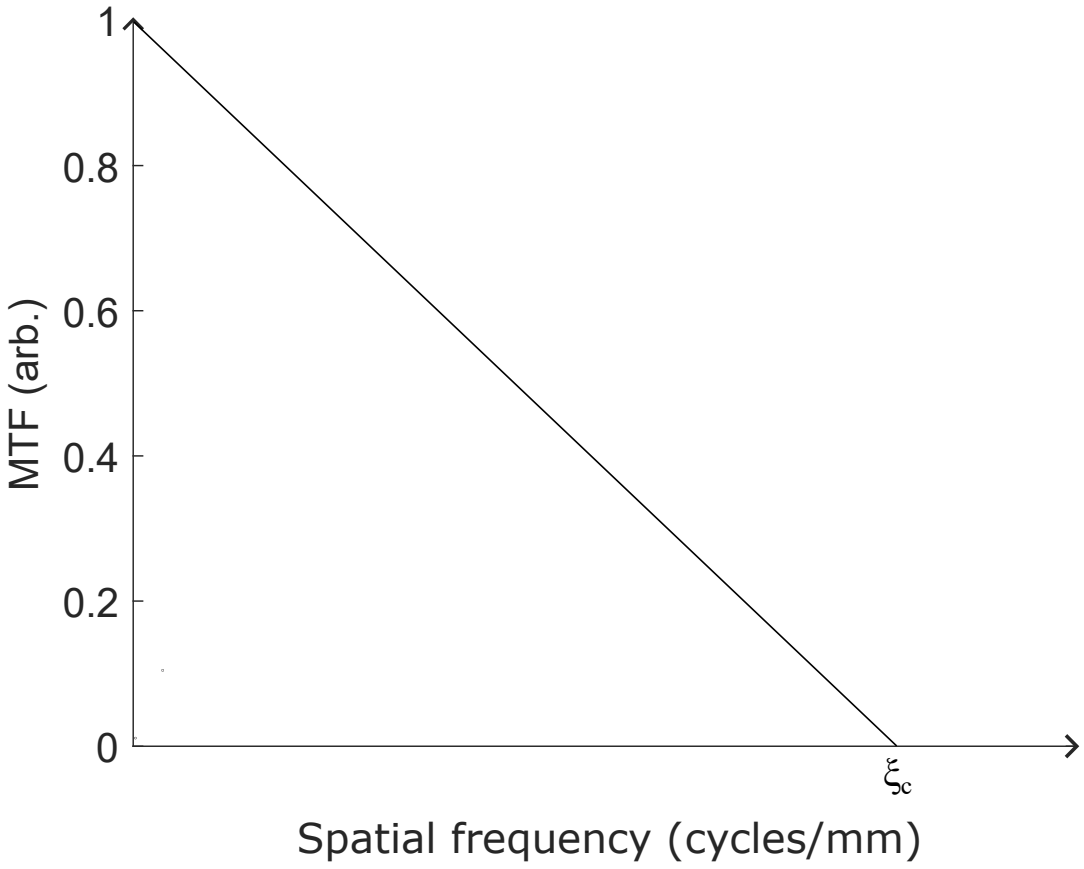

Figure 4.4: **MTF for an aberration-free system** showing that at higher frequencies the image is less resolved until it reaches the cut-off frequency ξ_c, i.e. the resolution limit.

The main difference between coherent and incoherent illumination is the ability or lack thereof to interfere. A source of incoherent radiation lacks phase coherence be-

tween different points in space or time, whereas coherent radiation maintains a consistent phase across them. This leads to differences in the derivation of the Fourier-based image-formation formalism across the two cases.

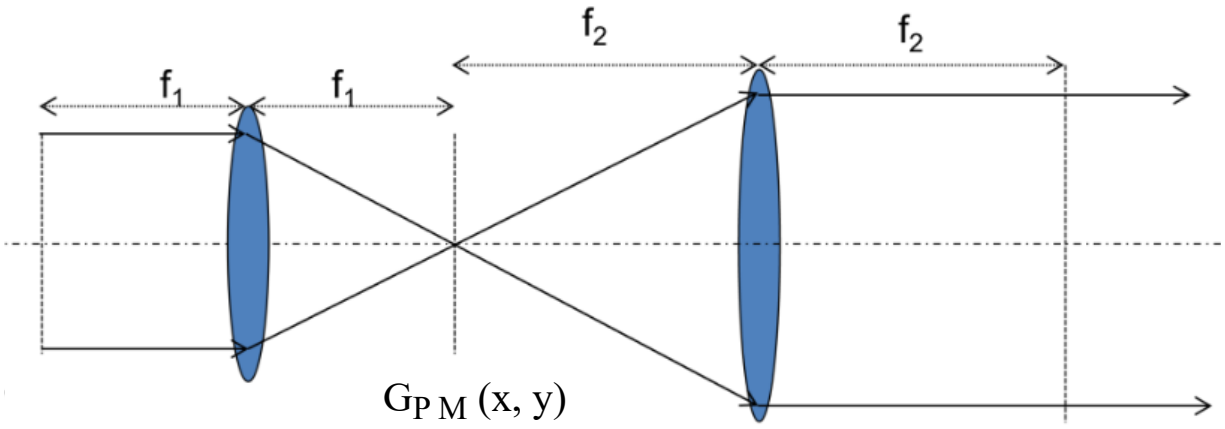

Figure 4.5: **4-f imaging system.** The Fourier plane lies between the two lenses.

We assumed two imaging systems with the same imaging optics, but one is illuminated by coherent light and the other by incoherent light. In general, the image will form at the image plane where the detector is located, as shown in Figure 4.5. In the Fourier plane, we can define the pupil function $G_{PM}(x, y)$, a complex function that describes how the relative phase and amplitude of light waves change as they propagate between the image and focal planes. Mathematically is the same as the Amplitude Transfer Function (ATF), $H(u, v)$, which in turn is the Fourier transform of the amplitude PSF $h(x, y)$ [125]. From the PSF an intensity distribution of the resulting image can be derived, where every point in the object that is being illuminated will be added up as phasors. More specifically, coherent light illuminating different points on the object can interfere; hence, the field strengths A add rather than the intensities:

$$I(x, y) = A \otimes h(x, y) \tag{4.5}$$

In the system where illumination happens with incoherent radiation, the PSF will be equal to the modulus squared of the coherent PSF $h_I(x, y) = |h(x, y)|^2$. Similar to the coherent case, an expression for the image's intensity distribution can be derived. This time, the different illuminated points of the object will add in intensity, with the individual PSFs for each point integrated over the object's response:

$$I(x, y) = I(x, y) \otimes h_I(x, y) = I(x, y) \otimes |h(x, y)|^2 \tag{4.6}$$

with $\otimes$ indicating the convolution between PSF and the object's intensity response [125,

134]. To understand what this means in terms of resolution, the OTF needs to be obtained for each system, a parameter that directly correlates with the MTF. For the system illuminated by coherent radiation, the cut-off frequency is equal to:

$$\xi_{coh} = \frac{NA}{\lambda} \tag{4.7}$$

where NA is the numerical aperture of the system and λ the working wavelength. For incoherent illumination, the OTF will be the normalised autocorrelation function of the ATF, $H(u, v)$, and then the system cut-off frequency is:

$$\xi_{inco} = \frac{2NA}{\lambda} \tag{4.8}$$

concluding that incoherent radiation generally gives better image quality. While a brief mathematical explanation was provided and expressions for the cut-off frequency were obtained for both cases, an intuitive approach might help gain more insight. Because incoherent radiation cannot interfere, speckle and ringing artefacts are absent in images of objects illuminated by incoherent radiation and include more distinct details.

4.4 Entangled Parametric Upconversion Imaging

To implement the PUI technique in our eSFG setup, a mask was created on a microscope slide. To etch the mask on the microscope slide, a CNC milling device was used. Usually, a 1951 USAF resolution test chart is used; however, we opt for a microscope slide instead, as they are significantly thinner and thus introduce less dispersion, which is detrimental to entangled two-photon effects. Additionally, the total diameter of the USAF test target available was larger than our crystal mount could accommodate and could not be properly placed on the crystal's surface. The microscope slide was 0.2 mm thick and cut into a 6 mm diameter circle to fit into the eSFG crystal mount. The mask was mounted at the crystal's centre, forming the pattern "UoG", with the text measuring ∼1 mm in length to cover as much of the near field as possible. Incoming PDC radiation would first interact with the mask, then with the BBO crystal, to produce SFG. Any remaining PDC would be blocked, and the mask would be imaged using the SFG light.A telescope with a magnification of $M = 4$ was built to capture an image of the mask. The telescope was optimised before introducing the mask in front of the crystal by imaging the crystal's surface using eSFG, enabling a proof-of-concept measurement, as the observed features were dust particles on the crystal's front surface. The far-field of the eSFG with the 'shadow' cast by the dust particle is shown in Figure 4.6. The mask was then mounted to the crystal holder, on the side where the PDC would interact with it first, before forming eSFG.

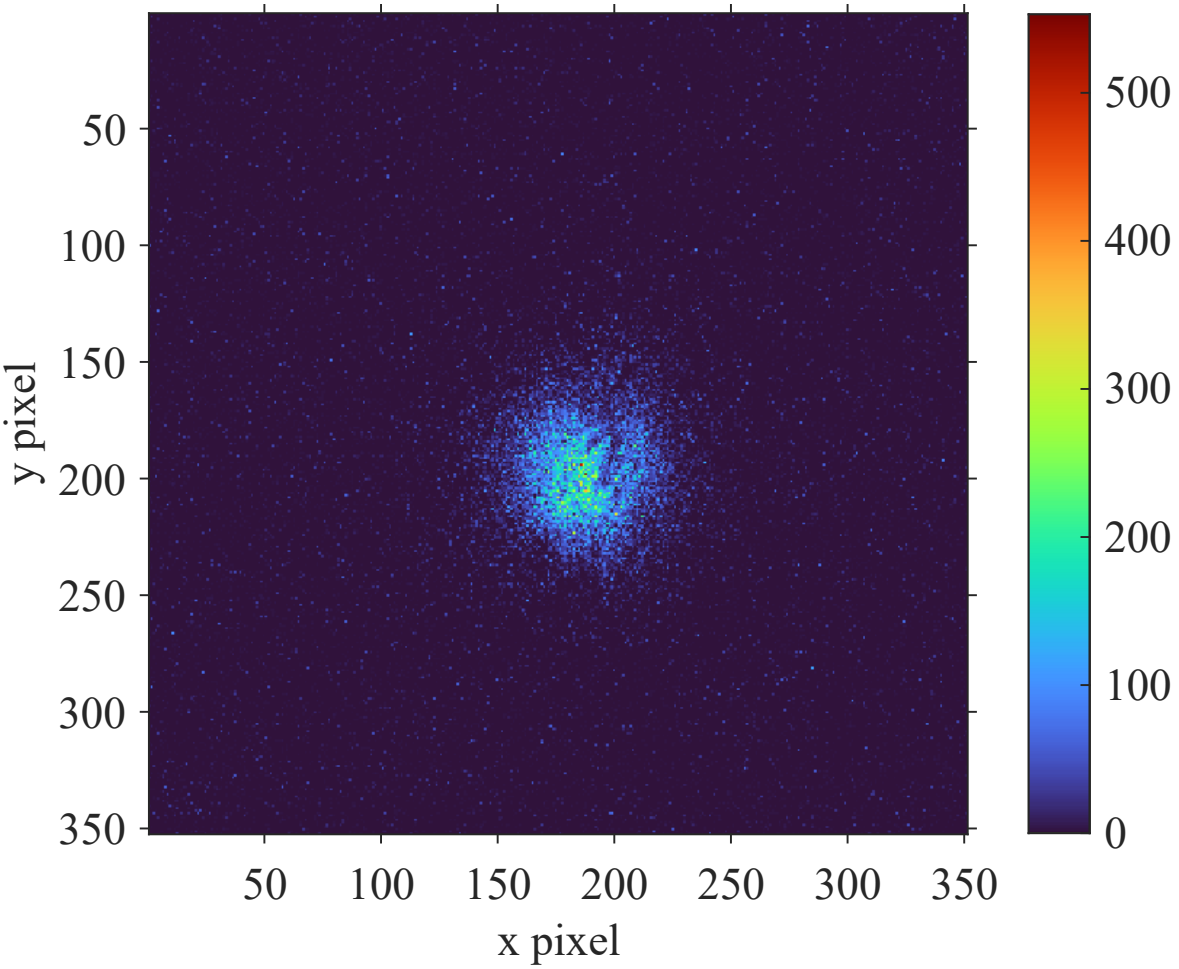

Figure 4.6: **eSFG imaging the crystal details.**This was performed to ensure good alignment of the telescope build using two lenses.

Figure 4.7 A shows the PDC near-field imaged on the eSFG crystal with the mask in front of it, while on 4.7B the upconversion of the entangled radiation is shown. From the image of the eSFG, the presence of aberrations is evident, as the mask appears blurry. A shift in the generation spot of the eSFG is also apparent, as details that the PDC illuminates are not visible with the eSFG. This can be attributed to the effect of the walk-off, which appears in the direction of the phase-matching angle. The fact that the vertical lines of the mask are unaffected by it is evidence that the observed effect can be attributed to walk-off. This was also confirmed by carrying out two separate measurements. The first measurement was performed to eliminate the possibility that the aberrations were caused by tilting of the crystal, which is necessary for achieving phase matching. Therefore, the side of the mask that is closer to the incoming squeezed radiation appears blurred. The mask was rotated 90° and thus all the details of the mask were positioned directly atop the side of the crystal, which was closer to the imaging system. Alas, this didn't eliminate the aberrations, as they reappeared across the horizontal axis of the image again. In the

last test performed, the mask was replaced with a piece of paper in the shape of the letter 'L' to examine whether the horizontal line on the paper would be sharper than the vertical one, or vice versa. Indeed, the vertical line was not aberration-free, and it was concluded that walk-off would have a detrimental effect on imaging details along the phase-matching direction. An example is shown in Appendix A.

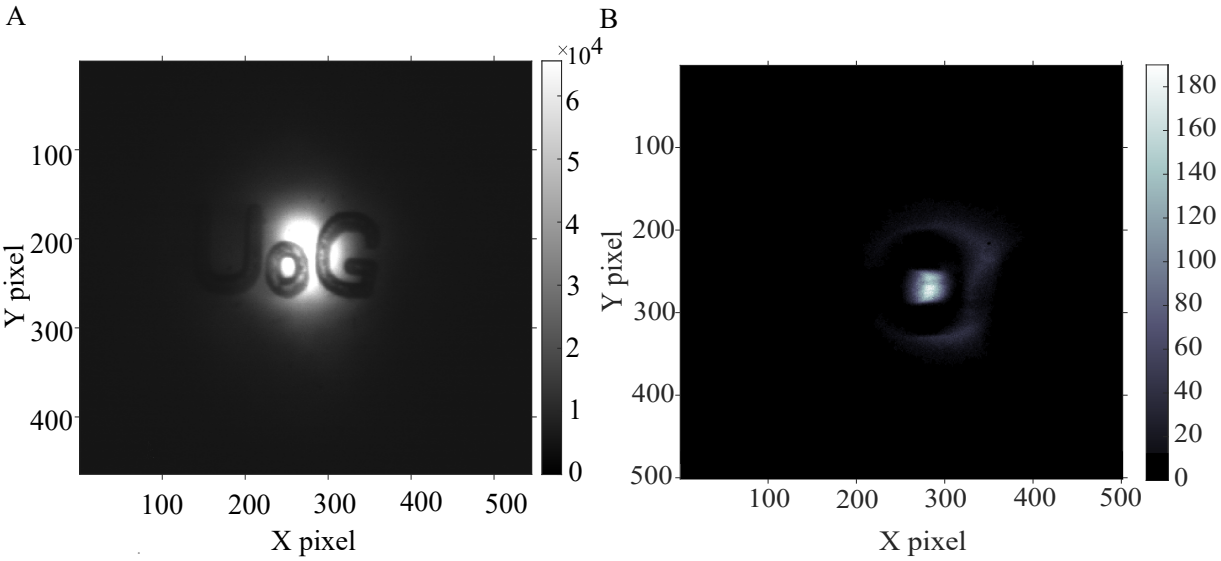

Figure 4.7: **Imaging of mask through eSFG.A** shows the PDC near field on the UoG mask and **B** eSFG far-field imaging the mask. Imaging of the eSFG was performed using a telescope of magnification 4.

Walk-off is a phenomenon that can be intrinsic to nonlinear interactions, as it is a consequence of the birefringence of the nonlinear crystals used. As explained in the introduction, walk-off can be reduced or entirely avoided by changing the nonlinear medium used to produce eSHG. Walk-off in a BBO is typically 5 to 10 times larger than in an LBO, but it offers greater efficiency due to its higher nonlinearity. To eliminate walk-off, crystals that can be non-critically phase-matched are the best option, as non-critical phase-matching is insensitive to spatial walk-off. These crystals are most commonly used in PUI [135, 136], to achieve walk-off-free imaging of objects.

Instead of changing the crystal used for the interaction, we proceeded with the current setup and adjusted the imaging to account for the spatial walk-off effect. To this end, we revert to a more simplified imaging system, one that was inspired by the measurement of the MTF to characterise the resolution of the system. Hence, a knife-edge measurement was performed, and any image analysis was conducted along the vertical axis, where no walk-off is present. Therefore, the object was set along the vertical direction, and any details would be analysed by taking trace lines along the vertical direction. A more thorough explanation is given in the Methods section below.

4.4.1 Apparatus and Measurements

The modified setup to perform the imaging measurements is shown in Figure 4.8. A sharp razor blade was inserted as close to the front crystal surface as practically possible. The razor blade was positioned on a motorised translation stage to adjust its position along the vertical direction, allowing it to be placed precisely at the centre of the PDC beam, as shown in Figure 4.10. After the BBO crystal, a microscope objective with a tube lens was used to image the knife edge with the eSFG radiation. The infinity-corrected microscope objective had a magnification of 10, but the tube lens used had a focal length of 150 mm. The effective focal length of the microscope objective was 1200 mm, and the system's magnification was determined by dividing this by the tube lens' focal length. This resulted in a total magnification factor of M = 8. We chose the lens with this specific focal length to ensure it could be placed exactly one focal length from the crystal; therefore, the objective could be removed to observe the far-field of the eSFG and optimise for phase matching. To complete the imaging system, the EMCCD was placed after the optics.

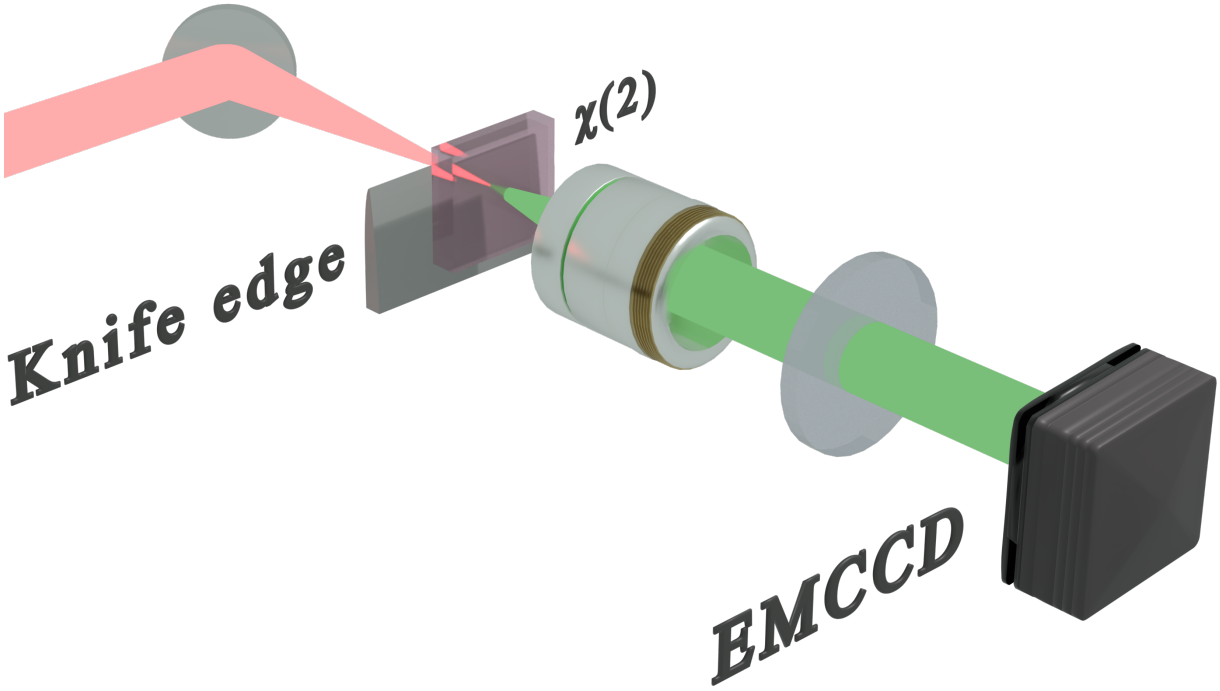

Figure 4.8: **Imaging set up**. A razor blade was inserted in front of the BBO crystal, in the way of the PDC beam. Parametric upconversion imaging is performed, and the edge is imaged through the eSFG.

We aimed to isolate the incoherent contribution from the eSFG by removing its coherent component. Incoherent eSFG is produced when non-correlated photons interact to generate SFG. Unlike correlated signal and idler photons, which are found at opposite sides of the far-field PDC, uncorrelated photons are photons that reside in the far-field of the PDC, but instead of interacting with their symmetric pair, they interact with an

uncorrelated photon. Therefore, by asymmetrically blocking the far field, PDC-correlated photons can be excluded from the interaction that happens at the BBO crystal, since none of them will arrive at the nonlinear medium, and the coherent component won't occur. This will result in purely incoherent eSFG radiation. To achieve this, a mask was designed and 3D printed to be placed at the far field of the SV, as shown in Figure 4.9 A ii). Of course, the mask would affect the total power of the PDC incident on the BBO crystal, where eSFG would occur. Therefore, a second mask was inserted at the far field, allowing the correlated photons to pass through and enabling the production of coherent eSFG. This is shown in Figure 4.9 A ii).

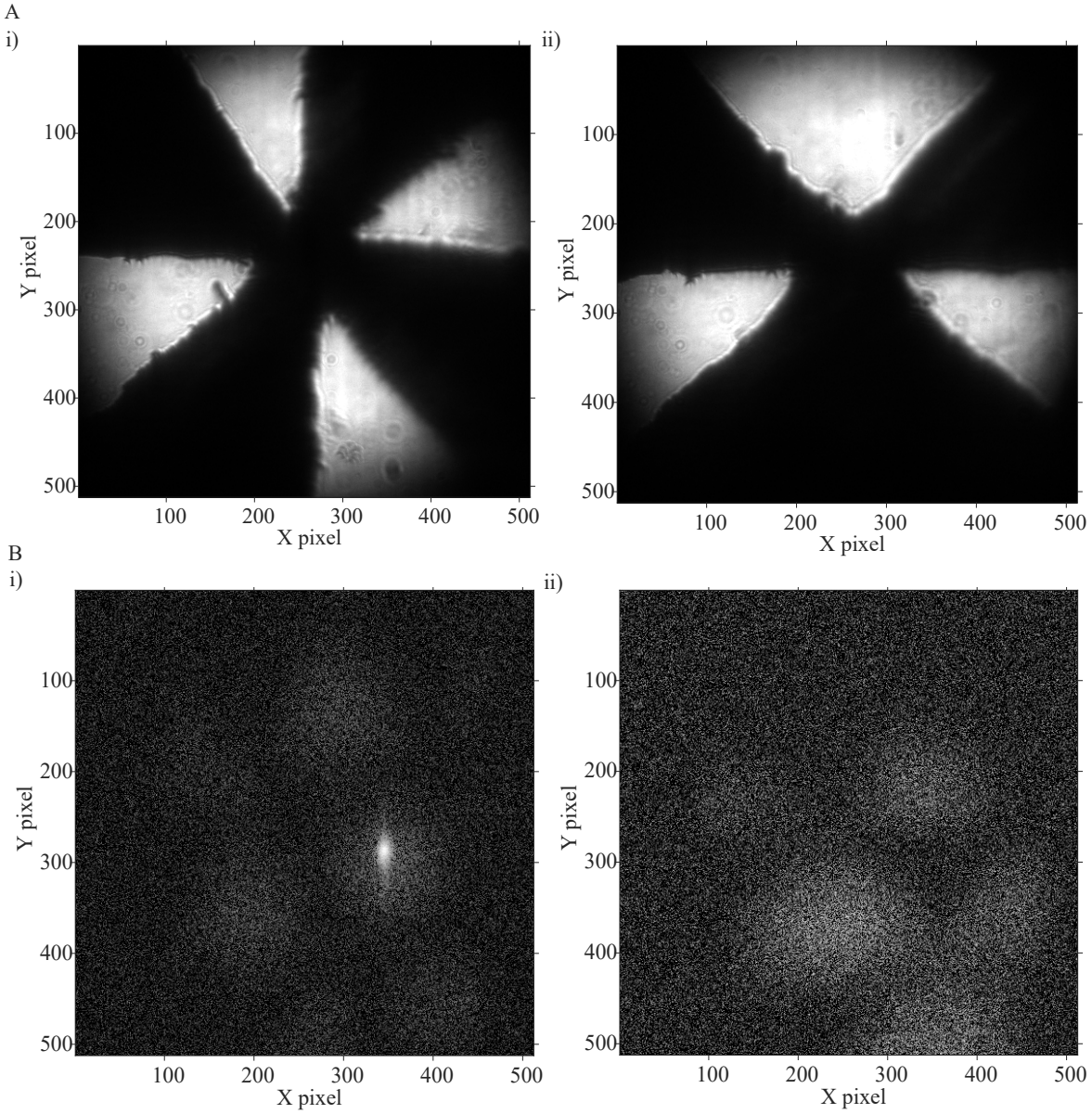

Figure 4.9: **Symmetric and asymmetric losses at the far-field of the PDC and the resulting eSFG far-field.** A i) shows the symmetric losses added to the far-field of the PDC, while A ii) shows the asymmetric losses, to block the interaction of correlated photons. The resulting incoherent eSFG radiation is shown in B ii).

The mask would introduce symmetric losses into the entangled state, but the total transmission would equal that of the asymmetric first mask. Both masks were mounted on a motorised filter wheel, for easy switching between them and were placed in the far field. The motorised filter wheel also allowed us to switch to one of its empty filter positions to check the eSFG response when no losses are present.

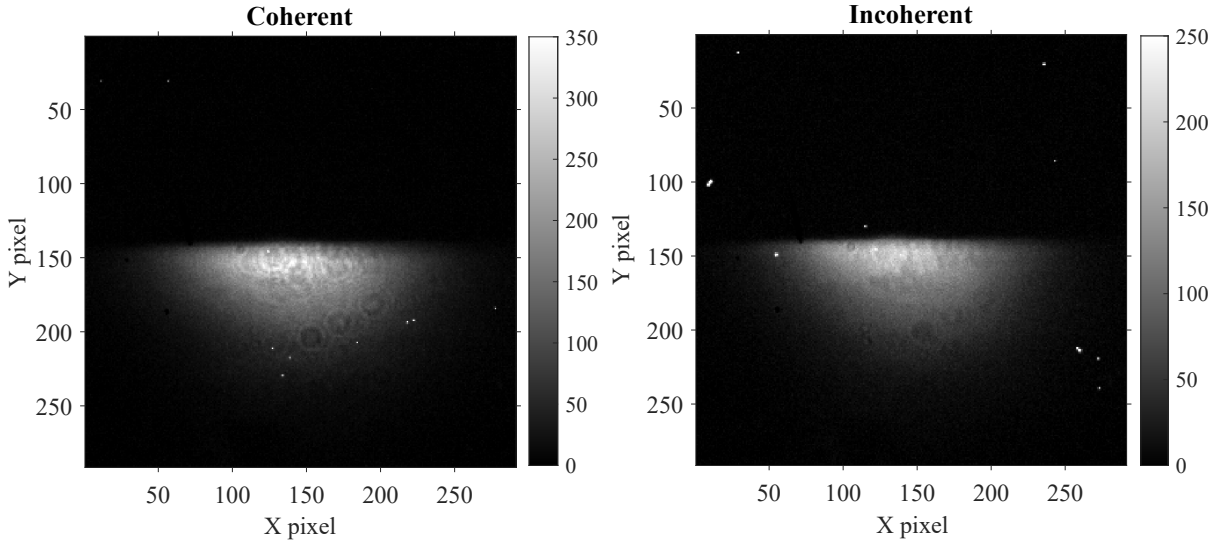

Figure 4.10: **Knife edge imaged with the coherent and the incoherent component of eSFG.**

The resolution measurements were performed following the theory described in Section 4.3.1 and the methods in [129, 133]. Information about the resolution could be retrieved from the MTF; therefore, the knife-edge method was implemented. Images of the knife edge were recorded using the EMCCD, as shown in Figure 4.10, and the results presented here are from pictures taken with a 30-minute acquisition time. Measurements with the symmetric and asymmetric masks were performed consecutively, with the phase-matching image checked at the beginning of the experiment. This was an essential step because our imaging system captures the near field of the eSFG, which corresponds to the birth zone of the radiation. Therefore, coherent and incoherent components appeared together in one bright spot, and no distinction can be made between the two elements of the radiation. The difference can be seen only in the far field of the radiation when the objective is removed. Once the check was completed, a background image was captured. Similar to the measurements described in Chapter 3, the crystal would be rotated 90 ° to capture the background.

When the knife edge covers the eSFG radiation, the total transmission is zero, while the rest of the beam being imaged has a transmission of one. Of course, this is only true

for a perfect edge with a step function describing the transmission like:

$$T(x) = \begin{cases} 1 & \text{for } x \geq 0 \\ 0 & \text{for } x \leq 0 \end{cases} \tag{4.9}$$

In reality, however, the edge is blurred by the PSF, with the image of the razor blade being described by the ESF. A line trace is taken between the two regions of the image, and the intensity of each pixel is obtained. The intensity response is fitted using the Gaussian error function $erf(z)$. Fitting is performed to increase the SNR. From this, the ESF is obtained. The results presented in this thesis are an average of three line traces across the knife edge and the dark region of the image. For both coherent and incoherent pictures, which are identical, the ESF was drawn across the same pixel positions, and then the three ESF were averaged between them. As mentioned earlier, the LSF can be obtained by calculating the gradient of the ESF.

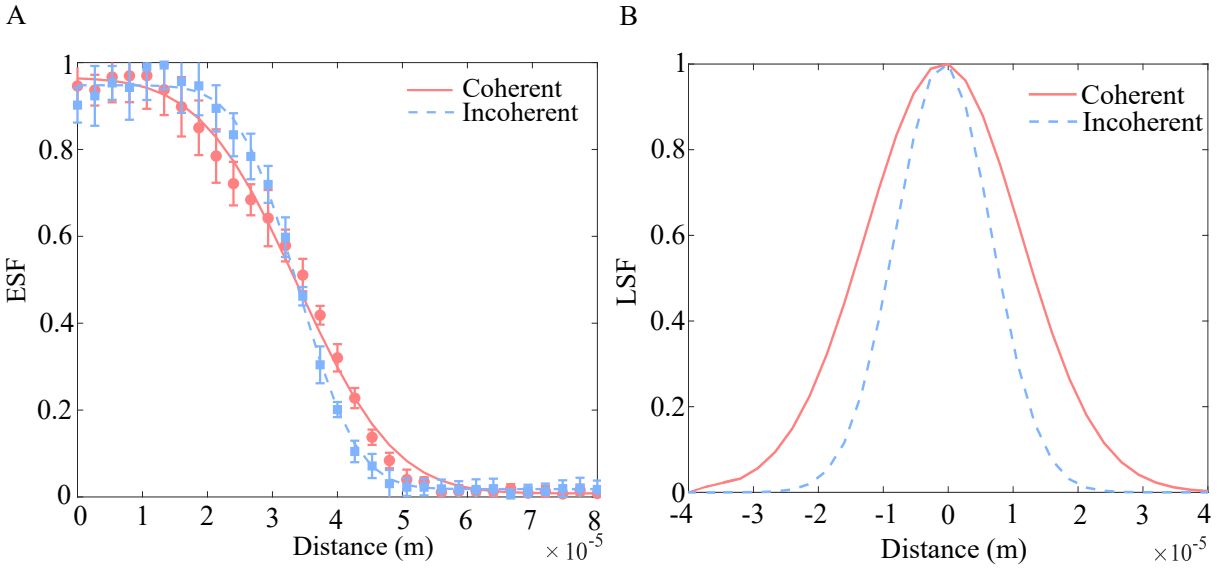

Figure 4.11: **Edge spread function and Line spread function of the coherent and incoherent components.** A shows the ESF of both components plotted together, and their corresponding fitted $erf(z)$ functions. The gradients of the fits are shown in B, with the incoherent LSF(blue line) being narrower, indicating a larger change of the ESF.

As seen from Figure 4.11 B), a clear difference between the LSF of the incoherent (blue dashed line) and the coherent (orange line) is visible. Imaging with an incoherent light source results in a narrower LSF, which is the derivative of the ESF. The narrower response indicates a sharper change in the LSF, and it is closer to the derivative of an ideal step function, which is the Dirac delta function. Therefore, a razor blade imaged by a super-resolving imaging system has an LSF that the Dirac delta function can describe mathematically. However, in our case, the LSF is a convolution of the razor blade response with the PSF [137]. Since the delta function can be approximated as the limit of a Gaussian

that has a width that approaches zero:

$$\delta(x) = \lim_{\gamma \to 0} \frac{1}{\gamma\sqrt{2\pi}} e^{\frac{x^2}{2\gamma}} \tag{4.10}$$

where γ is the width of the Gaussian [138], the obtained LSF can be fitted using a Gaussian. This was done as a means of quantifying the amount of enhancement seen from the incoherent component. Fitting the LSF as a Gaussian. From the fitting performed, the FWHM of the coherent component was found equal to 2.797×10^{-5}m while the FWHM of the incoherent component was equal to 8.709×10^{-6} m. These values indicate a difference of more than 3 times between the incoherent LSF and the coherent one.

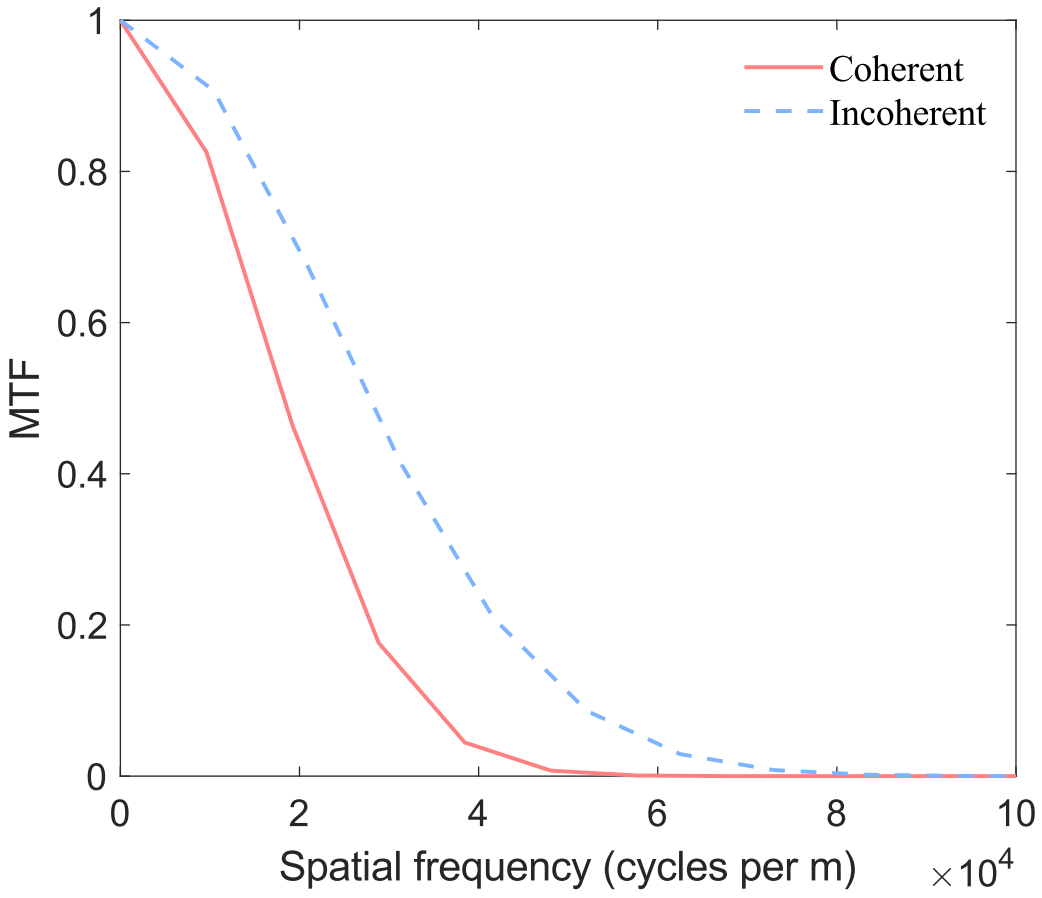

Figure 4.12: **Modulation transfer function of coherent and incoherent component.** The above shows the incoherent component (in blue dashed line) falling gradually until it reaches the cut-off frequency at 9.5×10^4 cycles per m. The coherent component's MTF falls much more abruptly at a cut-off frequency of 6×10^4 cycles per m. The above confirms the increased resolution when imaging is performed with incoherent illumination.

To obtain the MTF, the Fast Fourier Transform (FFT) was conducted over a 'window' to avoid spectral leakage. This technique is known as 'windowing,' and it is used to prevent discontinuities in the signal [139], since FFT assumes that the input signal is a

periodic function. This was obtained by performing a 1D Fourier Transform on both the coherent and incoherent contributions' LSF. To calculate the spatial frequency that our imaging system can resolve, the frequency index of the FFT is divided by the measured distance in the image. This is limited by the spacing between each point of the line traces, which is constrained by the pixel size and pixel separation. The measured separation is 2.67 µm, while the pixels of the EMCCD have a size of 16 µm. Of course, the magnification of our system can account for the difference in the two values.

The results are shown in Figure 4.12. As can be seen, the MTF obtained for the incoherent component (dashed blue line) falls more slowly than that of the coherent component (orange solid line), indicating that imaging with an incoherent component can result in higher-resolution images. Another important observation is the different cut-off frequencies that the light sources have. While the coherent component's cut-off frequency is 50×10^3 cycles/ m, the incoherent component has a cut-off frequency equal to 95×10^3 cycles/m. The cut-off frequency of the latter is almost twice that of the former, indicating that imaging with an incoherent source can sometimes resolve periodic features of an object with twice as small a period. Apart from the observed enhancement in resolution, there are other differences between the imaging of coherent and incoherent light sources. These will be discussed in the following section.

4.4.2 Other effects

Before performing any analysis on the identical razor blade images obtained for the two different masks placed in the far field of the PDC, an apparent difference was observed between the two images. More specifically, in Figure 4.10, a difference between the imaging of the edge of the razor blade can be seen, with the incoherent light having a more uniform distribution across the edge, while the coherent radiation appears to form a second edge. A magnified version of Figure 4.10 is presented below, in Figure 4.13. Initially, the observed effect was attributed to the correlated photons incident on the razor blade. The losses introduced by the edge on the correlated photons would affect the produced coherent eSFG significantly more than the incoherent component. Therefore, a second edge forms below the true edge imaged. But further investigation revealed that's not the case.

The observed effect is called 'ringing', and it is present whenever an edge is imaged using coherent radiation [140]. A more prominent example of it is given in Figure 4.14 included in the 'Introduction to Fourier Optics' book by Goodman. The effect can be thought of as equivalent to the Gibbs phenomenon, in which a sharp discontinuity in a signal can result in 'overshooting'. More specifically, the observed effect can be explained by considering the transfer function of a coherently illuminated imaging system that images

a sharp edge. The edge will have a strong high-frequency component, and therefore, the diffraction angle will be large.

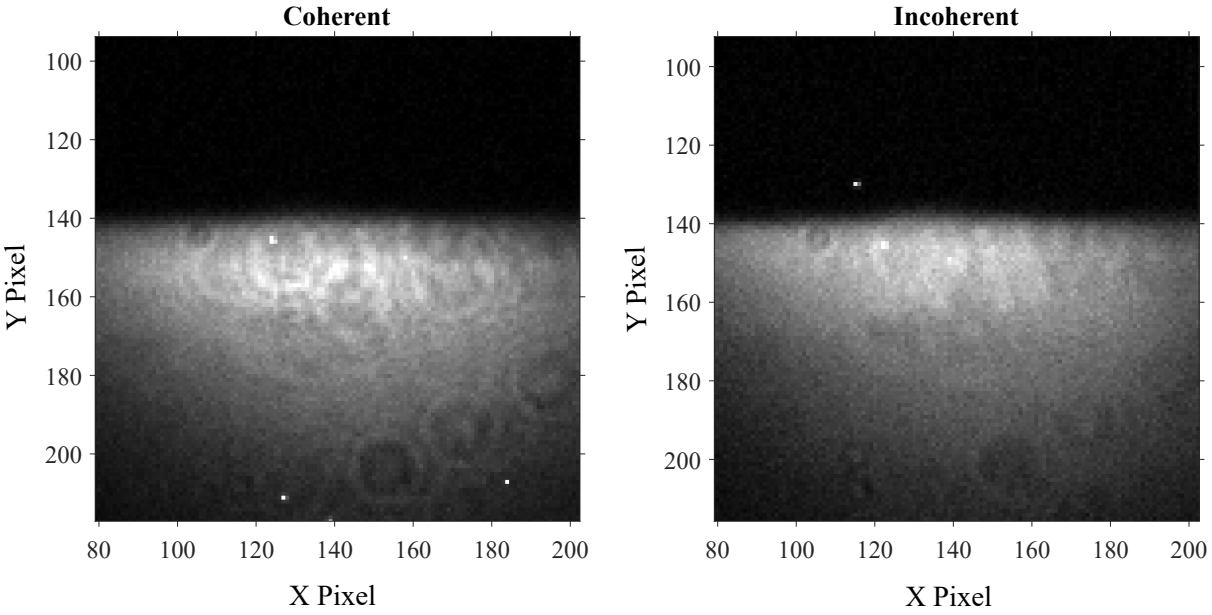

Figure 4.13: **Magnified version of Figure 4.10.** Magnification was performed in post-processing to highlight the effect of ringing.

This will also result in an effect called "edge shifting". When the ESF of incoherent and coherent radiation is plotted alongside the ideal ESF of a razor edge, which is described by an edge function, it can be concluded that the best at predicting the position of the edge are systems that are illuminated by incoherent radiation. This is because the asymptotic of the incoherent radiation ESF meets the edge at exactly one-half of its intensity. In contrast, the asymptotic of the coherent radiation ESF will only meet the step function at 1/4 of its intensity [140, 141].

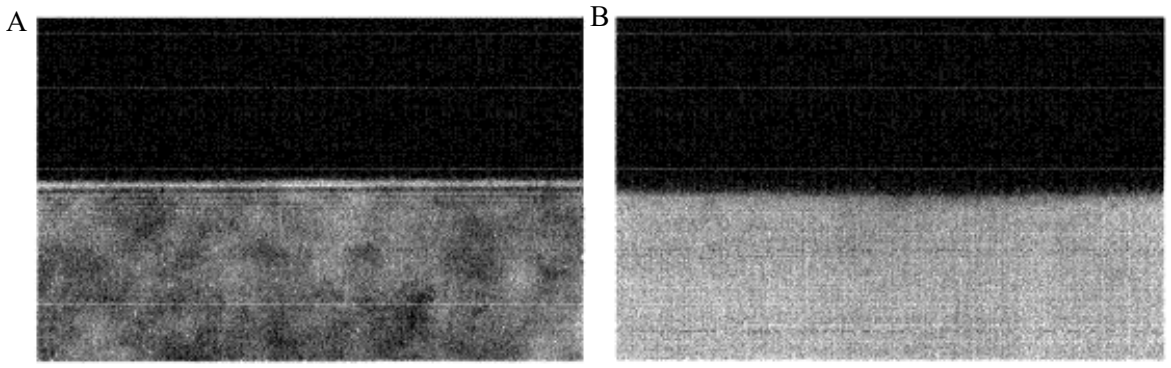

Figure 4.14: **Razor blade imaged through coherent and incoherent illumination** The effect of ringing is shown in A when the edge is illuminated by coherent radiation. The effect is absent when the edge is imaged with incoherent light. The above has been modified from [125].

4.5 Conclusion

To my knowledge, this is the first work to study the impact of the nature of the photons on entangled two-photon absorption effects on imaging. Previous research done on the effects has focused on the linear scaling that can be observed in the nonlinear phenomena when pumped with entangled photons. Here, we further examine the process by focusing on imaging.

While the excitation of fluorophores with quantum radiation and the imaging of their emitted radiation have been achieved previously, that research focused on the number of photons produced by the fluorophores. Here, we examine how the coherent contribution of the eSFG compares to the incoherent contribution in terms of imaging resolution. The effects of coherent and incoherent illumination on imaging resolution were investigated by measuring the MTF. This was achieved by implementing a Parametric Upconversion Imaging technique, in which a sharp razor blade was introduced at the PDC, with imaging performed on the eSFG side.

Our results showed an increase in the cut-off frequency when the object was imaged using the incoherent component of the eSFG, compared to that resolvable by the coherent component. In addition, the MTF of the incoherent radiation showed a higher response than that of the coherent radiation, indicating its ability to resolve images more effectively at the same spatial frequency. While these results are valid, further post-processing can be conducted to improve the fit of the data to the ERF equation. More specifically, there is some trouble fitting the ERF to the lower frequencies of the LSF. This can be improved by performing Gaussian interpolation to account for the knife-edge blocking of the Gaussian PDC beam. Further experimental measurements are needed to understand the phenomena seen. A significant question is the mode and entanglement area, and how they are affected by the introduction of the knife edge in the PDC beam path. Such a check can be performed by moving the razor blade after the BBO crystal where eSFG occurs and repeating the MTF measurements. Lastly, to complete the work on imaging, the results presented here must be compared with the classical form of the quantum experiment. Classical SFG is purely coherent. This raises the question: Does the incoherent component of the eSFG enhance the resolution of such imaging experiments, or can classical SFG still produce better-resolution images? Further discussion of future work for this will be presented in the Conclusion chapter.

CHAPTER 5

Propagation of entangled photons through nested antiresonant nodeless hollow-core optical fiber

Alongside my main PhD project, I also led an experiment with significant potential for quantum communications. While in the main body of this thesis, I focused on entangled two-photon processes, I wanted to include a summary of the work done with hollow-core fibers, a promising platform for low-loss communication.

5.1 Introduction

Alternative communication platforms to meet the ever-increasing communication demands and overcome the current "capacity crunch" have been under development in recent years [142]. One such technology is Hollow Core Fibers (HCF), which, in contrast to conventional glass optical fibers, allow for waveguiding to occur in air or other gases [143, 144]. Hence, the propagation of light can happen with lower fibre latencies and lower non-linearities than conventional glass fibres [145, 146]. This, along with HCF's large bandwidth, which enables the confinement and propagation of broadband radiation, makes it a promising alternative for overcoming the difficulties current communication technologies face.

One of the newly emerging HCF technologies, Nested Antiresonant Nodeless Fiber (NANF), demonstrates a significant reduction in confinement losses. More specifically, NANFs are a refinement of hollow core anti-resonant fibers, with improved losses and exceptional polarisation purity [147, 148]. As seen in Figure 5.1 A, they can consist of a hollow core surrounded by six nested non-touching parallel tubes made from silica, but their geometry can be varied to meet different demands. In the C and L telecommunication

bands, NANFs have achieved an attenuation of 0.28±0.04 dB/km and, more recently, exceptional polarisation purity of up to -70 dB/km has been reported at 1550 nm [147, 149]. This showed the potential for achieving polarisation-encoded communication with an increased secure key rate and since then it has been experimentally demonstrated with a 7.7 km-long HCF at telecom wavelengths [150].

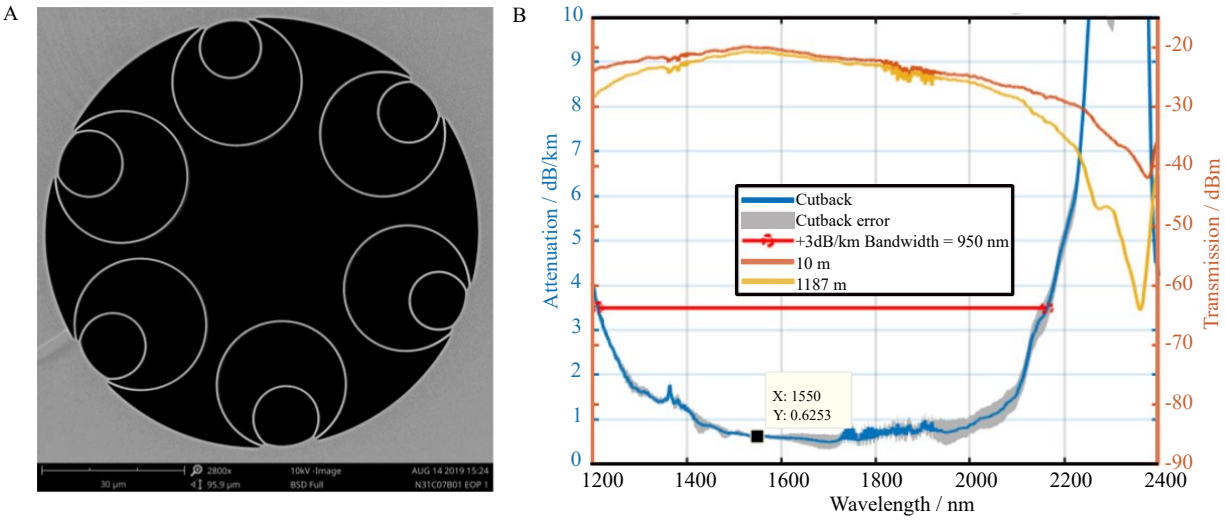

Figure 5.1: **NANF manufacturer characteristics.** In **A**, a picture of the cross-section of the fiber is shown, acquired using a scanning electron microscope. In **B**, the attenuation and transmission loss through the fiber are given as measured by the manufacturer. The fiber has a minimal loss value of 0.495 dB/km at a wavelength of 1705 nm, and 0.6253 dB/km at 1550 nm.

Another advantage of HCF is their exceptional operation at the 2 µm spectral region. HCF has a minimum attenuation of 0.85 dB/km at 2 µm and can transmit light with a 200 nm bandwidth at below 2 dB/km attenuation [151]. Operating further into the infrared region, at 2 µm, could offer a potential solution to the current capacity issues in communications, as other technologies already favour this spectral region. For example, integrated photonics are expanding into this region, with silicon-germanium waveguides transmitting data at speeds up to 10 Gbytes/s over a propagation length of nearly a centimetre [152]. Silicon could offer a potential infrastructure for future communication systems at 2µm since absorption and non-linearities are reduced. This has already caught the attention of scientists with developments in integrated quantum photonics underway [153, 154].

Matteo Clerici's group at Glasgow has also performed previous work at the 2µm region [155]. Specifically, the characterisation of indistinguishable photon pairs and polarisation entanglement at 2.1 µm was experimentally investigated. A pulse laser beam interacted with a 1-mm-long, periodically poled, magnesium-doped lithium niobate crystal (PPLN) to produce signal and idler photons centred around 2090 nm. Signal and idler

photons were spatially separated and coupled into two separate Ge-doped silica-core optical fibers and detected using superconducting Nanowire Single-photon Detectors (SNSPD) connected to time-tagging electronics. A tunable delay was added in front of one of the fibers to adjust the temporal arrival of the photons, and a coincidence-to-accidental ratio (CAR) measurement was performed. A maximum CAR of 180 ±50 at ≃5 mW of input pump power was measured, and, as expected, it decreased with increasing input pump power. In pulse SPDC, photon pairs are generated by individual pulses of the input laser beam, and a CAR measurement can indicate the ratio of coincidences from a single pulse to the average coincidences from two different pulses. Another measurement was performed to investigate the indistinguishability of the photon pairs. More specifically, quantum interference was observed using a polarisation-maintaining, fiber-based 50:50 beam splitter with two output ports. As predicted by the Hong–Ou–Mandel (HOM) effect, when the photons are indistinguishable, and their optical paths overlap, detection occurs at only one of the beam splitter's output ports. To ensure the effect was observed, a second delay was introduced, and the expected HOM dip became visible. Lastly, a Clauser-Horne-Shimony-Holt (CHSH)–Bell test was performed to ensure entanglement between signal and idler photons. With the results opening the way for quantum communication in the 2.1 µm region, we decided to investigate this possibility with HCF.

5.2 Methods

Work on HCF began with characterising its performance. The 1-km-long fiber, with 37 µm core diameter, was coiled into a spool. To optimise the coupling into the fiber we follow the suggestions from [156]. Their theoretical investigations showed that a coupling efficiency of up to 98% can be achieved when the laser beam waist size is 70%. Therefore, optics were selected to reduce the characterisation laser beam size to the desired value. Lastly, to maximise coupling, the input of the NANF was set on a 6-Axis NanoMax stage with stepper motor actuators to adjust the position and tilt of the fiber.

The coupling losses were first measured by using the cutback method. More specifically, this method consists of comparing the transmission of the fiber of different lengths. Therefore, a transmission measurement was performed along the full 1-km length of the fiber. Without unmounting the fiber from the 6-Axis NanoMax coupling stage, the fiber was cleaved to a shorter length of 1 m. This method enabled us to measure fiber characteristics without introducing errors due to variations in the launch conditions.

Next, the attenuation losses were considered in both the 1560 nm and 2 µm regions. The estimated attenuation values were 0.52 dB/km at 1560 nm and 0.95 dB/km at 2000

nm, accounting for coupling losses. While the measured attenuation at 2 µm is close to the record attenuation value of 0.85 dB/km it is also important to state that at 2 µm the HCF performs better than conventional silica-fused fibers and the reported measured attenuation loss is an improvement when compared to hollow-core photonic bandgap fibers (HC-PBGFs) with reported attenuation of 2.5 dB/km at the same wavelength [157]. To complete the above measurements, Continuous wave (CW) fiber laser sources at 1560 nm and 2 µm wavelengths were used.

Another critical step in the characterisation process was the evaluation of the Polarisation extinction ratio (PER). The PER is an important factor of systems that rely on high polarisation purity, as it is a measure of how well a fiber maintains the polarisation state of transmitted photons. An InGaAsP tunable laser and polarisation optics were used to measure the PER of the hollow-core fiber across the C band. The polarisation of the propagated laser light was set using a Glan-Taylor polariser, a half-wave plate, and a thin film polariser at the input of the fiber. To test the PER for a set of input polarisation angles, the polarisers were aligned with the horizontal axis of polarisation, then fixed in place, while the half-wave plate was rotated to select the desired polarisation. The reverse geometry of the polarisation optics was repeated at the output of the fiber, and the output light was focused on an InGaAs amplified detector connected to a lock-in amplifier for measurement.

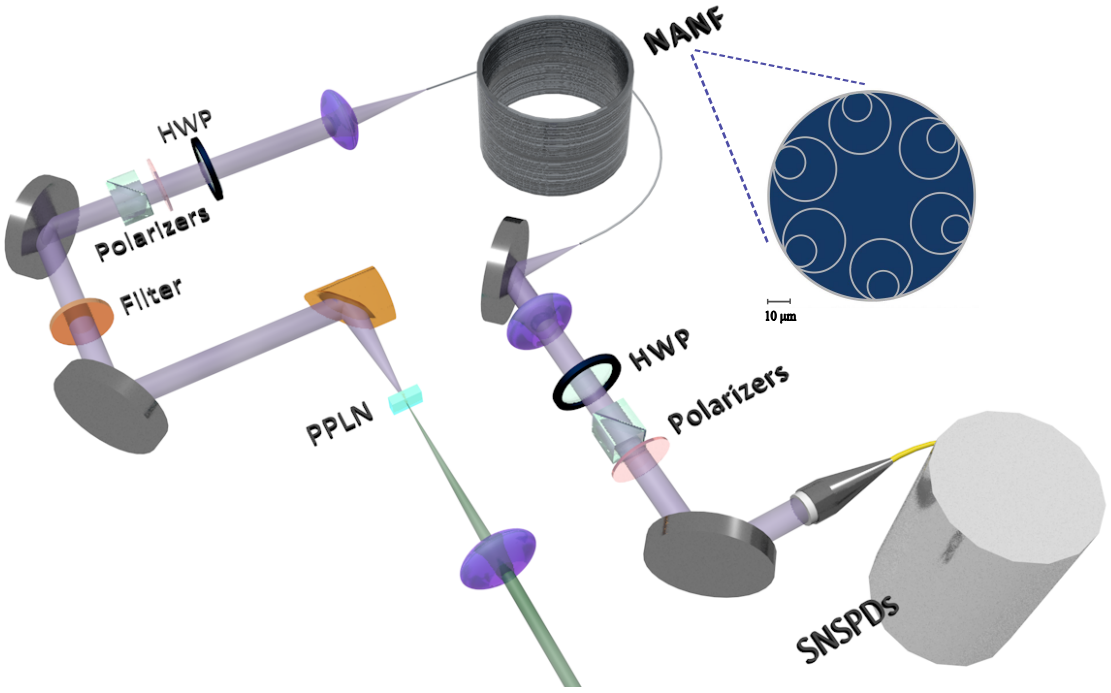

Figure 5.2: **Setup for measuring the PER and dispersion of the photon pairs propagating through the NANF** The laser pulse with duration 127 fs is acting as a pump to produce photon pairs centred around 2,01 µm through the process of PDC. The inset shows the cross-sectional structure of the fiber.

A similar setup was used to measure the PER of the fiber when a squeezed vacuum state was propagated through, shown in Figure 5.2. Like the previous work presented in this thesis, the squeezed vacuum was generated through the process of PDC when the pulse of a ytterbium-based ultrashort fiber laser with an average power of up to 2.5 W, repetition rate of 80 MHz and carrier wavelength of 1.045 µm interacted with a magnesium-doped lithium niobate crystal (MgO-PPLN) through type-0 interaction. Unlike in type-I interaction, where the generated signal and idler photons are orthogonal to the pump beam, in type-0 interaction the signal and idler photons share the same polarisation as the pump beam. The periodically poled crystals enable a technique known as quasi-phase matching; a thorough explanation is provided in Appendix B. After the generation crystal, a long-pass antireflection-coated germanium filter was used to block out any remaining pump beam, as well as a 55-nm bandpass filter centred around 2 µm to select most of the entangled radiation.

A range of optics was tested to collimate the down-converted light, which was emitted over a broad angular spectrum, before a 50-mm-focal-length, gold-coated, off-axis parabolic mirror was selected. To efficiently couple the photon pairs into the fiber, their beam size must be known in order to select appropriate optics that focus them to the desired spot size. Due to the unavailability of cameras in the 2 µm region, a knife-edge measurement was performed to determine the beam size. More specifically, an opaque edge was attached to a translation stage and was translated transversely across the beam path. The transmitted optical power is recorded as a function of the knife-edge position using the InGaAs-amplified detector. As the knife edge progressively blocks the beam, the detected power follows the integral of the beam's transverse intensity profile. When a Gaussian beam profile is assumed, the measured power-versus-position curve corresponds to an Error function (ERF). Therefore, the data were fitted using the ERF curve, and the beam radius was extracted. The data and the fitting values are shown in Appendix B. The estimated beam size of the squeezed vacuum was 6 mm (1/e2), and therefore, a 40 mm focal length CaF2 lens was used to couple the photon pairs into the hollow-core fiber. A duplicate of the same lens was used at the output of the fiber to collimate the radiation before passing through the polarisation optics and finally to the detector. This time, SNSPD were used for the PER and dispersion characteristics of the fiber. To this end, the squeezed vacuum was coupled to a 15-m-long single-mode fiber (SM2000), which was routed into the SNSPD cryostat.

In the next section, the results of these measurements are presented, beginning with those obtained using the CW lasers and then proceeding to the results from the propagation of squeezed vacuum. Apart from the PER measurements, the dispersion of the fiber experienced by the photon pairs was also investigated.

5.3 Results

The calculated PER results measured with the CW lasers are shown in Figure 5.3. More specifically, the PER is defined as:

$$\mathrm{PER} = 10\log_{10}\frac{\mathrm{P_p}}{\mathrm{P_0}} \tag{5.1}$$

where $\mathrm{P_p}$ and $\mathrm{P_0}$ correspond to the maximum and minimum measured signal from the lock-in, respectively. For each input polarisation, the output half-wave plate was rotated from 0° to 90°. As expected, the resulting data followed the $\cos^2(\theta)$ function, and those are shown in Appendix B. From those data, the PER is calculated and plotted in Figure 5.3. A code was written to control the half-wave plate mounted on a motorised stage, the tunable laser, and the lock-in amplifier to acquire the measured data. The laser sources were modulated using mechanical choppers at a frequency of 877 Hz. Different input polarisation angles across the 1518-1630 nm range were investigated by changing the half-wave plate angle. For each measurement, the lock-in was recording the output voltage of the photodetector, with each measurement averaged over a 3-second interval.

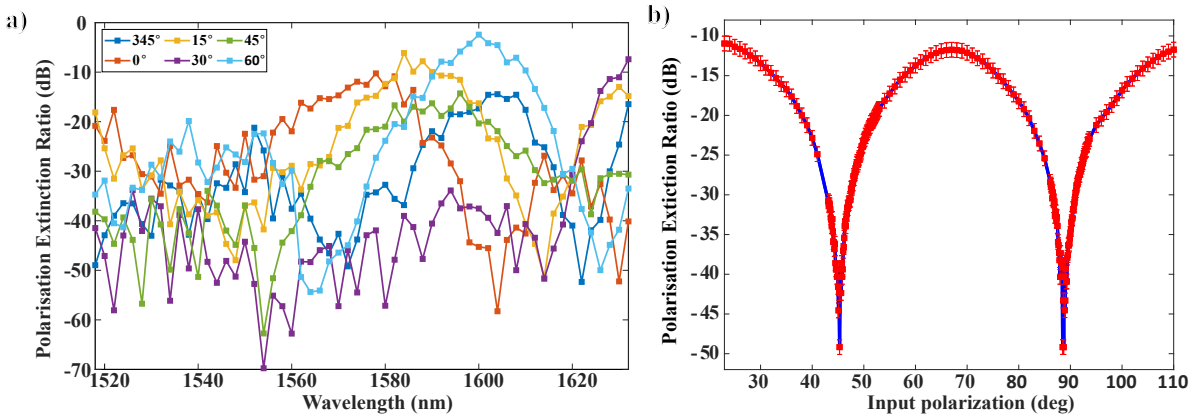

Figure 5.3: **Measured PER for C-band a) and 2 µm b) CW sources propagating through the NANF.** In a) the inset shows the angle of the input half-wave plate and the PER for each input polarisation is shown, with the best PER being achieved when the input polarisation was set at 60° at the wavelength of 1554 nm. In b) the PER measured with the 2 µm laser is plotted.

From the figure above, it is evident that the best PER value measured of −70 dB was achieved when the input half-wave plate was rotated at 30°, achieving an input polarisation angle of 60° to the horizontal (aligning with the plane of the fiber's coil). This value aligns closely with the reported values in the literature for NANF fibers designed for the 1550 nm waveband. Averaging all the PER values between them, a PER of −58 dB was achieved

across the C band, but quite a variability in PER is observed. This could be caused by the principal axis of the fiber shifting with wavelength and may not be perfectly aligned along the entire spool length. This can lead to variations in birefringence and, consequently, affect the PER.

The PER for the 2 µm wavelength is shown in Figure 5.3 b), with a recorded PER value of -50 dB for the horizontal and vertical input polarisations. It is important to note that polarisation optics can also limit PER if not carefully selected. For this reason, a similar measurement was performed without the fiber in place. This approach enabled estimation of the optics' PER, ensuring that it did not affect the measured PER of the fiber. In the 2 µm waveband, the PER of the polarisation optics without the NANF is approximately 55 dB, whereas in the telecom C band, the PER is approximately 80 dB. In the 2 µm case, the total PER of the fiber was close to the limit of the polarisation optics, and when photons from the C band spectral region propagated through the fiber the PER of the optics didn't affect our measurement.

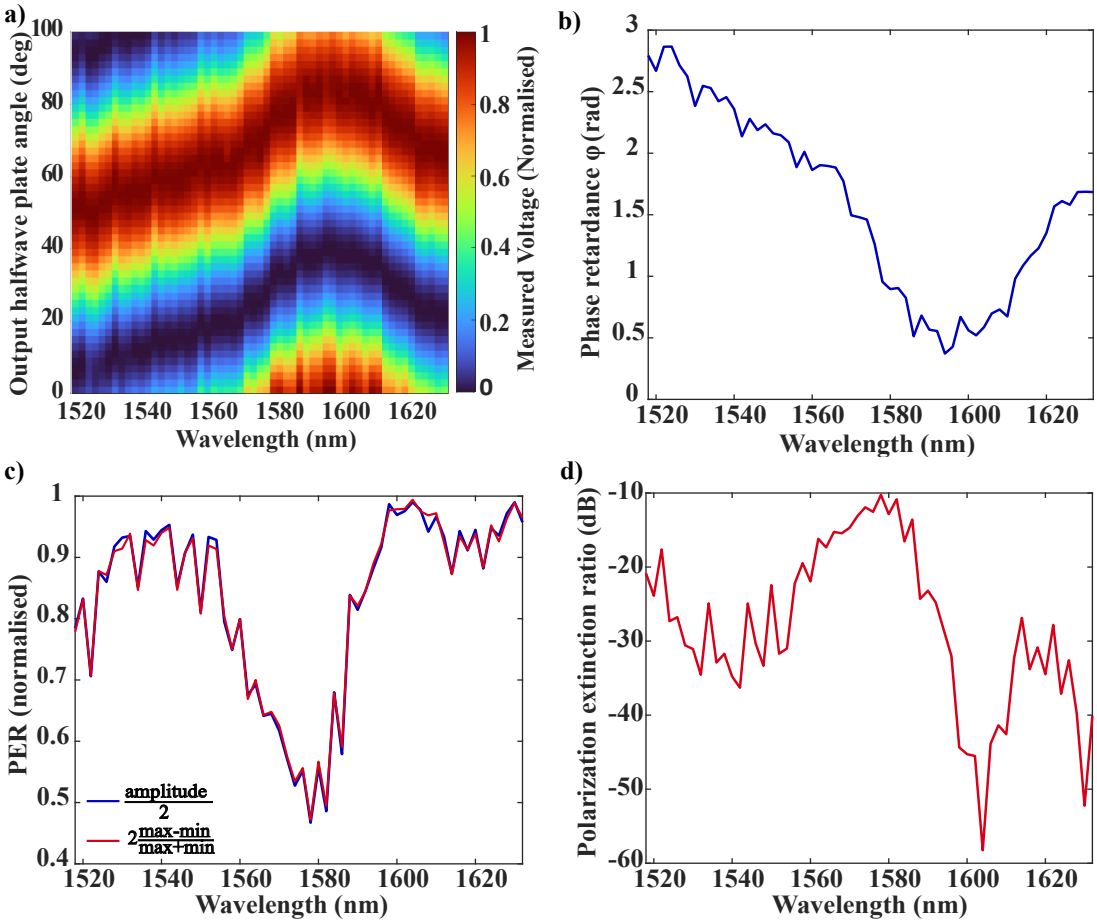

Figure 5.4: **Wavelength-dependent phase retardance of linearly polarised light at the C-band.** a) Shows the self-normalised signal amplitude obtained from the lock-in amplified photodiode for the various half-wave plate angles at the output of the NANF. b) Phase retardation and c) Normalised PER and d) PER in dB.

Before delving into the effects of dispersion, we wanted to study wavelength-dependent phase retardance, an effect previously investigated by [147]. To this end, for each wavelength of the InGaAsP laser, the output half-wave plate was rotated through a range of angles, while the input polarisation was kept constant (i.e., linearly polarised). Then, similar to the PER measurements before, the output voltage measured from the InGaAs detector was plotted as a function of the output waveplate, resulting in $\cos^2(\theta)$ relationship for each wavelength setting of the laser. It was then observed that, for each wavelength, the $\cos^2(\theta)$ curve starts at a different point on the x-axis, indicating that a wavelength-dependent phase retardance effect may be affecting the PER. An example of these curves is shown in Appendix B. From these, the phase-retardance ϕ was plotted in Figure 5.4 b) and, similar to previous measurements, the PER was obtained from fitting the voltage data to a cosine function. The normalised PER is shown in 5.4 c) while 5.4 d) shows the PER in dB. We observe that the optimum value achieved was -58 dB and only occurred when the phase retardation was at a minimum, as seen from Figure 5.4 b). The same effect was observed for different input polarisations.

When a squeezed vacuum is propagated through the NANF, we expected dispersion to be prominent, as the photon pairs are produced by a pulsed laser and are broadband. We wanted to study whether effects like pulse dispersion would be introduced by the NANF as the pulsed photon pairs propagate down the length of the fiber. To achieve this, pulses of varying bandwidths were characterised and compared before and after propagation through the NANF, and photon arrival times were recorded by coupling into the SM2000 fiber to the SNSPDs, connected to time-tagging electronics. The temporal spreading of the pulse was studied for three cases using band-pass filters to select different spectral bandwidths of the PDC field. More specifically, 55-, 35-, and 10-nm (FWHM around 2.09 µm) filters were used, and a transform-limited Gaussian pulse was assumed for each filter. Due to the need to couple into the SM2000 fiber, for detection to happen with the SNSPDs, the recorded data for the pulse arrival would also contain broadening effects introduced by the 15-m-long single-mode SM2000. It was important to account for those. To this end, before any propagation into the NANF, the transformed limited pulse was assumed to be the PDC light coupled into the SM200 fiber. Hence, the experimental data were fitted using the transform-limited pulse convolved with a Gaussian, which would contain all the effects introduced by the single-mode fiber as well as any electronic jitter from the detector. The FWHM of the Gaussian was then varied until the obtained convolution matched the experimental data. The data and the accompanying fit are presented in the first column of Figure 5.5. As shown by the data and the estimated FWHM of the Gaussian, convolved with the transform-limited pulse, no difference was observed among the three pulses with distinct bandwidths.

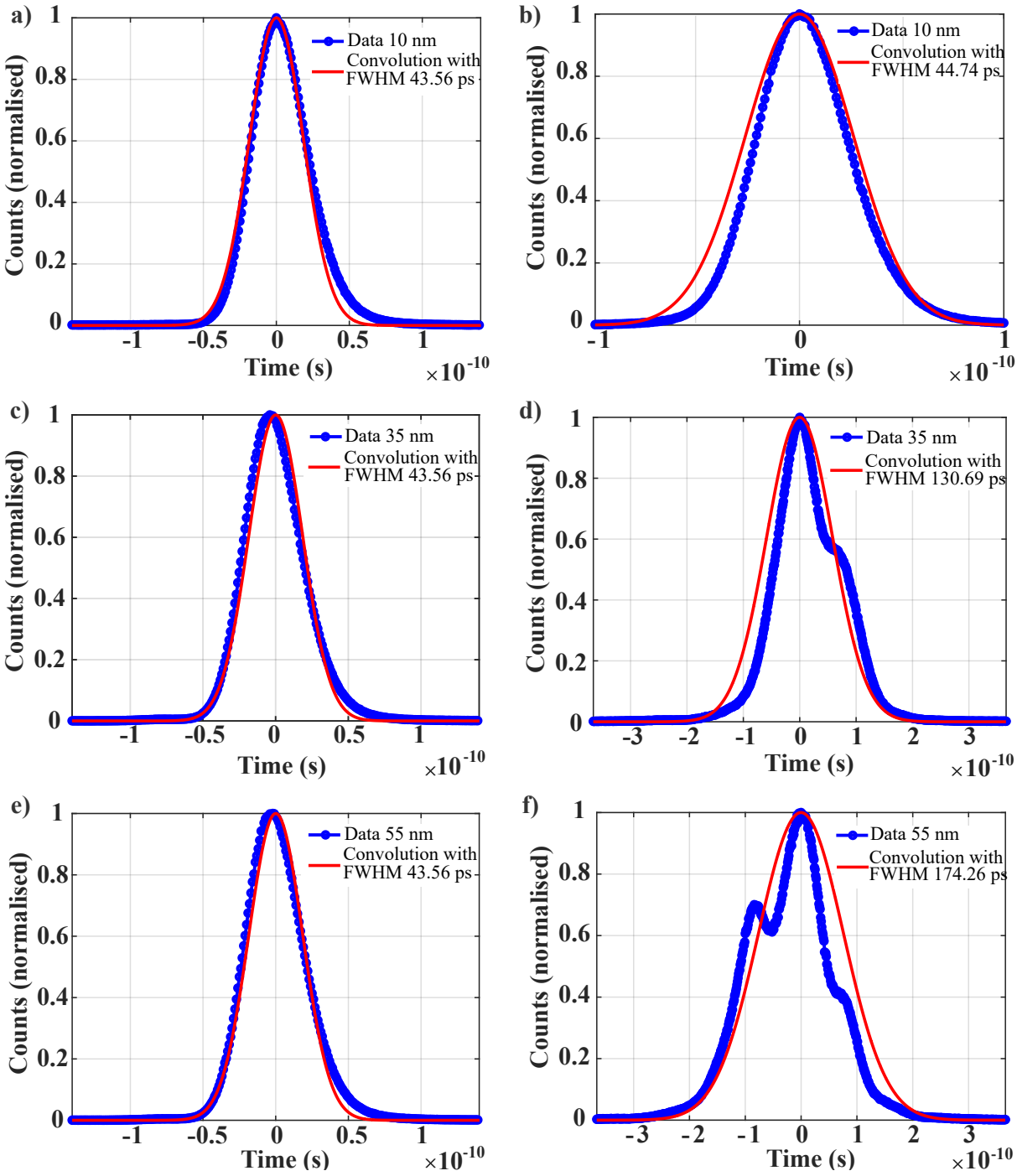

Figure 5.5: **Dispersion Introduced by the NANF on the PDC radiation.** a) Shows the pulse with a bandwidth of 10 nm before propagating into the NANF, and b) the output dispersed pulse after NANF propagation. Subfigures c) and d) illustrate the same for the 35 nm pulse, while e) and d) correspond to the pulse with 55 nm bandwidth.

A similar method to the one mentioned above was followed for the data acquired after the PDC pulses where propagated through the NANF. This time, a new Gaussian was convolved with the resulting Gaussian obtained from the previous convolution. The FWHM of the new Gaussian was varied until it matched the experimental data obtained

with the FWHM shown on the second column of Figure 5.5 for each pulse bandwidth. Our data indicate that the broader pulse (i.e., 55 nm) is most affected by NANF dispersion, consistent with the expected temporal spreading of different colours. For each bandwidth, the GDD was calculated from the temporal durations of the pulses before and after NANF propagation, and the three GDD values were averaged to derive the NANF GDD. The average GDD of the NANF fiber was equal to 3.64 ps^2 but such properties of these fibers depend highly on their geometries [158].

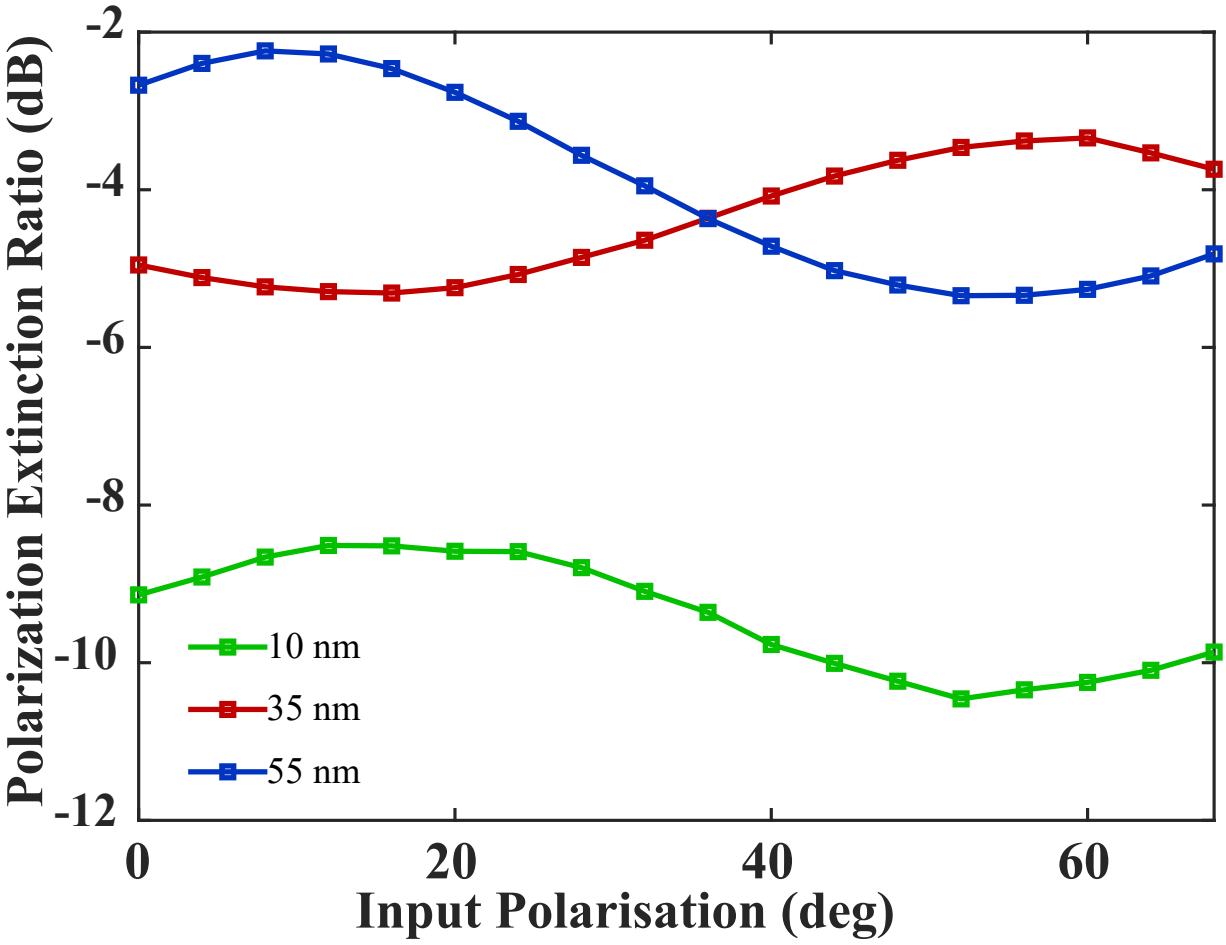

Figure 5.6: **PER of 2µm photon pairs through the NANF.** The plot includes data of the PER of broadband photons generated by SPDC filtered using 10-, 35- and 55-nm spectral filters, respectively.

To examine whether the NANF could serve as a platform for quantum secure communication protocols, such as BB84 and BBM92, we measured the PER as photon pairs propagated through the NANF. The setup used to do so is shown in Figure 5.2, in which the input polarisation optics were configured to admit linearly polarised PDC photons into the NANF. A measurement was performed for each of the three bandwidths of the parametric radiation and the results are shown on Figure 5.6. The highest PER was achieved with a 10 nm band-pass filter, reaching $\sim$ -11 dB.

5.4 Potential for performing polarisation-based quantum communication at 2 µm

We sought to determine whether, with the achieved PER of the photon pairs centred around 2 µm, the NANF could be used to perform quantum communication. In the context of Quantum key distribution (QKD), a useful metric for assessing the protocol's security, efficiency, and reliability is the Quantum bit error rate (QBER) [159, 160]. In digital communication, bit error rate gives the number of errors in a data stream per unit time. Errors in a communication channel can occur when bits of information are altered by noise or interference. In quantum communications, a QBER test is performed to determine whether an eavesdropper is attempting to decode the secret key shared by the two communicating parties. Of course, imperfections in the channel can cause a high QBER, and PER can adversely affect communication. To test whether our recorded PER would affect our ability to perform secure QKD, the QBER was estimated for two different protocols. More specifically, the Bennett-Brassard 1984 (BB84) and the BBM92 protocols were considered.

In the BB84 protocol, 4 quantum states are sent to the receiver, which can be denoted as $\{|H\rangle, |V\rangle, |\oplus\rangle, |\ominus\rangle\}$ representing horizontally, vertically, diagonally and anti-diagonally polarised photons, respectively [160]. The receiver will then measure the state in either the Z-basis (rectilinear) or the X-basis (diagonal). If the QBER is high, then it is possible that unwanted coupling between orthogonal polarisations occurred. To calculate the QBER equation:

$$\varepsilon = \frac{1}{4}\Big(|\langle \mathrm{H_p}|\mathrm{V_m}\rangle|^2 + |\langle \mathrm{V_p}|\mathrm{H_m}\rangle|^2 + |\langle \oplus_\mathrm{p}|\ominus_\mathrm{m}\rangle|^2 + |\langle \ominus_\mathrm{p}|\oplus_\mathrm{m}\rangle|^2\Big) \tag{5.2}$$

is used where ε = QBER and the subscripts p, m refer to the prepared and measured states, respectively. For polarisation-based BB84 QKD, a QBER of 11% or lower is required to achieve secure communication [161]. Simulations were run by Adetunmise C. Data showed that only when the photon pairs were filtered using the 10 nm band-pass was QKD possible, with the 35- and 55-nm bandwidths resulting in QBER of 33.91% and 36.31%, respectively.

The BBM92 protocol is entanglement-based and relies on coincidence measurements [162]. The two communicating parties receive entangled photons in a Bell state, with both photons having either horizontal ($|HH\rangle$) or vertical polarisation ($|VV\rangle$) or a mix of the two, ($|VH\rangle$ or $|HV\rangle$). The number of times the two communicating parties have used the same basis to measure their states indicates the sifted key rate $Q_{Z/X}$, where Z and X are

the rectilinear and diagonal bases, respectively. In this case, the secure key rate is:

$$R_{Z,X} \geq Q_{Z/X}[1 - H(\varepsilon_Z) - H(\varepsilon_X)] \tag{5.3}$$

where $Q_{Z/X}$ is the QBER in each basis while $H(\varepsilon)$ the binary entropy function. Simulations showed that a total secure rate $R_A = R_X + R_X$ of 0.06 bits can be achieved when the broadband photon pairs are filtered using the 10 nm band-pass filter.

5.5 Conclusion

This chapter has demonstrated the work done on NANF. More specifically, the performance of a 1-km-long NAFN, when broadband pulsed parametric radiation centred around 2 µm was propagated through, was studied, and the feasibility of performing quantum communication applications with it was examined. Before any work with entangled photons ensued, the fiber was tested with CW sources. Initially, the attenuation loss was measured to confirm the values provided by the manufacturer and collaborators. During those stages, a fibre laser with a 1560 nm carrier wavelength was used to facilitate alignment and imaging of the output. After the attenuation loss was measured at 0.52 dB/km, the laser source was switched to a 2 µm one to repeat the measurement. For the 2 µm case, the attenuation was 0.95 dB/km. Both values are close to the manufacturer's values, i.e., 0.62 dB/km and 1.39 dB/km at each wavelength.

To perform any polarisation-based communication, the PER needs to be measured, as it indicates how well polarisation is maintained within a system. Previous research has reported exceptional polarisation purity in NANF designs of single-mode hollow-core fibre, reaching values as low as -70 dB at telecom wavelengths [147]. We wanted to see if we could reach these values, and so we tested the PER using an InGaAsP tunable laser. The PER was measured for wavelength across the C band. We recorded a PER of -70 dB at 1550 nm when the input polarisation was set to 60° relative to the horizontal, a value in close agreement with previously published values. Although the principal axis of the fiber is expected to be shifting with wavelength, averaging over all the PER values recorded for the C-band, a PER of -58 dB was achieved. Following the research by A. Taranta et al. [147], which used a Jones matrix model to describe wavelength-dependent phase retardance, we investigated this effect experimentally. Indeed, we observed a phase retardance across the C-band with various input polarisations.

Switching back to the 2 µm CW source, the PER was measured at -50 dB, close to the optics' measurable limits. Given that the NAFN performed well with the classical

source at 2 µm, we wanted to examine the PER with our broadband source of photon pairs. This time, the effects of dispersion were expected to broaden the photon-pair pulse in time. Hence, a scheme was developed to measure the pulse duration at three different bandwidths before and after propagation into the NANF using SNSPDs connected to time-tagging electronics. We concluded that NANF supports the propagation of broadband radiation but limits its operation due to dispersion. However, we note that the NANF design's geometry can affect its dispersion, and ongoing research is underway to optimise these properties [163, 164]. After measuring the PER for three spectral bandwidths, we found that it significantly affects the QBER and secure key rate for two QKD protocols. Our simulations showed that, for the BB84 protocol, the PER affects the quality of polarisation-based QKD, as only when photon pairs are filtered with a 10-nm band-pass filter can QKD be achieved with a low enough QBER. By considering the BBM92 protocol, we estimate a secure key rate of 0.06 bits. One advantage of the BBM92 protocol is that it relies on coincidence measurements, allowing synchronisation in a CW mode. This allows us to reach a much higher secure key rate when photon pairs from a CW source are propagated through the NAFN, as our characterisation has shown that better PER can be achieved with CW sources. Investigating this possibility, our simulations have shown an estimate of 0.68 bits/pair secure key rate.

Our research has shown that NANFs can be a promising platform for polarisation-based QKD at the 2µm region and the results presented here have been published in Optics Express [165].

CHAPTER 6

Conclusion and future work

In this work, we investigate SFG driven by an entangled beam. This study advances the understanding of the effect by employing parametric down-conversion not only in the low-gain (spontaneous) regime but also in the high-gain regime to drive the SFG process. In the spontaneous regime of PDC, the crystal interaction responsible for SFG involves only individual photons. As a result, the efficiency of the process scales linearly with the incoming photon flux. Previous studies have generally assumed that, beyond the spontaneous regime, the eSFG would scale like the classical version of the effect, with a quadratic dependence on the entangled photon flux, and that any quantum enhancement would therefore cease. We found out that this is not the case and showed that by driving the effect at higher photon fluxes, the SFG remains more efficient when compared to SFG produced by a state with high losses. We developed a mathematical model to describe the role of losses in the efficiency of the SFG process, which agrees with experimental results. From Figure 3.14, we observe that a classically generated SFG will produce more photons than SFG produced by an entangled beam with losses present. Still, it will only asymptotically approach the efficiency of SFG created by an entangled beam with zero losses present, showing the importance of minimising and characterising the losses in the field.

I want to emphasise the importance of achieving good imaging of the near field of the down-converted radiation on the plane where SFG is expected to be generated. Imaging of the PDC birth zone enables us to bring the entangled state together, both spatially and temporally, so that it can interact coherently in the nonlinear medium. For the same reason, we have avoided adding any dispersion to the PDC beam by opting to use reflective optics throughout our experimental setup, apart from the filters added to control the PDC spectrum bandwidth. Only by thoroughly optimising the PDC source were we able to achieve the efficiencies reported in Chapter 3, a study that is missing from much of the literature on the effect.

From the theoretical work of Gatti et al. [37], which matches our experimental results, it was expected that the SV's physical parameters are affected by the process gain. We took this into account before performing a comparison of the quantum effect with its classical version, by matching the peak intensities of the classical field to those of PDC. In chapter 3, we showed that classical SFG will start producing more photons than the entangled SFG at around ∼10 photons per mode, an order of magnitude higher than what was thought possible. As the theoretical model describes, the quantum enhancement that occurs depends on the experimental parameters and can be further increased. We tested this experimentally by changing the SFG crystal to a shorter one. While the efficiency of the total SFG decreases, in absolute terms, the comparison with a classical SFG was in favour of the entangled SFG. This is because the phase-matching constraints are less stringent for a shorter crystal, allowing more components of the entangled field to up-convert coherently.

We created a PDC source bright enough to generate an efficient SFG, and we take advantage of this by studying the implications of the effect on imaging. In Chapter 4, we explored how both the coherent and incoherent contribution affects the imaging resolution when illuminating a razor blade. To this end, we use two masks in the far field of the PDC, which, while they would allow the state to retain the same transmission, let different photons of the PDC through to interact in the SFG crystal. MTF measurements have been performed for both cases, and the results showed that the incoherent component can resolve at a higher spatial frequency. These results have the potential to influence the choice of regime in which the signal from entangled two-photon interactions could be studied and imaged, by preferring to excite these processes with PDC at a regime where an incoherent contribution is also expected to be observed.

6.1 Future work

To confirm the significance of the imaging results reported here, further investigation is warranted. More specifically, the results obtained should be compared with MTF measurements performed at the low-gain of the PDC, where only a coherent component is expected. Such a measurement, though, is not straightforward since to detect the eSFG photons produced in that regime, a more sensitive detector than the EMCCD is needed. The PMT could be implemented again, but the setup should be modified to accommodate the fact that the PMT has only one pixel (the active detector area). Such a measurement can be performed by moving both the crystal and the knife edge and acquiring the eSFG response on the PMT. Then the data should be "stitched" together to form an image to measure the MTF.

Furthermore, it is of interest to implement an intermediate imaging plane so that the imaging plane of the PDC near-field will be decoupled from the imaging plane of the razor blade. This way, the knife-edge could be placed in the intermediate imaging plane and then imaged to the plane where the SFG crystal would be placed. It would enable more accurate placement of the knife edge by helping us align it within the PDC's focus point. Additionally, the background acquisition could greatly improve from this, since, for the measurements presented in this thesis, whenever the crystal was rotated to prevent phase-matching, the knife-edge would remain in place, thereby affecting our background acquisition and subtraction from the signal images.

Our technique of adding symmetric and asymmetric losses is unique, and to our knowledge, it hasn't been used in literature before. This could be implemented to study the efficiency of entangled two-photon effects. Similar configurations could also be realised. For example, symmetric and asymmetric losses can be added to the far-field of the PDC in the form of glass. This should cause the photons that are covered by the glass to arrive at the eSFG crystal with an additional delay, thereby reducing the likelihood of recombination with their entangled pair. This is expected to increase the incoherent component SFG generated, but since the photons will only be delayed and not entirely blocked (like in our case), this won't result in the same effect reported in Chapter 4. Placing filters in the far-field with decreasing transmission as a form of introducing symmetric losses and studying the effects that would have on imaging is also of interest. Lastly, to ensure the robustness of the effect, imaging of the razor blade while it is illuminated by a purely coherent source, such as a laser beam. Similar to the comparison presented in Chapter 3, the classical field should match the physical parameters of the PDC, and the same optics that image the razor field should be used. All these, including the formulation of a theoretical model describing the effect's image modalities, could lead to a strong publication.

Although excitation of a biological sample was unsuccessful, the possibility of exciting a sample with a high TPA coefficient remains of interest. After completing the study on imaging and with the knowledge gained from implementing losses, presented in Chapter 3, a robust setup could be designed to measure the eTPA response from a sample while ensuring that any measured signal is attributed to the interaction of entangled photons and that any other effects are rejected. Building on the insight gained from characterising the system's resolution, we could then image the sample's response when excited by entangled photons, demonstrating compatibility with leading-edge applications.

6.2 Final remarks

In conclusion, this thesis has explored entangled two-photon interaction in a novel PDC gain regime. Throughout this work, we showed that entangled effects can compete with their classical counterparts by achieving a high PDC photon number per mode. This was made possible by understanding the entangled photon source, and we demonstrated the potential to compete with current classical techniques.

Bibliography

[1] P. Luu, S. E. Fraser, and F. Schneider, "More than double the fun with two-photon excitation microscopy," *Communications biology*, vol. 7, no. 1, p. 364, 2024.

[2] J. Donnelly and F. E. Hernandez, "Two-photon absorption spectroscopy on curcumin in solution: a state-of-the-art physical chemistry experiment," *Journal of chemical education*, vol. 94, no. 1, pp. 101–104, 2017.

[3] D. Oron, E. Papagiakoumou, F. Anselmi, and V. Emiliani, "Two-photon optogenetics," *Progress in brain research*, vol. 196, pp. 119–143, 2012.

[4] J. Javanainen and P. L. Gould, "Linear intensity dependence of a two-photon transition rate," *Physical Review A*, vol. 41, no. 9, p. 5088, 1990.

[5] N. P. Georgiades, E. Polzik, K. Edamatsu, H. Kimble, and A. Parkins, "Nonclassical excitation for atoms in a squeezed vacuum," *Physical review letters*, vol. 75, no. 19, p. 3426, 1995.

[6] A. Mikhaylov *et al.*, "A comprehensive experimental system for measuring molecular two-photon absorption using an ultrafast entangled photon pair excitation source," in *Advanced optical techniques for quantum information, sensing, and metrology*, SPIE, vol. 11295, 2020, pp. 48–61.

[7] A. Mikhaylov *et al.*, "Hot-band absorption can mimic entangled two-photon absorption," *The Journal of Physical Chemistry Letters*, vol. 13, no. 6, pp. 1489–1493, 2022.

[8] S. Corona-Aquino *et al.*, "Experimental study of the validity of entangled two-photon absorption measurements in organic compounds," *The Journal of Physical Chemistry A*, vol. 126, no. 14, pp. 2185–2195, 2022.

[9] W. G. Wagner and R. W. Hellwarth, "Quantum noise in a parametric amplifier with lossy modes," *Physical Review*, vol. 133, no. 4A, A915–A920, Feb. 1964, ISSN: 0031-899X. DOI: 10.1103/physrev.133.a915.

[10] R. L. Byer and S. E. Harris, "Power and bandwidth of spontaneous parametric emission," *Physical Review*, vol. 168, no. 3, pp. 1064–1068, Apr. 1968, ISSN: 0031-899X. DOI: 10.1103/physrev.168.1064.

[11] D. C. Burnham and D. L. Weinberg, "Observation of simultaneity in parametric production of optical photon pairs," *Physical Review Letters*, vol. 25, no. 2, pp. 84–87, Jul. 1970, ISSN: 0031-9007. DOI: 10.1103/physrevlett.25.84.

[12] B. Stray *et al.*, "Quantum sensing for gravity cartography," *Nature*, vol. 602, no. 7898, pp. 590–594, 2022.

[13] P. Frey and S. Rachel, "Realization of a discrete time crystal on 57 qubits of a quantum computer," *Science advances*, vol. 8, no. 9, eabm7652, 2022.

[14] H. Yu *et al.*, "Exploiting nonlocal correlations for dispersion-resilient quantum communications," *Physical Review Letters*, vol. 134, no. 22, p. 220 801, 2025.

[15] P. Cutipa and M. V. Chekhova, "Bright squeezed vacuum for two-photon spectroscopy: simultaneously high resolution in time and frequency, space and wavevector," *Optics Letters*, vol. 47, no. 3, pp. 465–468, 2022.

[16] W. P. Schleich, *Quantum optics in phase space*. John Wiley & Sons, 2015.

[17] N. Korolkova, G. Leuchs, R. Loudon, T. C. Ralph, and C. Silberhorn, "Polarization squeezing and continuous-variable polarization entanglement," *Physical Review A*, vol. 65, no. 5, p. 052 306, 2002.

[18] J. Aasi *et al.*, "Enhanced sensitivity of the ligo gravitational wave detector by using squeezed states of light," *Nature Photonics*, vol. 7, no. 8, pp. 613–619, 2013.

[19] D. Adamou *et al.*, "Quantum-enhanced time-domain spectroscopy," *Science Advances*, vol. 11, no. 4, eadt2187, 2025.

[20] R. L. Sutherland, *Handbook of nonlinear optics*. CRC press, 2003.

[21] B. E. A. Saleh and M. C. Teich, *Fundamentals of Photonics*. Wiley, Aug. 1991, ISBN: 9780471213741. DOI: 10.1002/0471213748.

[22] A. Lahiri, "Nonlinear optics," in *Basic Optics*. Elsevier, 2016, pp. 901–968, ISBN: 9780128053577. DOI: 10.1016/b978-0-12-805357-7.00009-5.

[23] R. W. Boyd, *Nonlinear Optics*. Elsevier Science & Technology Books, 2020, p. 634, ISBN: 9780128110034.

[24] A. Christ, A. Fedrizzi, H. Hübel, T. Jennewein, and C. Silberhorn, "Parametric down-conversion," in *Experimental Methods in the Physical Sciences*, vol. 45, Elsevier, 2013, pp. 351–410.

[25] C. Duncan, L. Perret, S. Palomba, M. Lapine, B. T. Kuhlmey, and C. M. de Sterke, "New avenues for phase matching in nonlinear hyperbolic metamaterials," *Scientific Reports*, vol. 5, no. 1, Mar. 2015, ISSN: 2045-2322. DOI: 10.1038/srep08983.

[26] V. Petrov *et al.*, "Barium nonlinear optical crystals for the mid-ir: characterization and some applications," *Journal of the Optical Society of America B*, vol. 38, no. 8, B46, Jul. 2021, ISSN: 1520-8540. DOI: 10.1364/josab.425169.

[27] H. Wang, M. Mutailipu, Z. Yang, S. Pan, and J. Li, "Computer-aided development of new nonlinear optical materials," *Angewandte Chemie*, vol. 137, no. 6, Dec. 2024, ISSN: 1521-3757. DOI: 10.1002/ange.202420526.

[28] C. Couteau, "Spontaneous parametric down-conversion," *Contemporary Physics*, vol. 59, no. 3, pp. 291–304, Jul. 2018, ISSN: 1366-5812. DOI: 10.1080/00107514.2018.1488463.

[29] G. Wysin, "Quantization of the free electromagnetic field: photons and operators," *Department of Physics, Kansas State University*, 2011.

[30] Y. Shih, *Introduction to Quantum Optics, Photon and Biphoton Physics, Photon and Biphoton Physics*. Taylor & Francis Group, 2020, p. 448, ISBN: 9781003130604.

[31] A. Christ, A. Fedrizzi, H. Hübel, T. Jennewein, and C. Silberhorn, "Parametric down-conversion," in *Single-Photon Generation and Detection - Physics and Applications*. Elsevier, 2013, pp. 351–410. DOI: 10.1016/b978-0-12-387695-9.00011-1.

[32] M. Chekhova, G. Leuchs, and M. Żukowski, "Bright squeezed vacuum: entanglement of macroscopic light beams," *Optics Communications*, vol. 337, pp. 27–43, 2015.

[33] K. Y. Spasibko, T. S. Iskhakov, and M. V. Chekhova, "Spectral properties of high-gain parametric down-conversion," *Optics Express*, vol. 20, no. 7, p. 7507, Mar. 2012, ISSN: 1094-4087. DOI: 10.1364/oe.20.007507.

[34] I. V. Dyakonov, P. R. Sharapova, T. S. Iskhakov, and G. Leuchs, "Direct schmidt number measurement of high-gain parametric down conversion," *Laser Physics Letters*, vol. 12, no. 6, p. 065 202, May 2015, ISSN: 1612-202X. DOI: 10.1088/1612-2011/12/6/065202.

[35] P. Sharapova, A. M. Pérez, O. V. Tikhonova, and M. V. Chekhova, "Schmidt modes in the angular spectrum of bright squeezed vacuum," *Physical Review A*, vol. 91, no. 4, p. 043 816, 2015.

[36] D. Klyshko, "Photons and nonlinear optics, gordon and breach, ny," 1988.

[37] A. Gatti, M. Clerici, and L. Caspani, "Enhancing upconversion with space–time entanglement: from twin photons to twin-beams," *Optica Quantum*, vol. 3, no. 3, pp. 269–279, 2025.

[38] E. Brambilla, O. Jedrkiewicz, L. A. Lugiato, and A. Gatti, "Disclosing the spatiotemporal structure of parametric down-conversion entanglement through frequency up-conversion," *Physical Review A—Atomic, Molecular, and Optical Physics*, vol. 85, no. 6, p. 063 834, 2012.

[39] A. Gatti, O. Jedrkiewicz, and E. Brambilla, "Modeling the space-time correlation of pulsed twin beams," *Scientific Reports*, vol. 13, no. 1, p. 16 786, 2023.

[40] T. B. Pittman, Y. H. Shih, D. V. Strekalov, and A. V. Sergienko, "Optical imaging by means of two-photon quantum entanglement," *Physical Review A*, vol. 52, no. 5, R3429–R3432, Nov. 1995, ISSN: 1094-1622. DOI: 10.1103/physreva.52.r3429.

[41] H. Defienne, B. Ndagano, A. Lyons, and D. Faccio, "Polarization entanglement-enabled quantum holography," *Nature Physics*, vol. 17, no. 5, pp. 591–597, Feb. 2021, ISSN: 1745-2481. DOI: 10.1038/s41567-020-01156-1.

[42] G. Scarcelli and S. H. Yun, "Entangled-photon coincidence fluorescence imaging," *Optics Express*, vol. 16, no. 20, p. 16 189, Sep. 2008, ISSN: 1094-4087. DOI: 10.1364/oe.16.016189.

[43] T. S. Iskhakov, K. Y. Spasibko, M. V. Chekhova, and G. Leuchs, "Macroscopic hong–ou–mandel interference," *New Journal of Physics*, vol. 15, no. 9, p. 093 036, 2013.

[44] P.-A. Moreau, E. Toninelli, T. Gregory, and M. J. Padgett, "Imaging with quantum states of light," *Nature Reviews Physics*, vol. 1, no. 6, pp. 367–380, 2019.

[45] J. C. Howell, R. S. Bennink, S. J. Bentley, and R. W. Boyd, "Realization of the Einstein − Podolsky − Rosen paradox using momentum-and position-entangled photons from spontaneous parametric down conversion," *Physical review letters*, vol. 92, no. 21, p. 210 403, 2004.

[46] A. Aspect, P. Grangier, and G. Roger, "Experimental tests of realistic local theories via bell's theorem," *Phys. Rev. Lett.*, vol. 47, pp. 460–463, 7 Sep. 1981. DOI: 10.1103/PhysRevLett.47.460. [Online]. Available: https://link.aps.org/doi/10.1103/PhysRevLett.47.460.

[47] R. S. Bennink, "Optimal collinear gaussian beams for spontaneous parametric down-conversion," *Physical Review A*, vol. 81, no. 5, p. 053 805, May 2010, ISSN: 1094-1622. DOI: 10.1103/physreva.81.053805.

[48] M. Hendrych, X. Shi, A. Valencia, and J. P. Torres, "Broadening the bandwidth of entangled photons: a step towards the generation of extremely short biphotons," *Physical Review A—Atomic, Molecular, and Optical Physics*, vol. 79, no. 2, p. 023 817, 2009.

[49] O. Varnavski, S. K. Giri, T.-M. Chiang, C. J. Zeman IV, G. C. Schatz, and T. Goodson III, "Colors of entangled two-photon absorption," *Proceedings of the National Academy of Sciences*, vol. 120, no. 35, e2307719120, 2023.

[50] A. K. Bain, *Crystal optics: properties and applications*. John Wiley & Sons, 2019.

[51] A. K. Bain, *Crystal Optics: Properties and Applications*. 2019.

[52] D. N. Nikogosyan, *Nonlinear optical crystals: a complete survey*. Springer, 2005.

[53] V. G. Dmitriev, G. G. Gurzadyan, and D. N. Nikogosyan, *Handbook of nonlinear optical crystals*. Springer, 2013, vol. 64.

[54] A. V. Smith, *Crystal nonlinear optics: with SNLO examples*. AS-Photonics Albuquerque, NM, USA, 2018.

[55] A. Gatti, E. Brambilla, and O. Jedrkiewicz, "Unified space–time description of pulsed twin beams," *Philosophical Transactions A*, vol. 382, no. 2287, p. 20 230 334, 2024.

[56] J. Gea-Banacloche, "Two-photon absorption of nonclassical light," *Physical review letters*, vol. 62, no. 14, p. 1603, 1989.

[57] S. Reynaud, C. Fabre, and E. Giacobino, "Quantum fluctuations in a two-mode parametric oscillator," *Journal of the Optical Society of America B*, vol. 4, no. 10, pp. 1520–1524, 1987.

[58] B. Mollow, "Two-photon absorption and field correlation functions," *Physical Review*, vol. 175, no. 5, p. 1555, 1968.

[59] H.-B. Fei, B. M. Jost, S. Popescu, B. E. Saleh, and M. C. Teich, "Entanglement-induced two-photon transparency," *Physical review letters*, vol. 78, no. 9, p. 1679, 1997.

[60] M. C. Teich and B. E. Saleh, "Entangled-photon microscopy," *Cesk. Cas. Fyz*, vol. 47, no. 3, 1997.

[61] B. Dayan, A. Pe'Er, A. A. Friesem, and Y. Silberberg, "Two photon absorption and coherent control with broadband down-converted light," *Physical review letters*, vol. 93, no. 2, p. 023 005, 2004.

[62] A. Pe'Er, B. Dayan, A. A. Friesem, and Y. Silberberg, "Temporal shaping of entangled photons," *Physical review letters*, vol. 94, no. 7, p. 073 601, 2005.

[63] B. Dayan, A. Pe'er, A. A. Friesem, and Y. Silberberg, "Nonlinear interactions with an ultrahigh flux of broadband entangled photons," *Physical review letters*, vol. 94, no. 4, p. 043 602, 2005.

[64] B. Dayan, "Theory of two-photon interactions with broadband down-converted light and entangled photons," *Physical Review A—Atomic, Molecular, and Optical Physics*, vol. 76, no. 4, p. 043 813, 2007.

[65] D.-I. Lee and T. Goodson, "Entangled photon absorption in an organic porphyrin dendrimer," *The Journal of Physical Chemistry B*, vol. 110, no. 51, pp. 25 582–25 585, 2006.

[66] A. R. Guzman, M. R. Harpham, Ö. Süzer, M. M. Haley, and T. G. Goodson III, "Spatial control of entangled two-photon absorption with organic chromophores," *Journal of the American Chemical Society*, vol. 132, no. 23, pp. 7840–7841, 2010.

[67] J. P. Villabona-Monsalve, O. Calderón-Losada, M. Nuñez Portela, and A. Valencia, "Entangled two photon absorption cross section on the 808 nm region for the common dyes zinc tetraphenylporphyrin and rhodamine b," *The Journal of Physical Chemistry A*, vol. 121, no. 41, pp. 7869–7875, 2017.

[68] D. Tabakaev *et al.*, "Energy-time-entangled two-photon molecular absorption," *Physical Review A*, vol. 103, no. 3, p. 033 701, 2021.

[69] L. Upton, M. Harpham, O. Suzer, M. Richter, S. Mukamel, and T. Goodson III, "Optically excited entangled states in organic molecules illuminate the dark," *The Journal of Physical Chemistry Letters*, vol. 4, no. 12, pp. 2046–2052, 2013.

[70] K. M. Parzuchowski *et al.*, "Setting bounds on entangled two-photon absorption cross sections in common fluorophores," *Physical Review Applied*, vol. 15, no. 4, p. 044 012, 2021.

[71] M. G. Raymer, T. Landes, and A. H. Marcus, "Entangled two-photon absorption by atoms and molecules: a quantum optics tutorial," *The Journal of Chemical Physics*, vol. 155, no. 8, 2021.

[72] T. Landes, M. G. Raymer, M. Allgaier, S. Merkouche, B. J. Smith, and A. H. Marcus, "Quantifying the enhancement of two-photon absorption due to spectral-temporal entanglement," *Optics Express*, vol. 29, no. 13, pp. 20 022–20 033, 2021.

[73] T. Landes, M. Allgaier, S. Merkouche, B. J. Smith, A. H. Marcus, and M. G. Raymer, "Experimental feasibility of molecular two-photon absorption with isolated time-frequency-entangled photon pairs," *Physical Review Research*, vol. 3, no. 3, p. 033 154, 2021.

[74] M. G. Raymer, T. Landes, M. Allgaier, S. Merkouche, B. J. Smith, and A. H. Marcus, "How large is the quantum enhancement of two-photon absorption by time-frequency entanglement of photon pairs?" *Optica*, vol. 8, no. 5, pp. 757–758, 2021.

[75] T. Landes, B. J. Smith, and M. G. Raymer, "Limitations in fluorescence-detected entangled two-photon-absorption experiments: exploring the low-to high-gain squeezing regimes," *Physical Review A*, vol. 110, no. 3, p. 033 708, 2024.

[76] K. Y. Spasibko, D. A. Kopylov, V. L. Krutyanskiy, T. V. Murzina, G. Leuchs, and M. V. Chekhova, "Multiphoton effects enhanced due to ultrafast photon-number fluctuations," *Physical Review Letters*, vol. 119, no. 22, p. 223 603, 2017.

[77] D. A. Kopylov, K. Y. Spasibko, T. V. Murzina, and M. V. Chekhova, "Study of broadband multimode light via non-phase-matched sum frequency generation," *New Journal of Physics*, vol. 21, no. 3, p. 033 024, 2019.

[78] O. Jedrkiewicz, J.-L. Blanchet, E. Brambilla, P. Di Trapani, and A. Gatti, "Detection of the ultranarrow temporal correlation of twin beams via sum-frequency generation," *Physical Review Letters*, vol. 108, no. 25, p. 253 904, 2012.

[79] R. Hanbury Brown and R. Twiss, "Correlation between photons in two coherent beams of light," *SPIE MILESTONE SERIES MS*, vol. 139, pp. 93–95, 1997.

[80] A. Jechow, M. Seefeldt, H. Kurzke, A. Heuer, and R. Menzel, "Enhanced two-photon excited fluorescence from imaging agents using true thermal light," *Nature Photonics*, vol. 7, no. 12, pp. 973–976, 2013.

[81] A. Gatti, E. Brambilla, M. Bache, and L. A. Lugiato, "Ghost imaging with thermal light: comparing entanglement and classical correlation," *Physical review letters*, vol. 93, no. 9, p. 093 602, 2004.

[82] D. Zhang, Y.-H. Zhai, L.-A. Wu, and X.-H. Chen, "Correlated two-photon imaging with true thermal light," *Optics letters*, vol. 30, no. 18, pp. 2354–2356, 2005.

[83] B. E. Saleh, B. M. Jost, H.-B. Fei, and M. C. Teich, "Entangled-photon virtual-state spectroscopy," *Physical review letters*, vol. 80, no. 16, p. 3483, 1998.

[84] E. Brambilla, A. Gatti, M. Bache, and L. A. Lugiato, "Simultaneous near-field and far-field spatial quantum correlations in the high-gain regime of parametric down-conversion," *Physical Review A*, vol. 69, no. 2, p. 023 802, 2004.

[85] P. Günter, *Nonlinear optical effects and materials*. Springer, 2012, vol. 72.

[86] R. M. Malone *et al.*, "Design of a thermal imaging diagnostic using 90-degree off-axis parabolic mirrors," in *Current Developments in Lens Design and Optical Engineering VII*, P. Z. Mouroulis, W. J. Smith, and R. B. Johnson, Eds., vol. 6288, SPIE, Aug. 2006, 62880Z. DOI: 10.1117/12.681080.

[87] F. X. Kärtner and O. D. Mücke, *Nonlinear Optics*. Centre for Free-Electron Laser Science, DESY Department of Physics, University of Hamburg, 2016.

[88] R. Klein, G. Kugel, A. Maillard, A. Sifi, and K. Polgar, "Absolute non-linear optical coefficients measurements of bbo single crystal and determination of angular acceptance by second harmonic generation," *Optical Materials*, vol. 22, no. 2, pp. 163–169, 2003.

[89] Y.-H. Kim, "Measurement of one-photon and two-photon wave packets in spontaneous parametric downconversion," *Journal of the Optical Society of America B*, vol. 20, no. 9, pp. 1959–1966, 2003.

[90] K. Y. Spasibko, T. S. Iskhakov, and M. V. Chekhova, "Spectral properties of high-gain parametric down-conversion," *Optics express*, vol. 20, no. 7, pp. 7507–7515, 2012.

[91] S.-Y. Baek and Y.-H. Kim, "Spectral properties of entangled photon pairs generated via frequency-degenerate type-i spontaneous parametric down-conversion," *Physical Review A—Atomic, Molecular, and Optical Physics*, vol. 77, no. 4, p. 043 807, 2008.

[92] W. Becker, *The bh TCSPC handbook*. Becker & Hickl GmbH, 2021.

[93] D. Tabakaev *et al.*, "Spatial properties of entangled two-photon absorption," *Physical Review Letters*, vol. 129, no. 18, p. 183 601, 2022.

[94] T. Dickinson *et al.*, "Quantum-enhanced second harmonic generation beyond the photon pairs regime," *Science Advances*, vol. 11, no. 27, eadw4820, 2025.

[95] O. Varnavski and T. Goodson III, "Two-photon fluorescence microscopy at extremely low excitation intensity: the power of quantum correlations," *Journal of the American Chemical Society*, vol. 142, no. 30, pp. 12 966–12 975, 2020.

[96] O. Varnavski, C. Gunthardt, A. Rehman, G. D. Luker, and T. Goodson III, "Quantum light-enhanced two-photon imaging of breast cancer cells," *The Journal of Physical Chemistry Letters*, vol. 13, no. 12, pp. 2772–2781, 2022.

[97] C. A. Casacio *et al.*, "Quantum-enhanced nonlinear microscopy," *Nature*, vol. 594, no. 7862, pp. 201–206, 2021.

[98] B. Ndagano *et al.*, "Quantum microscopy based on hong–ou–mandel interference," *Nature Photonics*, vol. 16, no. 5, pp. 384–389, 2022.

[99] Z. He, Y. Zhang, X. Tong, L. Li, and L. V. Wang, "Quantum microscopy of cells at the heisenberg limit," *Nature Communications*, vol. 14, no. 1, p. 2441, 2023.

[100] A. M. Dąbrowska, S. M. Kolenderska, J. Szlachetka, K. Słowik, and P. Kolenderski, "Quantum-inspired optical coherence tomography using classical light in a single-photon counting regime," *Optics Letters*, vol. 49, no. 2, pp. 363–366, 2024.

[101] K. Hashimoto, D. B. Horoshko, and M. V. Chekhova, "Broadband spectroscopy and interferometry with undetected photons at strong parametric amplification," *Advanced Quantum Technologies*, vol. 8, no. 4, p. 2 300 299, 2025.

[102] Rayleigh, "Xv. on the theory of optical images, with special reference to the microscope," *The London, Edinburgh, and Dublin Philosophical Magazine and Journal of Science*, vol. 42, no. 255, pp. 167–195, 1896.

[103] B. R. Masters and B. R. Masters, "Helmholtz's contributions on the theoretical limits to the resolution of the microscope," *Superresolution Optical Microscopy: The Quest for Enhanced Resolution and Contrast*, pp. 109–139, 2020.

[104] V. Giovannetti, S. Lloyd, L. Maccone, and J. H. Shapiro, "Sub-rayleigh-diffraction-bound quantum imaging," *Physical Review A—Atomic, Molecular, and Optical Physics*, vol. 79, no. 1, p. 013 827, 2009.

[105] E. Toninelli *et al.*, "Resolution-enhanced quantum imaging by centroid estimation of biphotons," *Optica*, vol. 6, no. 3, pp. 347–353, 2019.

[106] e. P. Franken, A. E. Hill, C. Peters, and G. Weinreich, "Generation of optical harmonics," *Physical review letters*, vol. 7, no. 4, p. 118, 1961.

[107] S. Fine and W. Hansen, "Optical second harmonic generation in biological systems," *Applied optics*, vol. 10, no. 10, pp. 2350–2353, 1971.

[108] X. Chen, O. Nadiarynkh, S. Plotnikov, and P. J. Campagnola, "Second harmonic generation microscopy for quantitative analysis of collagen fibrillar structure," *Nature protocols*, vol. 7, no. 4, pp. 654–669, 2012.

[109] A. Aghigh, S. Bancelin, M. Rivard, M. Pinsard, H. Ibrahim, and F. Légaré, "Second harmonic generation microscopy: a powerful tool for bio-imaging," *Biophysical Reviews*, vol. 15, no. 1, pp. 43–70, 2023.

[110] P. J. Campagnola and L. M. Loew, "Second-harmonic imaging microscopy for visualizing biomolecular arrays in cells, tissues and organisms," *Nature biotechnology*, vol. 21, no. 11, pp. 1356–1360, 2003.

[111] P. J. Campagnola, A. C. Millard, M. Terasaki, P. E. Hoppe, C. J. Malone, and W. A. Mohler, "Three-dimensional high-resolution second-harmonic generation imaging of endogenous structural proteins in biological tissues," *Biophysical journal*, vol. 82, no. 1, pp. 493–508, 2002.

[112] R. A. R. Rao, M. R. Mehta, and K. C. Toussaint Jr, "Fourier transform-second-harmonic generation imaging of biological tissues," *Optics express*, vol. 17, no. 17, pp. 14 534–14 542, 2009.

[113] D. Singh, V. Rai, and D. K. Agrawal, "Regulation of collagen i and collagen iii in tissue injury and regeneration," *Cardiology and cardiovascular medicine*, vol. 7, no. 1, p. 5, 2023.

[114] S. S. Mathew-Steiner, S. Roy, and C. K. Sen, "Collagen in wound healing," *Bioengineering*, vol. 8, no. 5, p. 63, 2021.

[115] A. Barh, P. J. Rodrigo, L. Meng, C. Pedersen, and P. Tidemand-Lichtenberg, "Parametric upconversion imaging and its applications," *Advances in Optics and Photonics*, vol. 11, no. 4, pp. 952–1019, 2019.

[116] R. Andrews, "Ir image parametric up-conversion," *IEEE Journal of Quantum Electronics*, vol. 6, no. 1, pp. 68–80, 1970.

[117] J.-E. Oh, Y.-W. Cho, G. Scarcelli, and Y.-H. Kim, "Sub-rayleigh imaging via speckle illumination," *Optics letters*, vol. 38, no. 5, pp. 682–684, 2013.

[118] J. S. Dam, C. Pedersen, and P. Tidemand-Lichtenberg, "High-resolution two-dimensional image upconversion of incoherent light," *Optics letters*, vol. 35, no. 22, pp. 3796–3798, 2010.

[119] J. Weller and R. Andrews, "Resolution measurements in parametric upconversion of images," *Opto-electronics*, vol. 2, pp. 171–176, 1970.

[120] J. S. Dam, C. Pedersen, and P. Tidemand-Lichtenberg, "Theory for upconversion of incoherent images," *Optics Express*, vol. 20, no. 2, pp. 1475–1482, 2012.

[121] M. G. Helander, *Handbook of human-computer interaction*. Elsevier, 2014.

[122] R. B. Wheeler, "Use of system image quality models to improve product design," in *IS AND TS PICS CONFERENCE*, SOCIETY FOR IMAGING SCIENCE & TECHNOLOGY, 2000, pp. 204–208.

[123] M. Osadebey, M. Pedersen, D. Arnold, and K. Wendel-Mitoraj, "Image quality evaluation in clinical research: a case study on brain and cardiac mri images in multi-center clinical trials," *IEEE journal of translational engineering in health and medicine*, vol. 6, pp. 1–15, 2018.

[124] S. Abdulla. "Frcr physics notes, image quality." (2021), [Online]. Available: https://www.radiologycafe.com/frcr-physics-notes/x-ray-imaging/image-quality/.

[125] J. W. Goodman, *Introduction to Fourier optics*. Roberts and Company publishers, 2005.

[126] W. B. Wetherell, "The calculation of image quality," in *Applied optics and optical engineering*, vol. 8, Elsevier, 1980, pp. 171–315.

[127] Z. Microscopy. "A beginner's guide to the point spread function." (2014), [Online]. Available: https://bitesizebio.com/22166/a-beginners-guide-to-the-point-spread-function-2/.

[128] E. L. O'Neill, "The modulation function in optics," Ph.D. dissertation, Boston University, 1954.

[129] E. Samei, M. J. Flynn, and D. A. Reimann, "A method for measuring the presampled mtf of digital radiographic systems using an edge test device," *Medical physics*, vol. 25, no. 1, pp. 102–113, 1998.

[130] A. Bigelmaier, K. Schaefer, and H. Wasmund, "An instrument for measuring transfer functions and line spread functions of camera lenses," *Applied Optics*, vol. 7, no. 2, pp. 277–281, 1968.

[131] Y. Zhang, Z. He, X. Tong, D. C. Garrett, R. Cao, and L. V. Wang, "Quantum imaging of biological organisms through spatial and polarization entanglement," *Science Advances*, vol. 10, no. 10, eadk1495, 2024.

[132] D. P. Haefner, "Best practices for imaging system mtf measurement," *Electronic Imaging*, vol. 31, pp. 1–6, 2019.

[133] F. Viallefont-Robinet *et al.*, "Comparison of mtf measurements using edge method: towards reference data set," *Optics express*, vol. 26, no. 26, pp. 33 625–33 648, 2018.

[134] M. Mansuripur, *Classical optics and its applications*. Cambridge University Press, 2002.

[135] K. Huang, J. Fang, M. Yan, E. Wu, and H. Zeng, "Wide-field mid-infrared single-photon upconversion imaging," *Nature communications*, vol. 13, no. 1, p. 1077, 2022.

[136] S. Junaid *et al.*, "Video-rate, mid-infrared hyperspectral upconversion imaging," *Optica*, vol. 6, no. 6, pp. 702–708, 2019.

[137] G. D. Boreman, *Modulation transfer function in optical and electro-optical systems*. SPIE press Bellingham, Washington, 2001, vol. 4.

[138] G. B. Arfken, H. J. Weber, and F. E. Harris, *Mathematical methods for physicists: a comprehensive guide*. Academic press, 2011.

[139] C. Sujatha, "Fundamentals of signal analysis," in *Vibration, Acoustics and Strain Measurement: Theory and Experiments*, Springer, 2023, pp. 351–464.

[140] P. S. Considine, "Effects of coherence on imaging systems," *Journal of the Optical Society of America*, vol. 56, no. 8, pp. 1001–1009, 1966.

[141] T. Skinner, "Surface texture effects in coherent imaging," *Journal of Optical Society of America*, vol. 53, no. 11, p. 1350, 1963.

[142] D. J. Richardson, "Filling the light pipe," *Science*, vol. 330, no. 6002, pp. 327–328, 2010.

[143] D. E. Couch *et al.*, "Ultrafast 1 mhz vacuum-ultraviolet source via highly cascaded harmonic generation in negative-curvature hollow-core fibers," *Optica*, vol. 7, no. 7, pp. 832–837, 2020.

[144] B. Debord, F. Amrani, L. Vincetti, F. Gérôme, and F. Benabid, "Hollow-core fiber technology: the rising of "gas photonics"," *Fibers*, vol. 7, no. 2, p. 16, 2019.

[145] Y. Hong *et al.*, "Hollow-core nanf for high-speed short-reach transmission in the s+ c+ l-bands," *Journal of Lightwave Technology*, vol. 39, no. 19, pp. 6167–6174, 2021.

[146] F. e. Poletti *et al.*, "Towards high-capacity fibre-optic communications at the speed of light in vacuum," *Nature Photonics*, vol. 7, no. 4, pp. 279–284, 2013.

[147] A. Taranta *et al.*, "Exceptional polarization purity in antiresonant hollow-core optical fibres," *Nature Photonics*, vol. 14, no. 8, pp. 504–510, 2020.

[148] W. Zheng *et al.*, "Wideband low confinement loss anti-resonant hollow core fiber with nested u-shape tube," *Optics Express*, vol. 29, no. 15, pp. 24 182–24 192, 2021.

[149] G. T. Jasion *et al.*, "Hollow core nanf with 0.28 db/km attenuation in the c and l bands," in *Optical Fiber Communication Conference*, Optica Publishing Group, 2020, Th4B–4.

[150] A. Trenti *et al.*, "High fidelity distribution of telecom polarization entangled photons through a 7.7 km antiresonant hollow-core fiber," *IEEE Journal of Selected Topics in Quantum Electronics*, vol. 30, no. 6: Advances and Applications of Hollow-Core Fibers, pp. 1–8, 2024.

[151] X. Zhang *et al.*, "Low loss nested hollow-core anti-resonant fiber at 2 μm spectral range," *Optics Letters*, vol. 47, no. 3, pp. 589–592, 2022.

[152] M. Lamy *et al.*, "Ten gigabit per second optical transmissions at 1.98 μm in centimetre-long sige waveguides," *Electronics Letters*, vol. 53, no. 17, pp. 1213–1214, 2017.

[153] L. M. Rosenfeld *et al.*, "Mid-infrared quantum optics in silicon," *Optics Express*, vol. 28, no. 25, pp. 37 092–37 102, 2020.

[154] W. Shen, G. Zhou, J. Du, L. Zhou, K. Xu, and Z. He, "High-speed silicon microring modulator at the 2 μm waveband with analysis and observation of optical bistability," *Photonics Research*, vol. 10, no. 3, A35–A42, 2022.

[155] S. Prabhakar *et al.*, "Two-photon quantum interference and entanglement at 2.1 μm," *Science advances*, vol. 6, no. 13, eaay5195, 2020.

[156] V. Zuba *et al.*, "Limits of coupling efficiency into hollow-core antiresonant fibres," *Journal of Lightwave Technology*, vol. 41, no. 19, pp. 6374–6382, 2023.

[157] Z. Liu *et al.*, "High-capacity directly modulated optical transmitter for 2-μm spectral region," *Journal of Lightwave Technology*, vol. 33, no. 7, pp. 1373–1379, 2015.

[158] T. Grigorova *et al.*, "Measurement of the dispersion of an antiresonant hollow core fiber," *IEEE Photonics Journal*, vol. 10, no. 4, pp. 1–6, 2018.

[159] A. Gaidash, A. Kozubov, S. Medvedeva, and G. Miroshnichenko, "The influence of signal polarization on quantum bit error rate for subcarrier wave quantum key distribution protocol," *Entropy*, vol. 22, no. 12, p. 1393, 2020.

[160] Á. Schranz and E. Udvary, "Quantum bit error rate analysis of the polarization based bb84 protocol in the presence of channel errors.," in *PHOTOPTICS*, 2019, pp. 181–189.

[161] D. Gottesman, H.-K. Lo, N. Lutkenhaus, and J. Preskill, "Security of quantum key distribution with imperfect devices," in *International Symposium onInformation Theory, 2004. ISIT 2004. Proceedings.*, IEEE, 2004, p. 136.

[162] C. H. Bennett, F. Bessette, G. Brassard, L. Salvail, and J. Smolin, "Experimental quantum cryptography," *Journal of cryptology*, vol. 5, no. 1, pp. 3–28, 1992.

[163] W. Li *et al.*, "Multi-functional metasurface: ultra-wideband/multi-band absorption switching by adjusting guided-mode resonance and local surface plasmon resonance effects," *Communications in Theoretical Physics*, vol. 76, no. 6, p. 065 701, 2024.

[164] M. Liu, X. Leng, W. Ni, and P. P. Shum, "Simultaneous and ultrasensitive measurement of refractive index and temperature based on spr of hollow-core anti-resonant fibers," *Plasmonics*, vol. 19, no. 6, pp. 3091–3100, 2024.

[165] I. Afxenti *et al.*, "Polarization purity and dispersion characteristics of nested antiresonant nodeless hollow-core optical fiber at near-and short-wave-ir wavelengths for quantum communications," *Optics Express*, vol. 32, no. 20, pp. 34 471–34 481, 2024.

[166] Y. W. Zhou *et al.*, "High extinction ratio super pixel for long wavelength infrared polarization imaging detection based on plasmonic microcavity quantum well infrared photodetectors," *Scientific reports*, vol. 8, no. 1, p. 15 070, 2018.

Appendix A

The Two Towers

A simplified schematic of the setup for collimating and focusing the photon pairs using spherical mirrors is shown in the figure below. The arrows indicate the direction of the propagation with the first and last mirros being spherical.

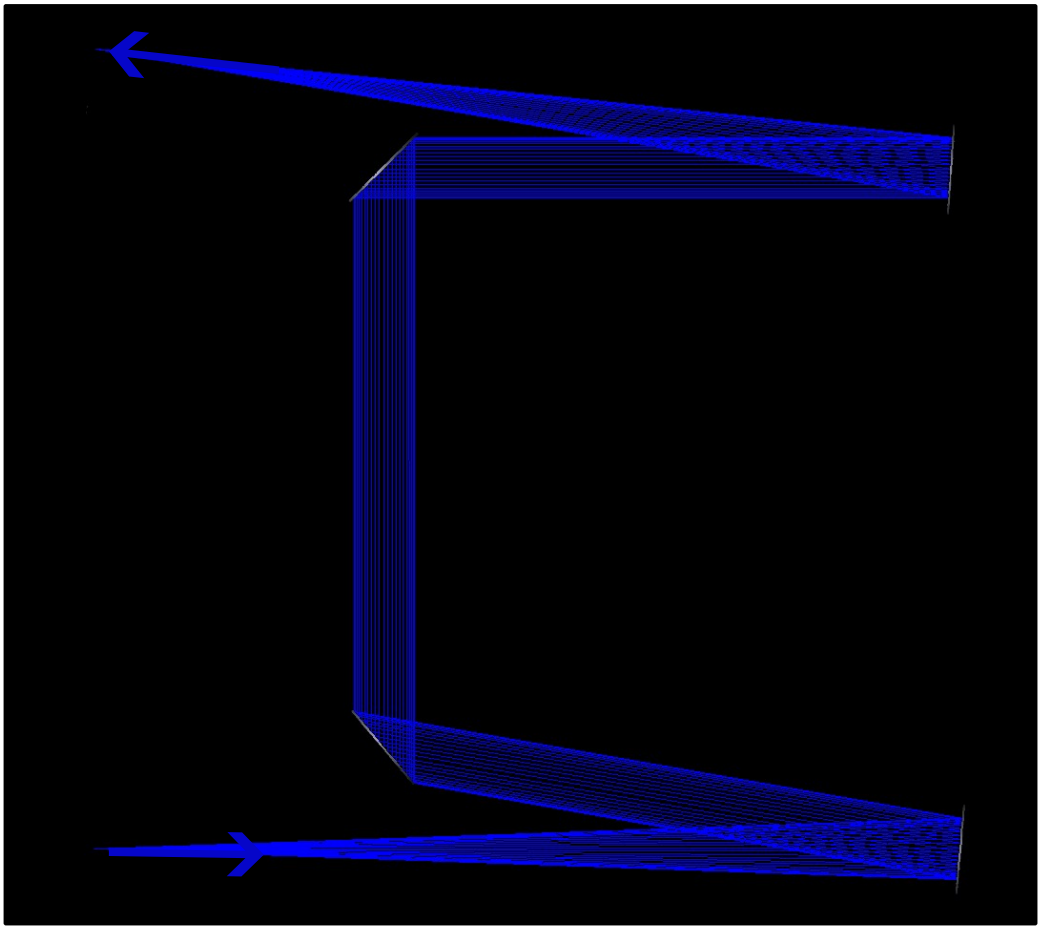

Figure 6.1: **Zemax schematic of spherical mirror setup.**

To ensure the face crystal is positioned on the imaging plane of the 4-f system used to reproduce the near field of the PDC, it was placed on top of a translation stage. An

increase in the efficiency of the SFG is expected when the SFG crystal face aligns on top of the imaging plane, where the photon pairs are spatially coincident. This is not what was observed as the SFG crystal was translated along the imaging plane formed by the spherical mirrors.

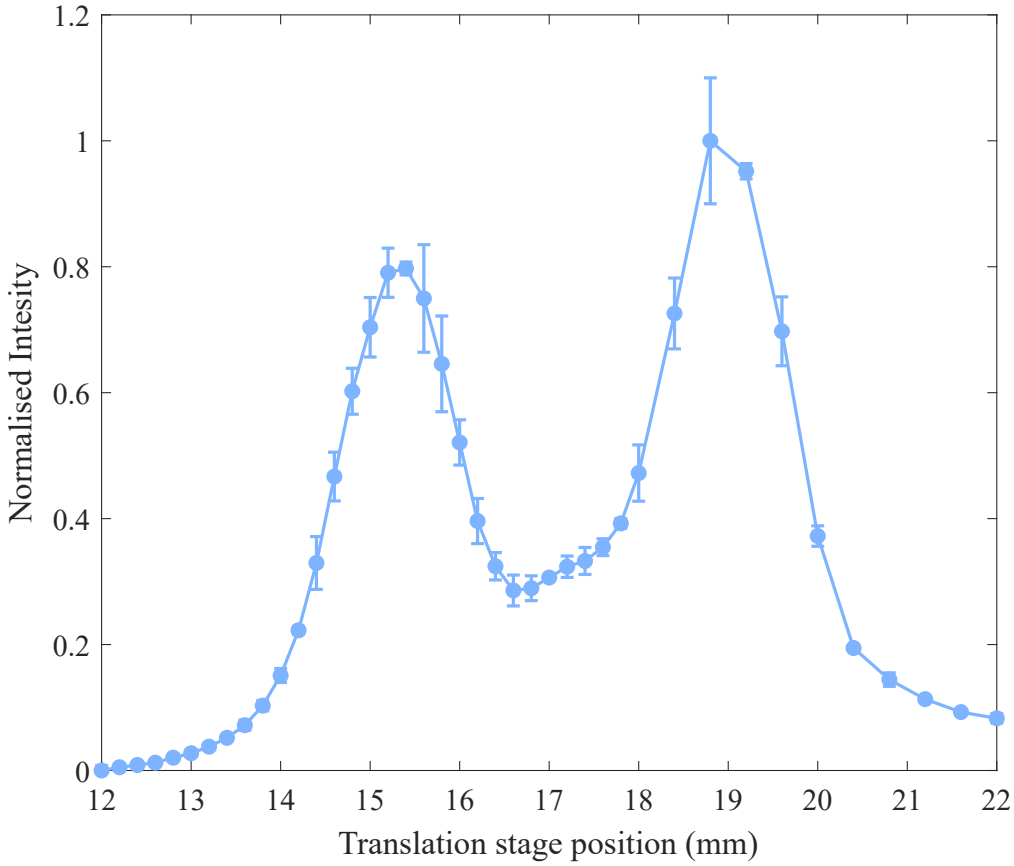

Figure 6.2: **Intensity response of SFG as the crystal was translated through the focus of PDC.**

The results are shown in Figure 6.2, where instead of one distinct peak in intensity as the crystal was translated, two were observed. This double peak in intensity was attributed to aberrations introduced by the spherical mirrors used then to reconstruct the near-field of the PDC state. Concave mirrors must be positioned at an angle nearly parallel to the incoming beam, as they generally have very low tolerance for deviations from this alignment. Due to the need to use dichroics to filter out the pump beam and propagate the entangled state to the SFG crystal, the concave mirrors were placed at a slight angle to reflect the PDC radiation. This was sufficient to induce a possible change in the phase of the entangled pairs, resulting in two peaks in SFG intensity. An interesting observation is that the double peak is 4 mm apart, which is twice the crystal length.

LBO Crystal

As mentioned in the main text, initially, two LBO crystals were used, one to generate the entangled pair and another to generate SFG.

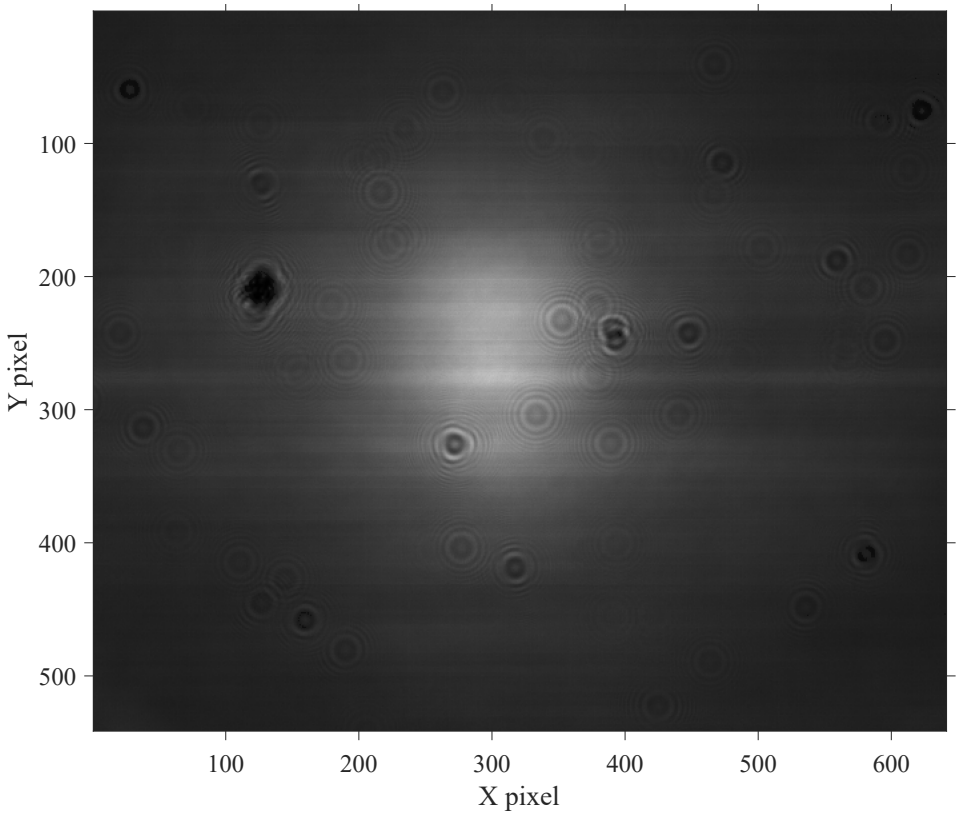

Figure 6.3: **Imaging of near-field PDC produced by the LBO crystal.** The horizontal lines are the anti-reflection coating of the crytal.

Although a non-critically phase-matched crystal would have been optimal for imaging applications, a problem became apparent with the LBOs. More specifically, due to the high intensity of the pump used to generate the entangled pairs, the anti-reflection coating on the crystal suffered damage. This became apparent when the near field of the PDC was imaged after the 4-f system, introducing discrepancies in the phase reconstruction of the photon pairs. Hence, the expected linear eSFG response was not observed.

Example image of the mask

The mask's horizontal edge appears sharper since walk-off only acts in the horizontal direction and any details left or right of the mask appear blurred.

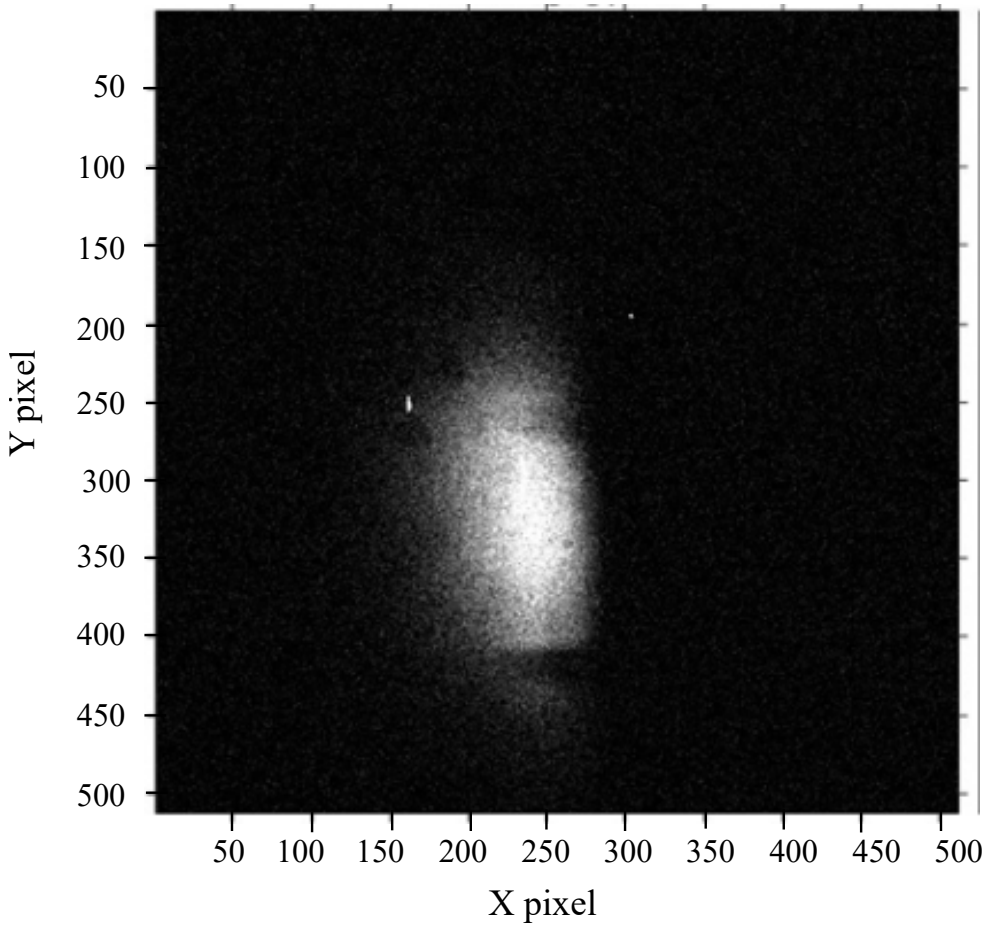

Figure 6.4: **Imaging of mask with vertical and horizontal details.** The mask was placed on the BBO crystal where SFG is generated, and the mask was imaged using the SFG light. It is observed that the horizontal detail is better captured, indicating that walk-off in the horizontal direction affects the vertical portion of the mask.

Appendix B

Quasi-phase matching

Quasi-phase matching occurs when non-homogeneous crystals are used for nonlinear interactions. These crystals are usually structurally modified to achieve spatially modulated nonlinear properties. In cases where we cannot rely on the crystal's birefringence, we exploit the reversal of the d_{eff} coefficient's sign at each structural period of the crystal. This results in the compensation of a nonzero wavevector mismatch, since as the light travels through the length of the nonlinear material, a reversal of the sign of d_{eff} occurs and the amplitude of the field of the resulting radiation continues to grow. A schematic of this is shown in the figure below.

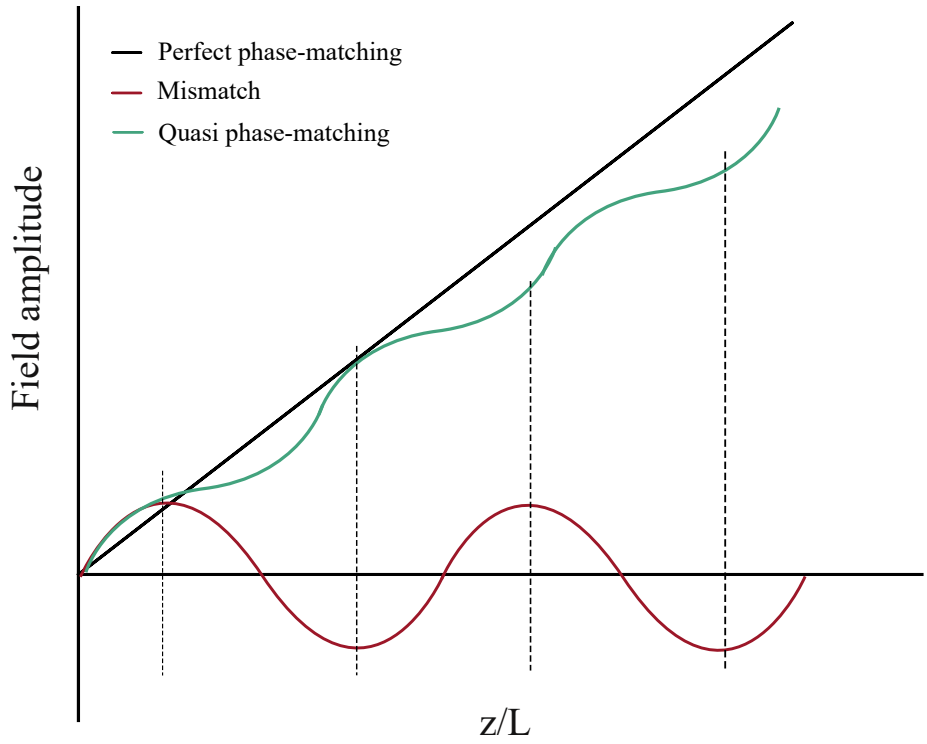

Figure 6.5: **Filed-amplitude for all phase-matching cases.**The green line corresponds to quasi-phase-matching. Here, z is the crystal length and L is the coherent interaction length. Figure modified by [23].

Knife edge

The results of the knife-edge measurement are shown below. In reality, two knife-edge measurements were performed: one at 1-f from the collimating mirror and one farther away, to confirm that the PDC source remained collimated.

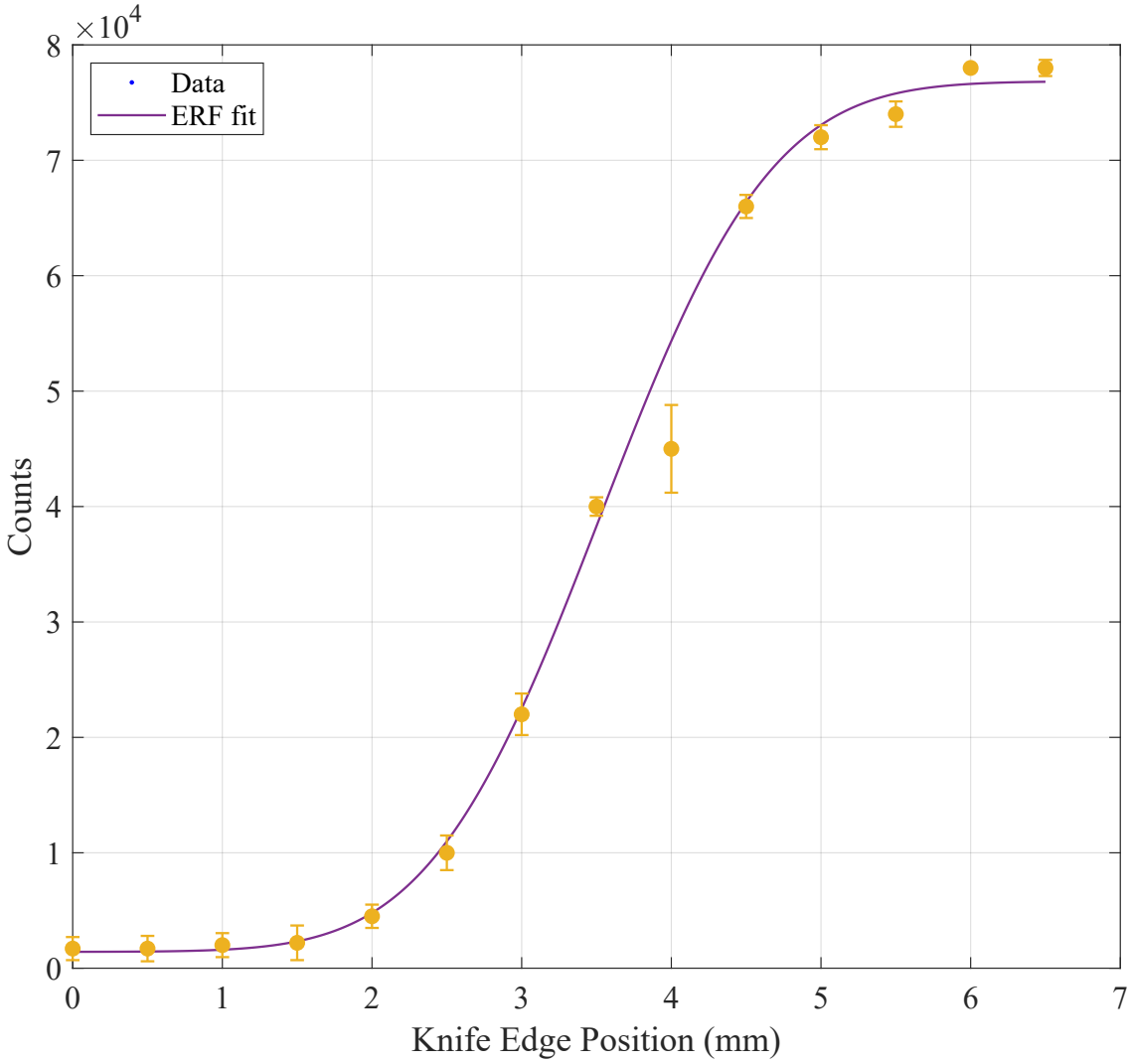

Figure 6.6: **Knife-edge measurement to ascertain the size of the 2μm radiation.** The purple line shows the ERF fit of the experimental data.

The ERF has the form of:

$$P_i = \frac{P}{2}\left(1 + \mathrm{ERF}\left(\frac{h_i - h_0}{w/\sqrt{2}}\right)\right) + d \tag{6.1}$$

where P is the maximum power measured by the detector, h_1 is the position of the blade,

and h_0 is the position where the power reaches half of its maximum. The beam radius is then given by w. From fitting the data to the above equation, the parameter w was found to be 2.9 mm, indicating that the 2 µm beam had a diameter of 6 mm ($1/e^2$).

6.3 Polarisation Extinction

An example of the polarisation extinction is shown in the figure below. As the output half-wave plate rotates, a response curve is recorded. The recorded data are fitted using a $\cos^2(\theta)$ as suggested by literature [166]. From this, the PER is calculated, as explained in the main body of the thesis.

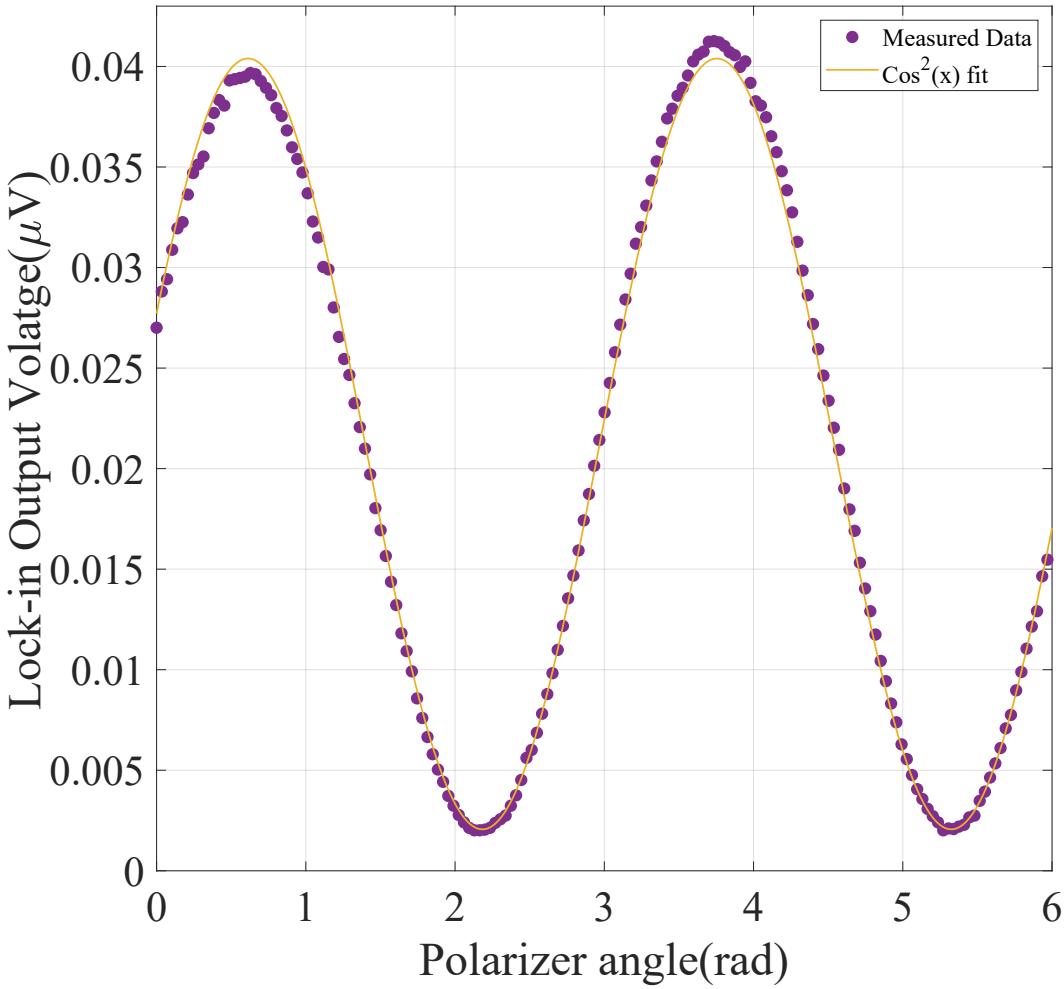

Figure 6.7: **Response curve obtained from rotating the output half-wave plate.** The above data were collected for radiation at 1550 nm with input polarisation of 20°, The purple line corresponds to the $\cos^2(\theta)$ fit of the experimental data.

6.4 Wavelength-dependent phase retardance

Here, polarisation extinction is shown for a set of different wavelengths across the C-band. As shown in the figure, although each beam was set to the same input polarisation, each curve starts at a different point on the x-axis. This indicates that an extra phase term was introduced for different wavelengths.

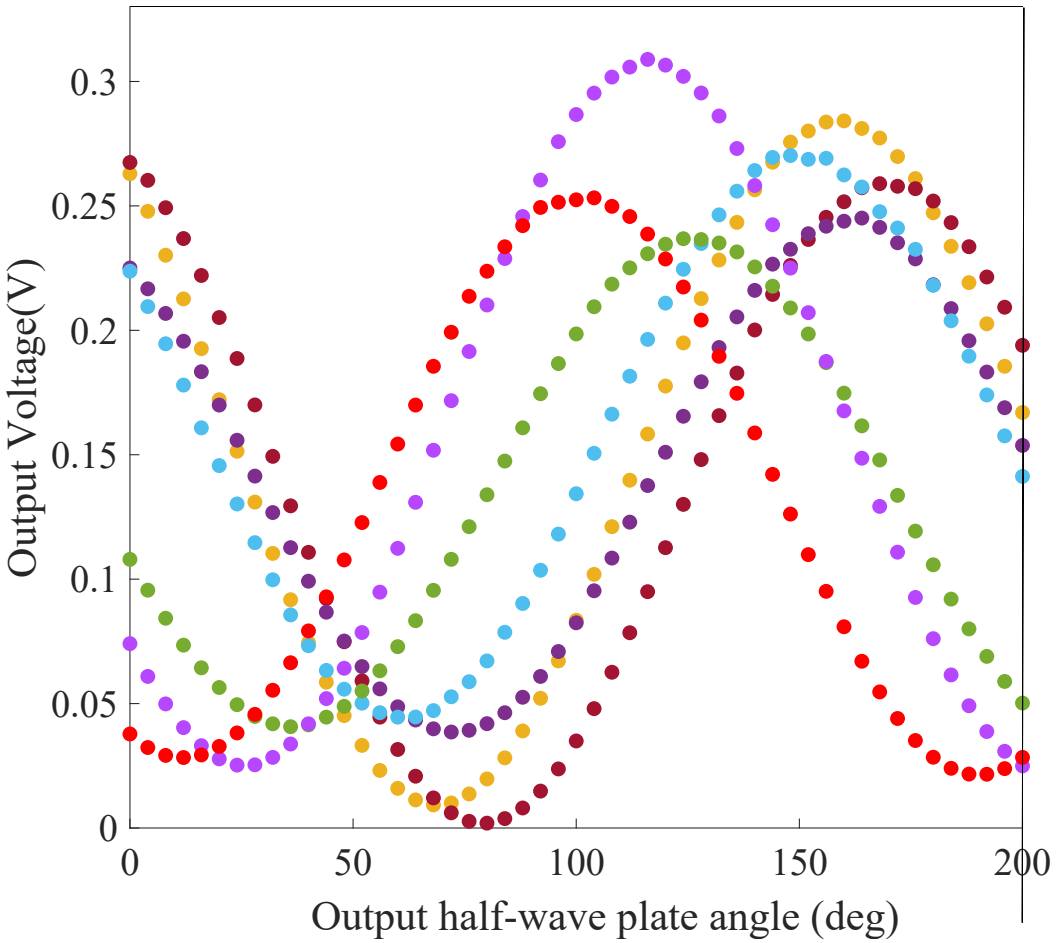

Figure 6.8: **Response curve obtained from wavelengths across the C-band.** The data set above corresponds to the case where the input polarisation was set to horizontal.

For each curve, the best $\cos^2(\theta + \phi)$ fit was determined, and the PER was then calculated. From the fits, the phase term ϕ was obtained and then plotted as shown in Chapter 5.